Ecole doctorale “C2MP” ED 606

Sciences and Technologies

Thèse

pour l’obtention du titre de

Docteur de l’Université de Lorraine

présentée par

Oleg KRUTKIN

Etudes Théoriques et de simulations dédiées à la conception et l’application, pour les tokamaks, de diagnostiques synthétiques de reflectométrie Doppler

Thèse soutenue publiquement le 9 Juin 2020 à Nancy devant le jury composé de:

Prof. Victor BULANIN	Rapporteur	SPbPU
Prof. Pascale HENNEQUIN	Rapporteur	Ecole Polytechnique
Dr. Tim HAPPEL	Examinateur	IPP Garching
Dr. Alexey POPOV	Examinateur	Ioffe Institute
Prof. Etienne GRAVIER	Examinateur	ULorraine
Prof. Stephane HEURAUX	Directeur de thèse	ULorraine
Prof. Evgeniy GUSAKOV	Co-directeur de thèse	Ioffe Institute

Doctoral school “C2MP” ED 606

Sciences and Technologies

Thesis

for obtaining the title of

Docteur de l’Université de Lorraine

presented by

Oleg KRUTKIN

Theoretical analysis and full-wave simulations combined in the development of the synthetic Doppler reflectometry diagnostics for tokamaks

Public defense on 9 June 2020 at Nancy before the jury composed of:

Prof. Victor BULANIN	Referee	SPbPU
Prof. Pascale HENNEQUIN	Referee	Ecole Polytechnique
Dr. Tim HAPPEL	Examinator	IPP Garching
Dr. Alexey POPOV	Examinator	Ioffe Institute
Prof. Etienne GRAVIER	Examinator	ULorraine
Prof. Stephane HEURAUX	Supervisor of thesis	ULorraine
Prof. Evgeniy GUSAKOV	Co-supervisor of thesis	Ioffe Institute

Abstract

Plasma turbulence is nowadays believed to be responsible for the anomalous transport and consequently the degradation of discharge conditions in magnetic confined fusion devices, such as tokamaks. Since a good energy confinement time is crucial for achieving a positive energy yield, understanding and control of turbulent processes is currently one of the major goals of the Magnetic Confinement Fusion research. To study the plasma turbulence, experimental tools that are able to provide information about its characteristics are necessary. Such tools include microwave diagnostics and, in particular, Doppler reflectometry and radial correlation Doppler reflectometry.

While these non-invasive diagnostics benefit from the simplicity of the setup, there are a number of unresolved issues when it comes to the interpretation of the experimental data. Issues such are small-angle scattering and plasma curvature effects limit the range of applicability of the simple interpretation of the measurements, while nonlinear scattering effects make it inapplicable altogether. These problems make it necessary to validate the interpretation of experimental data.

Thus, the primary goal of this thesis was to create a synthetic Doppler reflectometry and radial correlation Doppler reflectometry diagnostic for the interpretation of the FT-2 tokamak experimental results. This goal is achieved by applying full-wave IPF-FD3D code to the results of gyrokinetic plasma modelling with ELMFIRE code to obtain the synthetic signals, which are then benchmarked with experimental measurements. The synthetic diagnostic is also used for a more general study of the possibility of nonlinear effects influencing the experimental measurements.

Finally, the secondary goal of this thesis was to perform an analytical research of plasma curvature effects, nonlinear scattering and a novel technique for turbulence structures' characterization. The first principles analytical study was performed by considering the Helmholtz equation and obtaining an analytical expression for the experimental signals. The results for the latter two topics were numerically validated with the partial use of specially developed linear numerical model and the full-wave IPF-FD3D code.

Résumé

La turbulence du plasma est considérée aujourd'hui comme le mécanisme responsable du transport anormal induisant la dégradation du confinement de l'énergie des plasmas de fusion confinés magnétiquement, tels que les tokamaks. Le temps de confinement de l'énergie est un paramètre crucial pour atteindre un rendement énergétique positif. La maîtrise de ce paramètre passe la compréhension et le contrôle de la turbulence du plasma. Ces thèmes de recherche correspondent actuellement aux principaux objectifs de la recherche sur la fusion par confinement magnétique. Pour réaliser l'étude de la turbulence plasma, des outils expérimentaux capables de fournir ses caractéristiques sont nécessaires. Ces outils comprennent les diagnostics par micro-ondes et, en particulier, la réflectométrie Doppler et la réflectométrie de corrélation radiale Doppler.

Bien que ces diagnostics non invasifs bénéficient d'une configuration simple, il existe un certain nombre de problèmes non résolus associés à l'interprétation des données expérimentales. Des problèmes tels que la diffusion aux petits angles et les effets de courbure du plasma limitent le champ d'application d'une interprétation simple des mesures. La prise en compte des effets de diffusion non linéaire rende l'interprétation standard inapplicable. Ces problèmes nécessitent de valider l'interprétation des données expérimentales.

Ainsi, l'objectif principal de cette thèse était de créer un diagnostic de réflectométrie Doppler synthétique et de réflectométrie de corrélation radiale Doppler pour l'interprétation des résultats expérimentaux du tokamak FT-2. Cet objectif fut atteint en appliquant le code full-wave IPF-FD3D aux résultats d'une modélisation gyrocinétique du plasma turbulent avec le code ELMFIRE pour obtenir les signaux synthétiques. Ces derniers sont ensuite comparés avec des mesures expérimentales. Le diagnostic synthétique est également utilisé pour une étude plus générale de la contribution des effets non linéaires lors des mesures expérimentales.

Un objectif secondaire de cette thèse correspondait à une recherche analytique sur les effets de courbure du plasma et de la diffusion non linéaire puis sur une nouvelle technique pour la caractérisation des structures turbulentes. L'étude analytique basée sur les premiers principes a été réalisée en considérant l'équation de Helmholtz et en obtenant une expression analytique pour les signaux expérimentaux. Les résultats pour ces deux derniers sujets ont été validés numériquement avec l'utilisation partielle d'un modèle numérique linéaire spécialement développé pour ce type d'études et du code IPF-FD3D.

Аннотация

В настоящее время плазменная турбулентность считается причиной возникновения аномального переноса и последующего ухудшения условий разряда в установках магнитного удержания плазмы, таких как токамак. Поскольку высокое время удержания энергии необходимо для достижения положительного энергетического выхода, понимание и контроль турбулентных процессов является одной из основных задач исследования магнитного удержания термоядерной плазмы. Для изучения плазменной турбулентности необходимы экспериментальные методы, позволяющие получить информацию о её характеристиках. Эти методы включают микроволновые диагностики, в частности, допплеровскую рефлектометрию и радиальную корреляционную допплеровскую рефлектометрию.

Преимуществом этих диагностик является простота реализации, однако, существует ряд нерешенных проблем, связанных с интерпретацией экспериментальных данных. Проблемы, такие как малоугловое рассеяние и эффекты кривизны плазмы ограничивают область применимости стандартной интерпретации измерений, а эффекты, связанные с нелинейным рассеянием, делают её полностью некорректной. В связи с этим, интерпретация измерений в эксперименте нуждается в дополнительном подтверждении.

Таким образом, основной целью диссертационной работы было создание синтетических диагностик допплеровской рефлектометрии и радиальной корреляционной допплеровской рефлектометрии для интерпретации экспериментальных результатов токамака ФТ-2. Эта цель достигалась путем применения полноволнового кода IPF-FD3D к результатам гирокинетического моделирования плазмы кодом ELMFIRE с целью получения синтетических сигналов, которые затем соотносились с эксперимательными измерениями. Синтетическая диагностика также была использована для более общего исследования возможности влияния нелинейных эффектов на экспериментальные измерения.

Еще одной целью диссертационной работы был теоретический анализ эффектов кривизны плазмы, нелинейного рассеяния и нового метода определения угла наклона турбулентных структур. Исследование было выполнено путем рассмотрения уравнения Гельмгольца и получения аналитических выражений для диагностических сигналов. Результаты были подтверждены с помощью частичного использования специально разработанной линейной численной модели и полноволнового кода IPF-FD3D.

Résumé étendu

La consommation mondiale d'énergie ne cessant de croître, trouver une nouvelle source d'énergie respectueuse de l'environnement est l'une des tâches essentielles de l'humanité. Pour résoudre ce problème, la fusion thermonucléaire semble être un candidat approprié. Contrairement à la fission, il ne produit que des déchets radioactifs adaptés à un enfouissement superficiel tout en produisant potentiellement la même quantité d'énergie, ce qui le rend plus adapté aux intérêts actuels de la société. De plus, une centrale électrique à fusion potentiellement peut fonctionner de manière régulière et prévisible, contrairement aux sources d'énergie renouvelables telles que l'énergie solaire et éolienne (qui ne produisent pas même assez d'énergie pour répondre aux besoins actuels de l'humanité). La réaction la plus prometteuse et la plus facilement exploitable en raison de sa grande section transversale est la fusion de deux isotopes de l'hydrogène, le deutérium et le tritium, qui produisent 17,6 MeV d'énergie.

Cependant, pour que les réactions de fusion se produisent, les particules doivent d'abord surmonter la barrière de répulsion de Coulomb en se rapprochant suffisamment pour qu'elles puissent passer à travers elle et fusionner. Cela peut être réalisé en chauffant les particules à des températures extrêmes. Ces températures leur permettent de commencer à s'ioniser et le gaz neutre passe à l'état plasma - un gaz de particules chargées. Le pic de la section efficace de la réaction de fusion DT correspond à une température du plasma d'environ 90 keV (ou 1 milliards de degrés Kelvin), qui fait du confinement du plasma de fusion une tâche assez difficile. De plus, un rendement énergétique positif est nécessaire pour utiliser la réaction de fusion comme source d'énergie (bien que le concept de réacteur de fusion-fission qui contourne cette exigence soit également en cours de développement), pour lequel il est nécessaire d'obtenir une pression et une température de plasma suffisamment élevées.

Il existe différentes possibilités pour atteindre ces conditions extrêmes. Dans les étoiles, elle est obtenue par de fortes forces gravitationnelles qui condensent le plasma, mais une telle approche est impossible sur Terre. Une autre approche consiste à se concentrer sur l'obtention d'une densité et d'une température élevées tout en ayant un temps de confinement d'énergie faible. Une telle méthode explosive est appelée confinement inertiel. Enfin, l'une des approches les plus performantes est la fusion par confinement magnétique (MCF). Cette branche de la physique sur la fusion utilise le fait que le plasma est composé de particules chargées et ces dernières sont piégées le long des lignes fermées du champ magnétique, les particules chargées se déplacent alors en spirales autour des lignes de champ magnétique. Étant donné que les particules chargées se déplacent en spirales le long des lignes de champ magnétique, elles doivent en principe être confinées sur une "boucle" associée à une ligne de champ magnétique fermée. C'est pourquoi beaucoup de premiers concepts étaient des machines sous la forme d'un anneau (appelé tore) avec le champ magnétique le long de la direction de la circonférence de «l'anneau» (dénommé composante toroïdale).

L'un des dispositifs basés sur ce principe est le tokamak, où en combinant les champs magnétiques toroïdaux et poloïdaux (ces derniers sont induits par un courant à travers le plasma dans la direction toroïdale), les lignes hélicoïdales de champ magnétique sont ainsi créées. Des lignes de champ magnétique hélicoïdal s'enroulant sur une surface d'un tore à rayon constant à chaque révolution constitue une surface dite magnétique. Le champ magnétique dans une telle configuration est plus fort du côté intérieur du tore et plus faible du côté extérieur. Par conséquent, le côté intérieur proche du solénoïde central est appelé côté haut champ (HFS) et le côté extérieur est appelé côté bas champ (LFS). Une seule particule chargée se déplaçant le long d'une surface magnétique ne doit en principe jamais la quitter. De plus, en raison de la croissance du champ magnétique vers le HFS, les particules ayant une vitesse parallèle (au champ magnétique) suffisamment faible peuvent être piégées dans le miroir magnétique du LFS et être localisées encore plus loin. Cependant, les collisions entre particules provoquant un changement aléatoire de la vitesse et de la direction de leur mouvement provoquent le transport des particules entre les surfaces magnétiques et créent une source de perte d'énergie. Néanmoins, un tel

transport dit collisionnel de particules et d'énergie n'aurait pas empêché les appareils de tokamak modernes de satisfaire au critère du triple produit densité, température temps de confinement de l'énergie plus grand qu'une constante de l'ordre de 10^{21}, appelé critère de Lawson. Malheureusement, le transport des particules observé expérimentalement s'est avéré être beaucoup plus important que prévu en raison du transport turbulent des particules, causé par les micro-instabilités du plasma.

Le plasma de Tokamak en raison de ses conditions extrêmes et forts gradients génère un certain nombre d'instabilités essayant de redistribuer les particules et l'énergie dans une configuration plus homogène. Au cours de la recherche sur le tokamak, il a été découvert que les instabilités des ondes de dérive étaient à l'origine du phénomène de transport anormal (turbulent). Ces instabilités à très petite échelle (de l'ordre du mm) sont entraînées par les gradients de densité et de température et conduisent au développement de la cascade de turbulence non linéaire et finalement à la formation de tourbillons instables. Ces tourbillons, à leur tour, connectent différentes surfaces magnétiques et provoquent un transport anormalement élevé à travers elles. La compréhension des caractéristiques de la turbulence donne un aperçu des causes de celle-ci et une possibilité de la contrôler. En essayant de caractériser la turbulence expérimentalement, les petites fluctuations de la densité et de la température du plasma sont principalement observées (bien que les fluctuations du potentiel électrique et du champ magnétique soient également étudiées). Une grande variété de diagnostics est utilisée pour cette caractérisation, y compris les diagnostics de turbulence micro-ondes.

Bien que les détails varient, le principe principal de tous les diagnostics micro-ondes est de collecter l'onde qui a interagi avec le plasma. Comme les propriétés optiques du plasma sont déterminées par sa densité, une telle onde intègre les informations sur les caractéristiques du plasma et de ses fluctuations. Pour cette raison, le diagnostic par micro-ondes est utilisé à la fois pour les mesures de profil de densité de routine (interférométrie, réflectométrie de balayage) et pour l'étude des fluctuations de densité de plasma (réflectométrie de fluctuation, rétrodiffusion Doppler, réflectométrie de corrélation).

La rétrodiffusion Doppler, communément appelée réflectométrie Doppler (DR), est basée sur le sondage au plasma avec l'incidence oblique du faisceau de sondage par rapport à la surface magnétique et la mesure sur le signal de rétrodiffusion. L'amplitude du signal de diffusion est proportionnelle à l'amplitude de l'harmonique du spectre de nombres d'onde poloïdaux de la turbulence qui a provoqué la diffusion, fournissant des informations sur le spectre de nombres d'onde poloïdaux de la turbulence, tandis que le décalage de fréquence correspond aux vitesses de rotation et de phase de la dite turbulence c'est-à-dire des fluctuations de densité . La réflectométrie Doppler à corrélation radiale (RCDR) est une version de DR, où le sondage est effectué simultanément à plusieurs fréquences proches et la fonction de corrélation croisée (CCF) entre les signaux de diffusion correspondants est calculée. La décroissance de la corrélation avec l'augmentation du décalage de fréquence est interprétée comme la décroissance de la corrélation de turbulence avec la séparation radiale des points de diffusion, et la longueur de corrélation radiale de la turbulence est ainsi déterminée. La dépendance temporelle du CCF donne également des informations sur la vitesse de rotation du plasma ainsi que l'inclinaison possible des structures turbulentes.

Cependant, la simplicité de la configuration du diagnostic est contrebalancée par le fait que l'interprétation des données expérimentales est souvent un problème difficile et parfois non résolu. Ce problème est une conséquence du fait que les processus d'interaction onde-plasma sont assez compliqués dans un milieu inhomogène tels que ceux correspondant au plasma de fusion car ces interactions peuvent être affectées à la fois par des effets de diffusion non linéaire et par une diffusion aux petits angles mal localisée. Cette difficulté d'obtenir des mesures a été observée expérimentalement, numériquement et analytiquement. Ainsi, l'étude des diagnostics DR et RCDR reste un domaine d'étude ouvert et en développement et fait l'objet de cette thèse.

L'objectif principal de cette thèse est de rendre plus claire l'interprétation des mesures expérimentales de DR et RCDR. Pour cela, des études analytiques sont effectuées, en utilisant le modèle analytique s'appuyant sur les premiers principes décrits par l'équation de Helmholtz pour le plasma, le théorème de réciprocité et un tenseur diélectrique à plasma froid. Les objets étudiés comprennent les processus de diffusion non linéaire et l'influence des effets géométriques sur les mesures expérimentales. Ce travail de thèse inclut aussi l'étude linéaire de la nouvelle technique de mesure de l'angle d'inclinaison de turbulence pour RCDR. Les résultats analytiques sont également validés avec les méthodes de modélisation numérique, telles que les calculs pleine onde et la modélisation linéaire.

Cependant, la pièce maîtresse de cette thèse est le développement du diagnostic synthétique FT-2 tokamak RCDR et son application à l'analyse des résultats expérimentaux. Le diagnostic synthétique est créé en couplant les résultats de la modélisation gyrocinétique du plasma tokamak FT-2 avec le code IPF-FD3D pleine onde et le calcul des signaux RCDR synthétiques. Ces signaux sont ensuite comparés aux mesures expérimentales et interprétés en termes de leur relation avec les paramètres de turbulence et l'influence des effets diagnostiques. Une modélisation supplémentaire des ondes complètes est effectuée pour démontrer les effets analytiques attendus, tels que la diffusion non linéaire et la dominance aux petits angles en régime linéaire.

La thèse est composée de onze chapitres. Les cinq premiers chapitres ont un caractère introductif, tandis que les chapitres 6-11 couvrent le travail effectué dans le cadre du projet de thèse.

Le chapitre 1 (Introduction) fournit une brève introduction à la fusion magnétiquement confinée, aux problèmes associés à la turbulence du plasma et au rôle des diagnostics micro-ondes tels que la DR dans leur résolution. Il contient également la motivation derrière le sujet de thèse, ainsi qu'un aperçu du reste du manuscrit.

Le chapitre 2 traite plus en détail des processus turbulents dans le plasma magnétisé, couvre les cascades de turbulence, les propriétés de turbulence spécifiques au tokamak (y compris l'angle d'inclinaison des structures turbulentes par rapport à la surface magnétique, pertinent pour la mesure RCDR) et son effet sur le transport. Ce chapitre donne également un bref aperçu des méthodes expérimentales utilisées pour la recherche sur la turbulence.

Le chapitre 3 fournit le contexte théorique utilisé pour décrire les diagnostics DR et RCDR, une description détaillée des micro-ondes se propageant et se dispersant dans le plasma ainsi que l'approche typique de l'analyse théorique de la DR. Les quantités mesurées dans l'expérience, des exemples de configuration expérimentale et les principaux problèmes compliquant l'interprétation des mesures sont également donnés dans les dernières sections.

Le chapitre 4 décrit les outils numériques possibles disponibles pour l'analyse de la propagation des ondes dans le plasma magnétisé, ainsi que les outils utilisés pour la modélisation du plasma lui-même. En particulier, le principe de la modélisation linéaire utilisée dans la thèse est détaillé et expliqué.

Le chapitre 5 présente les informations sur les spécificités du tokamak FT-2 ainsi que sur la décharge utilisée pour le développement du diagnostic synthétique. Le tokamak FT-2 comporte un limiteur classique avec un rapport d'aspect important. Son rayon principal est de 55 cm, tandis que son rayon mineur est de 8 cm. Il est équipé d'un ensemble de diagnostics micro-ondes, y compris DR et RCDR (qui sont étudiés dans cette thèse), ainsi que de l'interférométrie et de diagnostics de diffusion améliorés.

Le chapitre 6 traite du problème des effets de courbure du plasma jouant un rôle lors de l'interprétation des mesures RCDR. La question est considérée analytiquement dans la géométrie cylindrique dans le cadre d'une approximation linéaire. En considérant la solution WKB d'une équation de

Helmholtz non perturbée et en appliquant le théorème de réciprocité, l'expression analytique du signal de diffusion est obtenue. La relation entre la fonction de corrélation croisée des signaux de diffusion et les paramètres de turbulence est obtenue et s'est révélée qualitativement différente de celle obtenue à partir de la géométrie en tranches. En particulier, la mesure de la séparation spatiale correspondant à différentes fréquences de sondage en géométrie plane est donnée par la séparation des surfaces d'indice nul dites de coupure. Cette nouvelle approche montre qu'en cas de géométrie cylindrique, il n'y a pas d'interprétation physique simple pour la séparation spatiale caractéristique. Les résultats de l'analyse sont appliqués à l'expérience du tokamak FT-2, mais aucune différence substantielle avec l'approche par tranches n'est observée dans le cas présenté.

Le chapitre 7 étudie la capacité du diagnostic RCDR à fournir des informations sur l'angle d'inclinaison des structures turbulentes en utilisant une nouvelle technique. La technique est basée sur la détermination du retard temporel correspondant au maximum du RCDR CCF et relative à l'inclinaison de la structure turbulente en combinaison avec sa rotation. Le problème est étudié analytiquement avec une méthode similaire à celle utilisée au chapitre 6. Dans ce cas, cependant, la solution exacte de l'équation de Helmholtz (donnée par la fonction Airy) est utilisée et le spectre de turbulence est décrit plus en détail. L'étude confirme la capacité de la technique de mesure de l'angle d'inclinaison à fournir des informations pertinentes, mais démontre un certain nombre de facteurs limitant son applicabilité, le principal étant la diffusion aux petits angles dominant le signal de diffusion. Dans l'analyse, une expression pour le CCDR RCDR dans le cas d'une diffusion aux petits angles dominant le signal est également obtenue et s'est avérée incapable de fournir des informations sur la turbulence. Les résultats de l'analyse théorique sont confirmés par une modélisation numérique linéaire. Une technique alternative pour les mesures d'angle d'inclinaison est également décrite et supposée être plus intéressante pour une analyse plus approfondie.

Le chapitre 8 couvre la recherche analytique des effets de diffusion non linéaire dans les mesures par DR. La théorie des perturbations est appliquée à l'équation de Helmholtz pour obtenir les amplitudes des signaux correspondant aux ordres de diffusion linéaires et quadratiques et l'amplitude de turbulence seuil pour le début des effets non linéaires. Les résultats sont obtenus pour une turbulence radialement uniforme, mais sont ensuite généralisés au cas d'une turbulence 2D réaliste. Les résultats obtenus sont comparés aux conclusions précédemment disponibles faites dans le modèle optique physique. La principale différence est une formule de seuil principalement nouvelle, qui serait plus pertinente pour les conditions expérimentales. Cette formule peut être bénéfique par rapport à l'expression, précédemment disponible car elle est moins limitative dans certains cas, décrite dans le chapitre. En dehors de cela, une explication qualitative est également proposée pour le comportement du signal de diffusion avec la croissance de l'amplitude de turbulence. Les résultats analytiques sont ensuite validés par une modélisation numérique incluant les phénomènes de diffusion d'ondes usuellement appelée "full-wave". Bien qu'ils démontrent quelques divergences avec la théorie, un accord est globalement obtenu et l'explication théorique du mécanisme de transition vers un régime non linéaire est confirmée par la simulation. Dans le cadre de ces calculs numériques, il est également démontré que la nouvelle formule peut être différente de celle précédemment disponible de plus d'un ordre de grandeur.

Le chapitre 9 est consacré à l'objectif principal de la thèse - le développement des diagnostics synthétiques DR et RCDR pour le tokamak FT-2. Le diagnostic est développé en utilisant les résultats de la modélisation gyrokinétique tokamak FT-2 comme entrée pour le code pleine onde IPF-FD3D. Les signaux synthétiques résultants sont ensuite analysés et comparés aux mesures expérimentales. L'analyse comparative avec les résultats expérimentaux est présentée et un bon accord est obtenu, bien que certaines divergences soient observées. En particulier, le spectre de fréquence pour le sondage en mode O (ordinaire) et le spectre en nombres d'onde poloïdaux pour le sondage en mode X ne correspondent pas aux résultats de la modélisation. Un certain nombre d'explications possibles à ce problème sont suggérées.

Néanmoins, l'accord avec l'expérience permet de supposer que la modélisation gyrokitétique du plasma de FT-2 fournit un plasma réaliste et l'interprétation des résultats expérimentaux est effectuée.

Le chapitre comprend également une série de calculs avec une amplitude variable de la turbulence obtenue à partir d'une matrice de fluctuations de densité multiplié par un facteur numérique, qui est utilisée pour confirmer le mode de fonctionnement linéaire du diagnostic DR ainsi que le mode de fonctionnement non linéaire du diagnostic RCDR en mode X au FT-2. Cette opération se fait en séparant la densité générée numériquement en profil de fond et en variant rapidement les perturbations, qui sont ensuite mises à l'échelle par un facteur constant. En utilisant cette approche, une étude plus générale des effets non linéaires est réalisée en utilisant les données du cas de modélisation gyrocinétique. Ce cas est prévu et s'est avéré plus approprié pour observer l'effet de diffusion non linéaire sur DR et RCDR. En plus des effets déjà décrits dans la littérature, un nouvel effet de la «linéarisation» de la dépendance du décalage Doppler du signal DR sur le nombre d'onde poloïdal de l'onde de sondage est décrit et le mécanisme sous-jacent est expliqué. Ces calculs démontrent également une sensibilité plus élevée du RCDR aux effets de diffusion non linéaire par rapport à la réflectométrie Doppler.

Enfin, les deux derniers chapitres du manuscrit correspondent aux conclusions et aux perspectives, où les résultats obtenus au sein de la thèse sont résumés et la direction d'une éventuelle recherche future est suggérée. Du point de vue analytique, l'analyse du seuil de non-linéarité pourrait être élargie pour englober également le diagnostic RCDR. Les résultats d'une telle analyse seraient intéressants en rapport avec le fait que le début de non-linéarité s'est produit plus tôt pour RCDR que pour DR.

Du point de vue de la modélisation numérique, le modèle linéaire développé dans le cadre de la thèse pourrait être appliqué à la technique alternative de mesure de l'angle d'inclinaison pour voir laquelle de ces approches est plus faisable.

En ce qui concerne le diagnostic synthétique, une étude supplémentaire suggérée a été réalisée pour explorer si le faisceau non gaussien dans l'expérience est la raison de l'incohérence du spectre de fréquence en mode O. Une autre tâche possible est l'inclusion de la paroi métallique permettant les multiples passages du faisceau de sonde à travers le plasma dans le calcul. Cet effet à passages multiples pourrait être responsable de l'élargissement du spectre poloïdal mesuré en mode X (en faisant passer plus rapidement le cas de sondage équatorial en régime non linéaire) dans l'expérimentation et en tenant compte de cela pourrait résoudre l'écart final entre la modélisation et les résultats expérimentaux.

Enfin, une analyse comparative supplémentaire de la modélisation de la turbulence ELMFIRE par rapport aux mesures expérimentales FT-2 est suggérée, car les mesures du diagnostic amélioré de diffusion UHR micro-ondes sont disponibles. Dans une conception similaire, des diagnostics synthétiques peuvent être développés, bien que les calculs numériques en présence d'un UHR puissent être difficiles.

Table of contents

1. Introduction

With the world's energy consumption steadily growing [1], finding a new, ecologically friendly energy source is one of the crucial tasks for humanity. To solve this problem, thermonuclear fusion seems to be a suitable candidate. Unlike fission, it only produces radioactive waste suitable for shallow burying while potentially producing the same amount of power, which makes it more suitable for the current interests of society. Moreover, a potential fusion power plant can operate steadily and predictably, unlike the renewable powers such as solar and wind energy (which also do no even produce enough energy to fulfill the current needs of humanity). The most promising and easily exploitable reaction due to its large cross-section [2][3], is the fusion of two Hydrogen isotopes, deuterium and tritium:

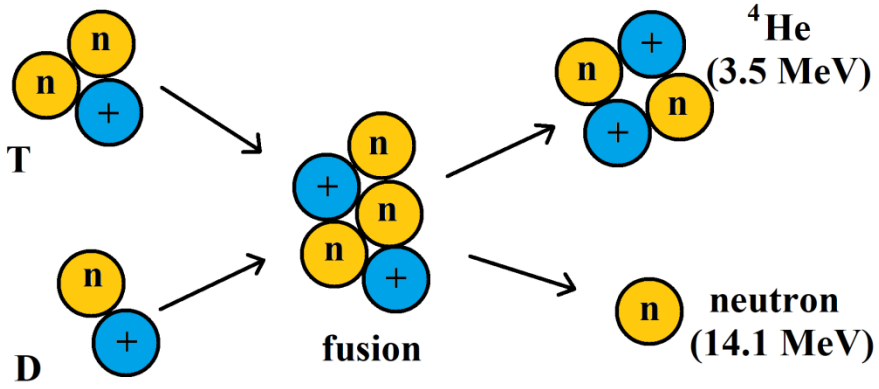

Figure 1.1. An illustration of a fusion reaction.

However, for the fusion reaction to happen, the particles first need to overcome Coulomb repulsion barrier by approaching close enough so that they can tunnel through it and fuse. That can be achieved by heating the particles to extreme temperatures. Such temperatures allow them to start ionizing and for the neutral gas to transform into plasma – a gas of charged particles.

The peak of D-T fusion reaction cross-section corresponds to a plasma temperature of about 70 keV (or 8×10^8 Kelvin) [2][3], which makes the confinement of fusion plasma a rather challenging task. Moreover, a positive energy yield is necessary to utilize the fusion reaction as an energy source (although the fusion-fission reactor concept that circumvents this requirement is also being developed [4]). The estimates for the plasma number density n and energy confinement time τ_E (characteristic time of the plasma energy loss) necessary to produce net energy gain were derived by J. D. Lawson over 60 years ago [4] and are still used in fusion physics in a slightly modified form known as triple product [3]:

$$nT\tau_E > 3\times10^{21}\ \mathrm{keV}\cdot\mathrm{s/m}^3, \tag{1.1}$$

where T is the temperature of the plasma in KeV. There are different possibilities for achieving this condition. In stars it is achieved by strong gravitational forces condensing plasma, but such an approach is impossible on Earth. Another approach is to focus on achieving high density and temperature while having a low energy confinement time. Such an explosive method is called inertial confinement. Finally, one of the most prominent approaches is the magnetic confinement fusion (MCF). This branch of fusion physics utilizes the fact that plasma is composed out of charged particles and is confined within the closed lines of magnetic field, as charged particles move in spirals around magnetic field lines.

1.1. Magnetic confined fusion

To describe the principle of the magnetic confinement it is necessary to describe the charged particle trajectories in magnetic field. Since the charged particles move in spirals along the magnetic field lines, they should in principle be confined within a “circle” created by a closed magnetic field line. That is why a lot of early concepts were machines in the shape of a donut (called torus) with the magnetic field along the “donut” circumference direction (called toroidal). It was found, however, that this toroidal magnetic field is not enough to confine plasma, since the particles in the curved magnetic field lines drift in the direction perpendicular to the field line plane. The solution to that was to introduce a poloidal magnetic field component, with resulting magnetic field having helical field lines winding around the torus of a device and creating surfaces of magnetic field called magnetic surfaces. A poloidal magnetic field can be both a result of the external currents running around plasma and the toroidal current within the plasma.

Focusing on these different possibilities two concepts emerged and are actively developed, the first being stellarator, suggested by L. Spitzer [6] – the device relying on fully external magnetic field, generated by magnetic coils specifically shaped to create closed helical magnetic field lines. The other concept is tokamak, a machine in the shape of torus, where the external toroidal magnetic field is combined with the poloidal field generated by the externally induced plasma current to also obtain helical magnetic field line structure. The name comes from the Russian abbreviation “ТОроидальная КАмера с МАгнитными Катушками” meaning toroidal chamber with magnetic coils, and the first device was developed in Kurchatov institute based on the concept of toroidal confinement device suggested by I. Tamm and A. Sakharov [7] with the addition of plasma current induction to create poloidal magnetic field. A typical scheme of a tokamak is presented in Figure 2. The terms toroidal and poloidal here refer to toroidal coordinate system, which is typically used in tokamak physics and will be used in following chapters along with Cartesian coordinate system.

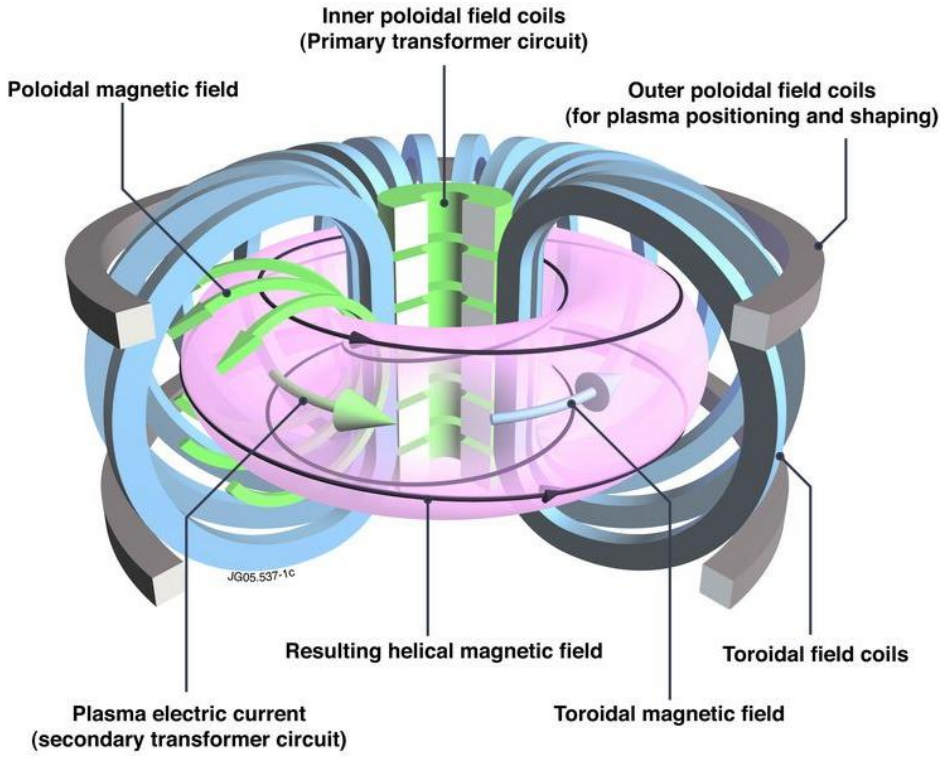

Figure 1.2. The scheme of a typical tokamak device. Sourced from [8].

Helical magnetic field lines winding around the torus with each revolution compose the so-called magnetic surfaces. The magnetic field in such a configuration is stronger on the inner side of the torus and weaker on the outer one. Consequently the inner side close to central solenoid is called the high-field side (HFS) and the outer side is called the low-field side (LFS). A single charged particle moving along a magnetic surface should, in principle never leave it. Moreover, due to magnetic field growing to the HFS, the particles with low enough parallel (to magnetic field) velocity can get trapped in the magnetic mirror on the LFS and be localized even further.

However, collisions between particles causing a random change of the velocity and the direction of their movement cause particle transport between magnetic surfaces and create a source of energy loss. Nevertheless, such collisional particle and energy transport wouldn't have prevented modern tokamak devices from fulfilling triple product condition. Unfortunately experimentally observed transport of particles turned out to be much greater than anticipated due to turbulent transport of particles [9][10][11], caused by plasma micro-instabilities [12].

1.2. Turbulence in magnetized plasma

Tokamak plasma due to its extreme conditions suffers from a number of instabilities trying to redistribute particles and energy into a more homogeneous configuration. In the course of the tokamak research drift-wave instabilities [11][12][13] were discovered to be the main culprit behind the anomalous (turbulent) transport. These extremely small-scale (in the range of mm) instabilities are driven by the gradients of the density and the temperature and lead to the development of the nonlinear turbulence cascade and ultimately to the formation of turbulent eddies. These eddies, in turn, connect different magnetic surfaces and cause an anomalously high transport across them. Understanding characteristics of the turbulence provides insight into the causes of it and a possibility to control it.

The crucial impact of the turbulence on the plasma confinement time makes studying it one of the major tasks of fusion research. When trying to characterize the turbulence experimentally, the small fluctuations of plasma density and temperature are mainly observed (although fluctuations of electric potential and magnetic field are also studied). A large variety of diagnostics is used for the task [14][15] including the microwave turbulence diagnostics [16][17][18].

1.3.Microwave diagnostics

Active microwave methods, such as interferometry, reflectometry, back scattering etc. are actively used both in MCF and general plasma physics (passive methods are also widely employed, but they are not the object of this thesis). In the case of "hot" fusion plasma, their main advantage is the simplicity of implementation.

While details vary, the main principle of all the microwave diagnostics is receiving the wave that has interacted with the plasma. Since optical properties of the plasma are determined by its density, such a wave provides information on plasma characteristic. For this reason, microwave diagnostics are used both for the routine density profile measurements (interferometry, sweeping reflectometry) and for the study of the plasma density fluctuations (fluctuation reflectometry, Doppler back-scattering, correlation reflectometry).

Doppler back-scattering [16][17], commonly referred to as Doppler reflectometry (DR) is based on the plasma probing with the oblique incidence of the probing beam with respect to

magnetic surface and the measurement on the back-scattering signal. Amplitude of the scattering signal is proportional to the amplitude of the turbulence poloidal wavenumber spectrum harmonic which has caused the scattering, providing information about the poloidal wavenumber spectrum of the turbulence, while frequency shift corresponds to the rotational and phase velocities of the said turbulence. Radial correlation Doppler reflectometry (RCDR) [18] is a version of DR, where the probing is performed simultaneously at several close frequencies and the cross-correlation function (CCF) between the corresponding scattering signals is computed. The decay of the correlation with the increase of frequency shift is interpreted as the turbulence correlation decay with the radial separation of the scattering points, and radial correlation length of the turbulence is determined. The temporal dependence of the CCF also gives information about rotation velocity of plasma as well as the possible tilt of the turbulent structures. Similarly, poloidal correlation reflectometry provides the measurement of the poloidal correlation length of the turbulence by computing the CCF of the signal coming to receiver antennas at different poloidal positions. The diagnostic also allows for the measurement of rotation velocity of plasma and even the pitch angle of magnetic field lines.

However, the simplicity of the diagnostic setup is counterbalanced with the fact that interpretation of experimental data is often a challenging and sometimes an unresolved issue. The problem is a consequence of the fact that wave processes are rather complicated in inhomogeneous medium such as plasma and can be affected both by nonlinear scattering effects [19][20] and poorly-localized small-angle scattering [21][22]. Measurements obstruction was observed experimentally, numerically and analytically. Thus, the study of DR and RCDR diagnostics is still an open and developing field of study and is the subject of this thesis.

1.4. Scope of this thesis

The main goal of this thesis is to make interpretation of experimental measurements of DR and RCDR clearer. For that analytical studies are performed, utilizing first principles analytical model based on the Helmholtz equation for plasma, reciprocity theorem and a cold plasma dielectric tensor. The objects studied include nonlinear scattering processes and the influence of geometrical effects on experimental measurements as well as linear study of the novel turbulence tilt angle measurement technique for RCDR. The analytical results are also validated with the numerical modelling methods, such as full-wave computations and linear modelling.

However, the centerpiece of this thesis is the development of the synthetic FT-2 tokamak [23] RCDR diagnostic and its application to the analysis of experimental results. The synthetic diagnostic is created by coupling the results of gyrokinetic modelling of FT-2 tokamak plasma [24] with the full-wave IPF-FD3D code [25] and computing synthetic RCDR signals. These signals are then benchmarked to the experimental measurements and interpreted in terms of their relation to the turbulence parameters and the influence of diagnostic effects. Additional full-wave modelling is performed to demonstrate expected analytical effects, such as nonlinear-scattering and small-angle dominance in linear regime.

Thus, the content of this thesis is divided as follows: chapter 2 and 3 serve as a more detailed introduction into the topics of the plasma turbulence and the microwave diagnostics with the last section of chapter 3 highlighting the issues that required analytical study. Chapter 4 provides a description of FT-2 tokamak device, the diagnostics relevant to this thesis and detailed description of the experimental discharge that was used for the synthetic diagnostic

benchmarking. Chapter 5 describes the numerical approaches available for RCDR studies and justifies the validation approaches used for each task. Consequent sections cover the results obtained within the framework of the thesis: chapter 6 covers analytical research of the plasma curvature effects on RCDR, while in chapter 7, the turbulent structures' tilt angle measurement technique is studied both analytically and numerically. In chapter 8, transition of the DR diagnostics to nonlinear regimen is studied analytically and results are confirmed with full-wave modelling. Finally, chapter 9 covers the results obtained with synthetic DR and RCDR diagnostics. Chapters 10 and 11 contain the conclusions and the future prospects of the thesis respectively.

2. Turbulence and its characterization

In this chapter an overview of turbulence in magnetically confined plasmas is given, as well as basic parameters of the turbulence normally studied experimentally.

The turbulent flow of fluid is characterized by a chaotic change of flow velocity and direction in contrast to laminar flows, corresponding to the liquid flowing in parallel layers. The type of flow is generally characterized in fluid physics by the Reynolds number [26]:

$$R_e = \frac{V_0 \rho L}{\mu}, \tag{2.1}$$

where L is the characteristic size of a system, V_0 is the characteristic velocity of the flow, ρ is the mass density of the fluid (in contrast with the number density n generally used in plasma physics) and μ is the dynamic viscosity coefficient. In the case of the values of $R_e >> 1$ due to inertial forces breaking the turbulent cells down to smaller sizes, a cascade of the turbulent eddies develops, transferring the energy to the structures of smaller scales. Moreover, an inverse turbulent cascade can act as well, causing the deposition of the energy to the higher spatial scales. It was shown by Kolmogorov [26] that in the case of the 3D turbulent flow only direct cascade is present, with resulting energy scaling exponentially with the -5/3 coefficient over the inverse scale of eddies, while the subsequent works [27] have shown that the 2D turbulence is characterized with the existence of the inverse energy cascade scaling as -5/3 and direct cascade scaling as -3 over the inverse turbulent structure scale. Due to the complicated toroidal geometry tokamak plasma has a 2D dimensional character (with the dimension along magnetic field lines being excluded) and it therefore exhibits the inverse turbulent cascade. A rough scheme of theoretical energy distribution for the tokamak plasma is shown on the figure 2.1

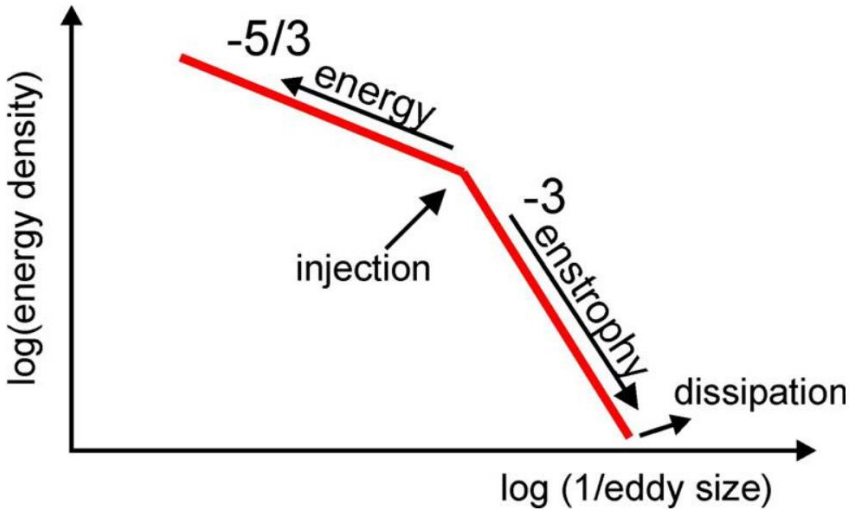

Fig. 2.1. An illustration of the energy cascade characteristic for tokamak plasma. Sourced from [28].

It should however be mentioned, that while the neutral fluid explanation provides an insight into the processes behind the turbulent energy cascade, the tokamak plasma is significantly more complicated, being a composition of two charged fluids actively interacting with the electric and magnetic fields of the tokamak.

2.1. Turbulence-driven transport in the tokamak

In the tokamak plasma, fast motion of the particles along the magnetic field lines leads to the plasma parameters variation being small in that direction, which gives it the previously mentioned 2D character. Because of this, the plasma and in particular the plasma turbulence is often described in the poloidal plane roughly perpendicular to the external magnetic field.

In these 2D cross-sections of the tokamak, plasma parameters are not homogenous [3]. Due to the localization of the heating and the radial transport of the particles and energy across the magnetic surfaces to the outside the plasma volume, the profiles of density and temperature are usually peaked at the plasma core (central area of the poloidal cross-section) with the pressure decreasing

In the presence of the pressure gradient, appearance of the random periodic perturbation of the electric potential causes a periodic perturbation of electron density. Certain effects, for example collisions can cause the "lag" in phase between the potential and density perturbation, which leads to the further accumulation of energy by the perturbation, which results in the development drift-wave turbulence (more detailed information on the mechanism can be found for example in [13]). Developed drift-wave in turn causes the local elimination of the pressure gradients.

These small-scale instabilities via the inverse energy cascade cause the development of the plasma density and temperature fluctuations at larger scales (see Fig. 2.1) which in turn lead to anomalously high transport and significant degradation of plasma particle and energy confinement [10][11]. The scale of the turbulence in the radial direction is however somewhat limited by the radial variation of the plasma perpendicular velocity [12][29], often called the velocity shear. The difference of velocity on the adjacent magnetic surfaces "breaks up" turbulent cells and causes their radial scales to dwindle. An illustration of this mechanism is given on the figure 2.1. The complete interplay between plasma flows and turbulence is, however, very complicated and is currently a topic of active research.

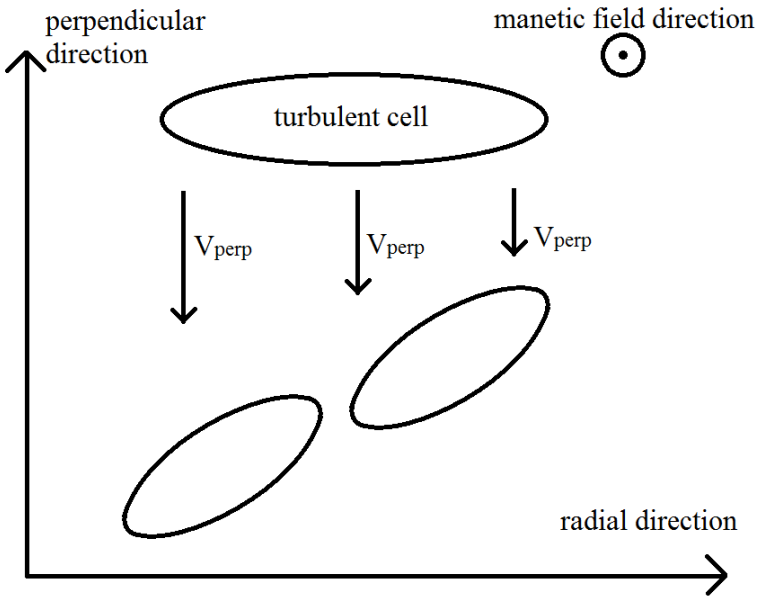

Fig. 2.2. An illustration of the shear of velocity suppressing the turbulent transport by reducing the spatial scale of the turbulence.

Besides that, the instabilities do not grow indefinitely, as there are a number of factors limiting their growth, which will be described in the latter sections. But before that, it would be useful to introduce the characteristics typically used to describe the tokamak turbulence.

2.2. Turbulence characteristics

Turbulent processes cause fluctuations of multiple plasma parameters [11][12]: density (δn), temperature of electrons (δT_e) and ions (δT_i), electric field potential ($\delta\varphi$) and magnetic field (δB). Doppler reflectometry technique, discussed in this thesis, however, focuses on measuring the density fluctuations δn, which is why they will be considered from here on out.

While plasma generally possesses toroidal geometry, if the size of the probing zone is much smaller than the minor and major radius of the plasma, to describe DR diagnostic analytically it is sufficient to consider so-called slab geometry, where Cartesian coordinate system is used for plasma parameters description. In such system x generally corresponds to radial component r of toroidal coordinate system, y corresponds to poloidal coordinate, which would normally be expressed as $r\varphi$ through poloidal angle φ. Finally, often neglected tororidal direction is substituted by z coordinate. Such a simplification neglects curvature effects, but provides the clarity toroidal system sometimes lacks. Slab geometry will be mostly used within the analytical approach of this thesis as well as in the introductory chapters 2 and 3.

Due to the random nature of the turbulence and consequently δn, it is generally described by its statistical characteristics or averaged values. The turbulence spatial scales are conveniently described by its k power spectrum in the Fourier space. Due to the 2D nature of the tokamak plasma, the spectrum is described in the following by its dependency on radial (κ) and poloidal (q) wavenumbers. Such power spectrum within the area where turbulence can be considered statistically stationary and homogenous is linked to the turbulence two-point CCF by Wiener-Khinchin theorem:

$$\langle \delta n(x,y)\delta n(x',y')^{*}\rangle = \int_{-\infty}^{\infty} \frac{1}{(2\pi)^2} |\delta n(\kappa,q)|^2 \, \mathrm{e}^{i\kappa(x-x')+iq(y-y')}\, d\kappa dq. \tag{2.2}$$

Here $|\delta n(\kappa,q)|^2$ is the power spectrum of the density fluctuations, a statistical value rather than a random one. The measure of the random turbulence amplitude is usually given by the value of δn r.m.s.

$$\delta n_{r.m.s.} = \sqrt{\left\langle \left(\delta n - \langle \delta n \rangle\right)^2 \right\rangle}. \tag{2.3}$$

While turbulence spectrum provides extensive information on the spatial characteristics of the average turbulent structure, a less precise quantity that is often directly measurable in experiment [15] is *"the correlation length"* of the turbulence. It is defined as the spatial separation at which the normalized two-point CCF of δn drops below the value of 1/e which makes it a measure of the spatial size of the average turbulent structure. Due to tokamak geometry introducing anisotropy into physical processes the poloidal and radial correlation lengths often can have different values. Moreover, the velocity shear mentioned earlier may cause the tilting of turbulent structures with respect to magnetic surfaces. As a result of this effect the turbulent structures are anisotropic, possessing two different correlation lengths

misaligned with coordinate system directions. And illustration of such situation is given by Fig. 2.3, with γ denoting the tilting angle of the turbulent structure with respect to magnetic surface.

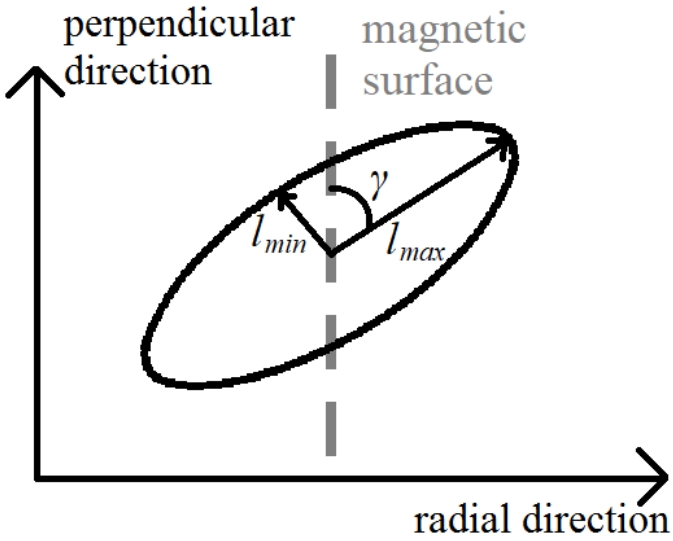

Figure 2.3. An illustration of the average turbulent structure.

Similarly to the spatial analysis, turbulence temporal behavior can be characterized. Frequency power spectrum of the turbulence can provide information on its temporal behavior and on the dispersion law, while correlation time provides the information on the time the turbulence stays correlated, a characteristic connected to the velocity of the turbulence as well as the lifetime of the turbulent eddy.

2.3. Typical tokamak instabilities

While the exact power laws differ from the ones presented on the Fig 2.1 the general turbulence spectra measured experimentally do have the characteristic knee-shape [25][30][31], with two distinct areas, the transition between which is characterized by the inverse ion Larmor radius $\rho_{ci} = \sqrt{T_i m_i}/eB$ where T_i is ion temperature and m_i is ion mass.

As it was mentioned before, the main cause of the anomalous transport in the tokamak is the drift-wave instabilities driven by the gradients on density and temperature in the plasma [11]. The four main types of instabilities are ion temperature gradient (ITG) mode, electron temperature gradient mode (ETG), trapped electron mode (TEM) and trapped ion mode (TIM) (which is often negligible, but can play a role in some cases). The term trapped here refers to the particles being trapped mainly as the plasma LFS, as mentioned in section 1.1. Due the trapped particles having a rather peculiar banana shaped (in the poloidal cross-section) trajectory they can cause instabilities specific to toroidal magnetic devices [32]. Such instabilities typically have a scale larger than the width of the “banana” in the radial direction and therefore the TIM has a much larger scale than TEM.

ITG mode [33] which is driven by the ion temperature gradient has a relative scale fulfilling $k_\perp \rho_{ci} \leq 1$. The mode is stabilized by the density gradients. This mode is often the one responsible for the anomalous transport.

ETG mode [34] possesses the smallest scale of the order of ρ_{ce}, which means that $k_{\perp}\rho_{ci} >> 1$. This mode is driven by the gradient of electron temperature and is also stabilized by the density gradient.

TEM [32] has the intermediate scale, which is wider that electron Larmor radius and can be comparable to ion one. As a result, for this mode $k_{\perp}\rho_{ci} \leq 1$. This mode is driven by both density and electron temperature gradients, but is limited by collisions, which lead to trapped particles becoming passing ones. Although collisions can also drive it causing the dissipative TEM to manifest, it was shown [32] that strong enough collisions will still act as a damping mechanism.

TIM [35] is the largest-scale mode, which possesses $k_{\perp}\rho_{ci} <<1$ and can lead to substantial transport, but is usually not the dominating instability in the tokamak discharge. Similarly to TEM, TIM is driven by ion temperature and density gradients and is limited by collisions.

An illustration of different instabilities' respective scales as well as an example of growth rates for HT-7 device is presented on the figure 2.4. The FT-2 tokamak that is going to be studied in this work is dominated by TEM instability according to the linear analysis [36].

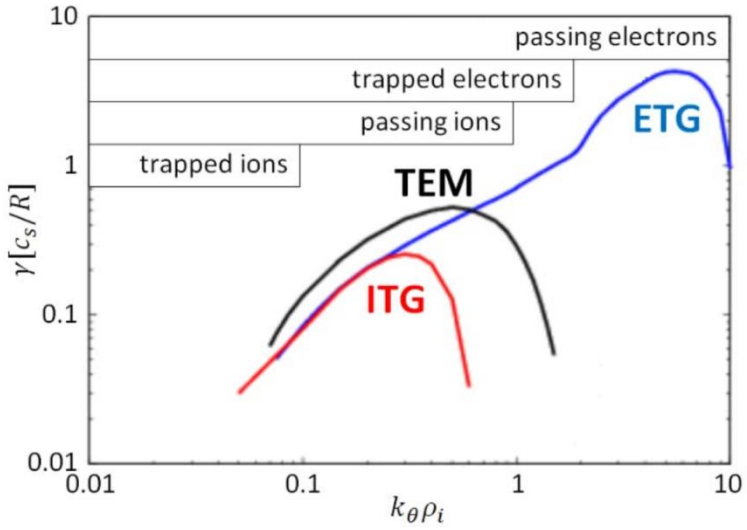

Figure 2.4. An illustration of domains corresponding to different instabilities, as well as their growth rates (expressed in the ion sound velocity divided by major radius). Sourced from [37].

2.4. Measurement of turbulence parameters

The experimental studies of drift wave turbulence have been going on for over 40 years. During this time, microwave scattering techniques have been at the forefront of the research of turbulence. A scattering technique was used as early as 1976 [38] to identify drift-wave turbulence, and later multiple studies were performed and new techniques were suggested.

Before moving on to a detailed description of microwave scattering diagnostics, however, it should be mentioned that there are other diagnostics that can also provide information on the plasma turbulence. Among such diagnostic is the laser scattering technique that have also been used for a long time [39], heavy-ion beam that can also provide information on the electric potential of the plasma [40], electron cyclotron emission diagnostic [41] that is used for measurement of the electron temperature fluctuations and their spatial correlation and beam emission spectroscopy, which also provides information plasma density fluctuations [42]. As for microwave diagnostics, nowadays microwave Doppler reflectometry is used in experiments for the measurement of poloidal wavenumber spectrum of the plasma density fluctuations

[25][30][42], which sheds the light on the instability dominating the discharge. In addition frequency spectrum of the scattered DR signal provides information on the plasma rotation velocity [17][31][43], as well as on temporal processes in plasma such as Geodesic Acoustic Modes [16]. The information about accessible measurement ranges of different diagnostics can be found for example in [14].

RCDR diagnostic supposedly measures the CCF and the radial correlation length of the density fluctuations [44][45][46][47][48], providing an estimate for the spatial size of the turbulent cells. Moreover, a technique for the reconstruction of the whole radial spectrum of the density fluctuation was suggested and implemented. Recently, RCDR was also suggested [49][50] as a tool to provide the information on the turbulence structures tilt angle, which could be crucial for distinguishing between the different drift wave instabilities.

A more detailed description of the theoretical basis behind both DR and RCDR as well as some issues that served as an inspiration for this thesis are given in the next chapter.

3. Doppler reflectometry and radial correlation Doppler reflectometry techniques

3.1. Theoretical basis

To understand the principle behind the DR and RCDR diagnostics, it is first of all necessary to understand the way electromagnetic waves propagate through the plasma. To do that it is necessary to consider Maxwell's equations in plasma with its dielectric properties and to find the solutions in the microwave range. Maxwell's macroscopic equations will be used in CGS units (the general approach of this section is inspired by [51]):

$$rot\vec{E} = -\frac{1}{c}\frac{\partial \vec{H}}{\partial t}; \qquad (3.1)$$

$$div\vec{D} = 4\pi\rho;$$

$$rot\vec{H} = \frac{4\pi}{c}\vec{j} + \frac{1}{c}\frac{\partial \vec{D}}{\partial t};$$

$$div\vec{H} = 0.$$

Here, $\vec{E}$ and $\vec{H}$ correspond to electric and magnetic fields, ρ and $\vec{j}$ correspond to the charge and the current densities induced by external forces, while $\vec{D}$ is linked to $\vec{E}$ through polarization $\vec{P}$ in a standard for dielectric substance way (magnetic permeability μ for plasma can be considered to be 1 [51]):

$$\vec{D} = \vec{E} + 4\pi\vec{P} = \hat{\varepsilon}\vec{E}. \qquad (3.2)$$

Since we are looking for the wave solution of the Maxwell equations and we are going to assume that fields change periodically at circular frequency ω so that the wave can be considered monochromatic and ∂_t can be replaced by $-i\omega$. Then, using (3.1) we can arrive to the wave equation:

$$\Delta\vec{E} - graddiv\vec{E} + \frac{\omega^2}{c^2}\hat{\varepsilon}\vec{E} = 0; \qquad (3.3)$$

$$\varepsilon_{ik} = \delta_{ik} - (4\pi i/\omega)\sigma_{ik};$$

where, $\hat{\varepsilon}$ is the plasma local complex dielectric tensor, and $\hat{\sigma}$ is conductivity tensor defined by Ohm's law. Here we implicitly assume that a linear Ohm's law is applicable to plasma, but such an assumption produces all the necessary results and is used routinely for plasma analysis. Plasma dielectric tensor in general has a rather complicated form, but we will employ a so-called "cold plasma" approximation [52], which neglects the chaotic thermal velocity of the particles in comparison with the phase velocity of the wave $\upsilon_T << \upsilon_{ph}$. Thus we neglect the kinetic effects, which cause the damping of the wave when the wavelength becomes of the order of Debye length and the mode conversion [53].

Further simplifying the model, we will consider the plasma to be stationary, which is justified by the fact that the time-scale of diagnostic microwave propagation is generally much smaller than the time scales of plasma processes (including drift-wave instabilities mentioned in previous chapter). Damping processes, such as collisional and Landau damping are also neglected in this approach. Mathematically, these simplifications are going to be expressed by the specific form of the dielectric tensor, which does not include particle velocity effects.

Assuming that a constant magnetic field $\overrightarrow{B_0}$ is acting on plasma besides the wave fields we will choose a Cartesian coordinate system with *z*-axis aligned with the external magnetic field and *x*-axis aligned with the plasma parameters' gradient (the direction of which is assumed to be perpendicular to $\overrightarrow{B_0}$, as it normally is in tokamak experiments). In such a coordinate system, the "cold" dielectric tensor takes the following form for a two single charge species plasma:

$$\hat{\varepsilon} = \begin{pmatrix} \varepsilon & ig & 0 \\ -ig & \varepsilon & 0 \\ 0 & 0 & \eta \end{pmatrix}; \tag{3.4}$$

$$\varepsilon = 1 - \frac{\omega_{pe}^2}{\omega^2 - \omega_{ce}^2} - \frac{\omega_{pi}^2}{\omega^2 - \omega_{ci}^2}; \quad g = \frac{\omega_{ce}\omega_{pe}^2}{\omega\left(\omega^2 - \omega_{ce}^2\right)} - \frac{\omega_{ci}\omega_{pi}^2}{\omega\left(\omega^2 - \omega_{ci}^2\right)}; \quad \eta = 1 - \frac{\omega_{pe}^2}{\omega^2} - \frac{\omega_{pi}^2}{\omega^2};$$

$$\omega_{px}^2 = \frac{4\pi n e^2}{m_x}, \omega_{cx} = \frac{eH}{m_x c};$$

where $x=e,i$. The frequency $\omega_{pe,i}$ is called electron (resp. ion) plasma frequency as it corresponds to the frequency of electron (resp. ion) plasma electrostatic oscillations, while ω_{cx} is electron (resp. ion) cyclotron frequency corresponding to the circular movement of the particle in magnetic field.

The formula (3.4) describes the plasma with one sort of ions having the elementary charge *e*, where *n* is the plasma density, as defined in previous chapters. Since we are considering microwaves, electron component is the one dominating the dielectric tensor while the motion of ion plasma component can be neglected. Substituting such dielectric tensor into (3.3), seeking the solution in the form of a plane wave and for now neglecting the variation of plasma parameters, we obtain:

$$\begin{aligned} &(N_y{}^2 + N_z{}^2 - \varepsilon)E_x - igE_y - N_x N_y E_z = 0; \\ &igE_x + (N_x{}^2 + N_z{}^2 - \varepsilon)E_x - N_y N_z E_z = 0; \\ &(N_x{}^2 + N_y{}^2 - \eta)E_z - N_x N_z E_x - N_y N_z E_y = 0; \end{aligned} \tag{3.5}$$

where the index components are given by $N_i=k_i c/\omega$ – normalized by c/ω components of the wavevector. This system describes "cold" modes existing in plasma. In the microwave range, the equation (3.5) has two types of nontrivial solutions each corresponding to different values of *N* components. In the case when the wave is propagating in the direction perpendicular to the external magnetic field (which is how the probing usually done), the system explicitly breaks up into two independent parts:

$$\left.\begin{aligned} &(N_y{}^2 - \varepsilon)E_x - igE_y = 0 \\ &igE_x + (N_x{}^2 - \varepsilon)E_y = 0 \\ &(N_x{}^2 + N_y{}^2 - \eta)E_z = 0 \end{aligned}\right\} \rightarrow \begin{cases} \{(N_x{}^2 + N_y{}^2 - \eta) = 0, E_x, E_y = 0; \\ \begin{cases} (N_y{}^2 - \varepsilon)E_x - igE_y = 0 \\ igE_x + (N_x{}^2 - \varepsilon)E_x = 0 \end{cases}; E_z = 0. \end{cases} \tag{3.6}$$

Two independent solutions of this system are called ordinary (O)-mode and extraordinary (X)-mode. O-mode, which is the primary object of study in analytical theory, is defined by the following dispersion relation:

$$k^2 = \frac{\omega^2}{c^2}\eta \approx \frac{\omega^2}{c^2}\left(1-\frac{n}{n_c}\right) \tag{3.7}$$

$$n_c = \frac{m_e\omega^2}{4\pi e^2}$$

For O-mode at perpendicular propagation electric field is aligned with external magnetic field. It is notable that the propagation of O-mode does not depend on the external magnetic field and is only defined by plasma density. This comes from the fact that due to O-mode polarization, the current it causes is aligned with *z* and does not "feel" magnetic field.

X-mode, for which the electric field is perpendicular to the magnetic field is defined by the dispersion relation:

$$k^2 = \frac{\omega^2}{c^2}\frac{\varepsilon^2 - g^2}{\varepsilon} = \frac{\left(\omega\left(\omega-\omega_{ce}\right)-\omega_{pe}^2\right)\left(\omega\left(\omega+\omega_{ce}\right)-\omega_{pe}^2\right)}{c^2\left(\omega^2-\omega_{ce}^2-\omega_{pe}^2\right)}. \tag{3.8}$$

The wavenumber *k* for X-mode has a much more complicated dependence on the plasma parameters, which not only includes zeroes (corresponding to the so-called cut-offs of the wave), but also special points where *k* goes to infinity (plasma resonances, correct description of which in fusion plasmas requires taking account thermal effects excluded from the "cold plasma" approximation).

The cut-off position has a meaning of the reflection point of the wave beyond which it cannot propagate. The plasma resonance of the X-mode, called upper-hybrid resonance (UHR), on the other hand corresponds to the area, where the "cold" X-mode transforms into a warm plasma mode. The explicit expressions for the X-mode cut-off and resonances can be derived from (3.8) and are as follows:

$$\omega_{cut-off}^{right} = \frac{1}{2}\left(\sqrt{\omega_{ce}^2+4\omega_{pe}^2}+\omega_{ce}\right); \tag{3.9}$$

$$\omega_{cut-off}^{left} = \frac{1}{2}\left(\sqrt{\omega_{ce}^2+4\omega_{pe}^2}-\omega_{ce}\right);$$

$$\omega^{UHR} = \sqrt{\omega_{ce}^2+\omega_{pe}^2}.$$

The dispersion relations obtained here, are however only applicable locally, where the plasma parameters can be considered constant. In general plasma is of course inhomogeneous and a more general approach is necessary. Since coordinate system is set up to have plasma inhomogeneity aligned with *x*-axis, a dependency on *x* has to be introduced into wave number *k* and refractive index *N* and moreover, the derivatives over *x* can no longer be substituted with multiplication by *ik* as it was done in (3.5). This means that to obtain the expression for the wave field the Helmholtz's equation has to be solved. For O-mode it takes the form:

$$\frac{\partial^2 E_z}{\partial x^2} + k(x)^2 E_z = 0. \tag{3.10}$$

While it some cases (for example for linear density profile resulting in Airy's equation [54]) it can be solved exactly, often an easier approach which gives all the qualitative results called Wentzel–Kramers–Brillouin (WKB) approximation is used. The idea behind this approximation is that if the medium parameters are varying slowly enough, so that the solution locally would be a plane wave, amplitude and phase of which would be given by the global dependencies of

plasma parameters. The initial solution is then assumed to have a form $E_z = A(x)\exp(i\Phi(x))$ where *A(x)* is the slowly varying amplitude while Φ*(x)* is quickly changing phase. Substituting this solution into (3.10), separating the real and the imaginary parts and neglecting slowly varying second derivative of *A(x)*:

$$\begin{cases} -\left(\frac{\partial\Phi}{\partial x}\right)^2 + k(x)^2 = 0; \\ \frac{\partial^2\Phi}{\partial x^2}A(x) + 2\frac{\partial\Phi}{\partial x}\frac{\partial A(x)}{\partial x} = 0. \end{cases} \tag{3.11}$$

And the resulting solution is:

$$E_z(x) = \frac{E_z}{\sqrt{\frac{c}{\omega}k(x)}}\exp(i\int k(x)dx). \tag{3.12}$$

The condition of the applicability of such solution is slow enough change of parameters for the second derivative of *A(x)* to be neglected, which can be rewritten as:

$$k^2(x) >> \frac{dk}{dx}. \tag{3.13}$$

This condition breaks down either in the case of very fast change of *k* over coordinate, which happens in the vicinity of plasma resonances or when the value of *k* becomes very small, which happens near the wave cut-off. Nevertheless, it turns out that WKB approximation is enough to correctly describe the wave processes in the reflectometry studies when the scattering takes place away from the cut-offs and resonances.

Now that the method for solving the Helmholtz equation has been established, the last crucial ingredient of analytical consideration can be introduced: the density fluctuations corresponding to the plasma turbulence. The turbulence does not really conform to our assumptions of plasma parameters varying slowly or only along direction *x*, but in some experimental cases (for example when the core region of plasma with no strong gradient and consequently weak turbulence is probed) it possesses low enough amplitude to be treated with the perturbation method In this approach the density is separated into background density n_0 and density fluctuations δn, which satisfy $\delta n/n_c << 1$:

$$\Delta E_z + \frac{\omega^2}{c^2}\left(1 - \frac{n_0(x) + \delta n(x,y)}{n_c}\right)E_z = 0. \tag{3.14}$$

Exploiting the small amplitude of the density fluctuations, we can first find the solution E_z^0 of unperturbed equation without fluctuations and then obtain the solution of the first order over $\delta n/n_c$ by solving the following the equation:

$$\Delta E_z^1 + \frac{\omega^2}{c^2}\left(1 - \frac{n_0(x)}{n_c}\right)E_z^1 = \frac{\omega^2}{c^2}\left(\frac{\delta n(x,y)}{n_c}\right)E_z^0. \tag{3.15}$$

It is clear from this equation that the solution of the next order will be proportional to the density fluctuations amplitude and its frequency and wavenumber will be a combination of those of the probing wave and the fluctuation itself. This mathematically illustrates the linear scattering of the probing wave that can be induced by the density perturbations. The process goes much like Bragg scattering in the solid-state physics and follows the same rules.

The amplitude of the scattered wave is proportional to that of the probing wave as well as to the amplitude of the density fluctuations. The resulting frequency is a $\omega+\Omega$, where Ω is the natural frequency of the fluctuation that caused the scattering however it can be noticed that this frequency change should stay negligible for the wave propagation. The wavenumber of the scattered wave is defined as:

$$\overrightarrow{k_{scattered}} = \overrightarrow{k_{probing}} + \overrightarrow{k_{fluctuation}}. \tag{3.16}$$

This last relation is called the Bragg rule and it is the cornerstone of the DR and RCDR diagnostics.

The formulae presented here illustrate the physical principle behind DR and RCDR diagnostics. As the wave is propagating through plasma and approaching core area with higher densities where cut-off is located, in agreement with (3.12) its amplitude grows, since the radial wavenumber is decreasing (becoming zero at cut-off) along with the radial component of the group velocity of the wave. The growth of the wave amplitude in turn means that the scattered waves closer the cut-off will have higher amplitudes too. This will be more evident in the section 3.3, where explicit expressions for the case of linear density profile will be obtained.

But the main idea behind DR diagnostic is that due to scattering signal coming from the cutoff vicinity being the strongest, it provides a natural localization of measurements while Bragg rule performs selection over the wavenumbers of the turbulence. Those facts allow to measure relative amplitude of the turbulence with a specific wavenumber at the specific area within the plasma and to ultimately obtain frequency and poloidal wavenumber spectra of the turbulence at a certain radial position. RCDR expands on the idea of the localization by measuring the correlation between to signals corresponding to slightly different probing frequencies (and consequently two close cut-off radial positions) and interpreting it as the spatial correlation of the turbulence.

The word reflectometry in the names of DR and RCDR, however, corresponds to the fact that historically the diagnostics were created as extensions of fluctuation reflectometry diagnostic, in which reflected signal rather than scattering signal was studied. Technically the more appropriate name for the two diagnostics is Doppler backscattering and radial correlation Doppler backscattering.

3.2. Measured quantities

In plasma, in most of the cases density is treated as a function of magnetic surface due to a much faster transport along magnetic field compared to the one across it. The magnetic field is generally considered to only be dependent on the major radius. As a result, the cut-off (reflective) surfaces of the waves in plasma usually roughly repeat the shape of magnetic surfaces for O-mode. For X-mode, which possesses both cut-off and resonances dependent on magnetic field, the situation is a bit more complicated. The cut-off layer is no longer directly connected to the magnetic closed surfaces or density.

The two typical situations of X-mode probing are presented on Fig 3.1. The two pictures there present the color map of density for FT-2 tokamak poloidal cross-section according to the numerical modelling results, which will be explained in more detail in later chapters. Red lines

correspond to probing frequency being equal to the right cut-off formula (3.9), while blue ones to it being equal to the UHR frequency from the same formula.

In the case of lower magnetic field (left figure), the cut-off covers the resonance making the situation suitable for the reflectometry experiment, while in the opposite case reflectometry can only be used from the LFS, otherwise the wave is absorbed in the UHR and while the scattering still can happen, it falls in the domain of enhanced scattering diagnostic, which differs from DR.

One thing that was not mentioned before is that while cut-off defines the coordinate where the total wavenumber goes to zero, reflection actually happens when the radial component of the probing beam wavenumber is zero. In the case where the wave has nonzero poloidal and toroidal wavenumber components, this point, called the turning point is located before the cut-off in the path of the wave.

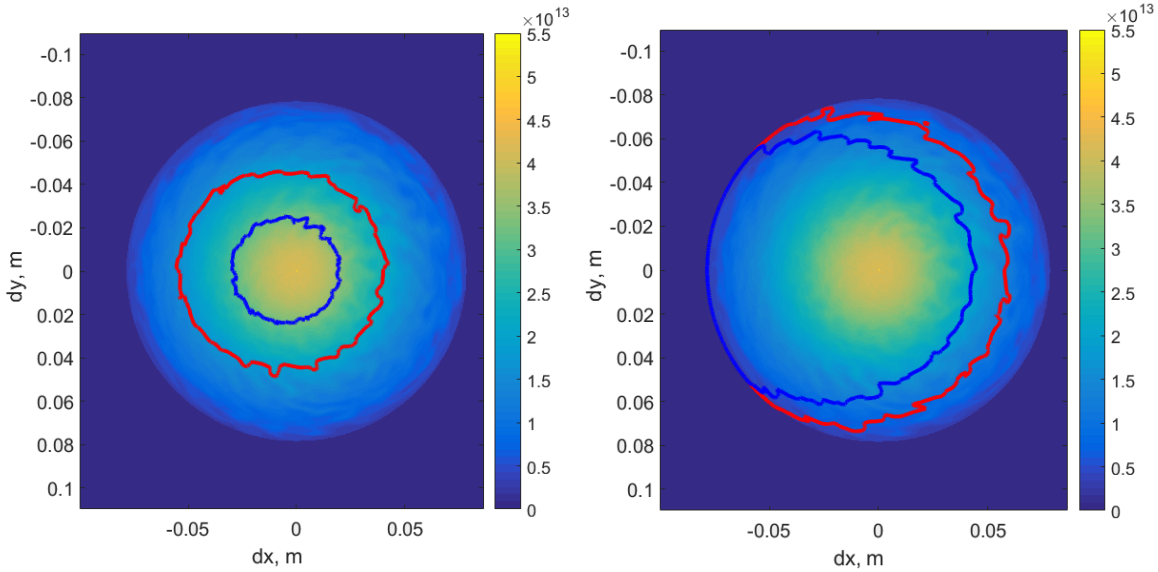

Fig 3.1. An illustration of two typical shapes of cut-off and UHR surfaces. Color map represents density, red line corresponds to cut-off for 70 GHz frequency, while blue line corresponds to UHR for the same frequency. Left figure is plotted for lower value of external magnetic field (1.7 T), while the right one corresponds to a higher one (2.2 T). Other plasma parameters of this computation will be given in the section 5.1.

As mentioned before, the DR diagnostic relies on the probing of the plasma in the presence of the cut-off at oblique incidence of the probing wave and measuring the scattering signal, supposedly coming from the vicinity of the turning point (which, as it will be shown later, is not always the case). A basic qualitative picture of the wave propagation in DR experiment is given on the figure 3.2. This picture ignores complicated volume physics of wave propagation, such as antenna radiation patterns and dispersion, but illustrates the main idea behind the diagnostic.

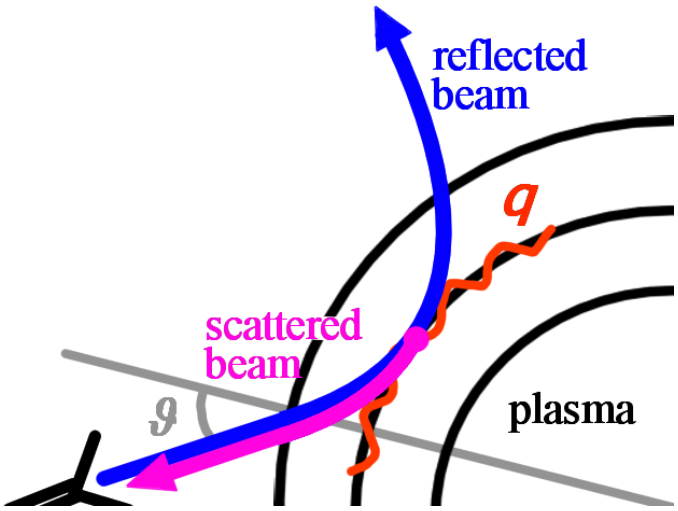

Fig. 3.2. Schematic representation of the wave propagation in DR experiment.

The probing is usually performed under oblique incidence with respect to the magnetic surface, so that the probing wave has a nonzero poloidal wavenumber makes it possible to scan over the turbulence poloidal wavenumber q by relying on the Bragg rule. Indeed, since the probing angle with respect to magnetic surface ϑ and consequently poloidal wavenumbers of the probing and scattered waves are known, it is possible to determine the poloidal wavenumber of the turbulence that cause scattering using (3.16).

Moreover, as it will be shown later, the reflected probing beam diverging away from the receiver antenna (which in our consideration is the same as the emitter one) due to nonzero poloidal wavenumber has an additional benefit of suppressing small-angle scattering signal. This signal, in the case of normal probing makes the interpretation of measurements significantly more complicated.

Temporal analysis of the received signal provides the frequency spectrum, which in turn provides the information on the mean frequency of the signal, corresponding to Doppler effect and making it possible to estimate the poloidal rotation velocity of the plasma.

The typical hardware scheme of a simple DR experimental setup is given on the Fig. 3.3.

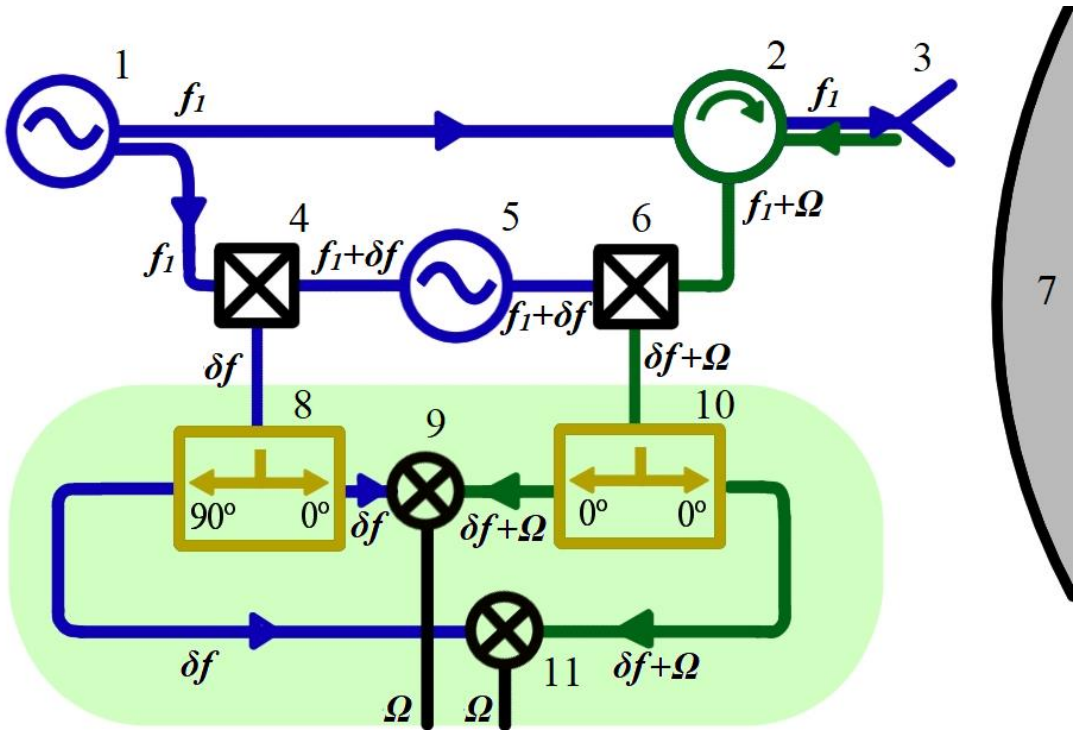

Fig. 3.3. DR experiment scheme, where 1,5 are microwave sources, 2 - circulation, 3 - antenna horn, 4,6 - microwave mixers, 7 - plasma, 8 - 90° power splitter, 9,11 -RF mixers, 10 - 0° power splitter.

This scheme corresponds to the heterodyne IQ detection (the IQ detector part is highlighted in green), which is used to measure both amplitude and phase of the scattering signal. By using 90° splitter and mixing reference and signals channels, the in-phase (*SigI*) and the quadrature (*SigQ*) parts of the signal (which can be interpreted as $A\cos\Phi$ and $A\sin\Phi$) are obtained, which in turn allows calculation of the complex signal defined as $S = SigI + i \cdot SigQ$. This technique makes temporal analysis of DR signal more detailed, since using complex signal means that distinguishing and separately measuring the variations of amplitude and the phase of the signal becomes possible. The reason two generators are used is that performing IQ detection at $\delta f << f$ produces a much better signal-to-noise ratio. To extract the turbulence spectrum at Ω, some sort of lower frequency filtration is used.

As mentioned before, DR measures two main quantities – the poloidal wavenumber spectrum of the density fluctuations and its frequency spectrum. To obtain frequency spectrum, Fourier transform of the measured IQ signal is performed and the power spectrum $P_s = S(\Omega)S(\Omega)^*$ is computed. Due to the noise and the random nature of the turbulence for this characteristic to be reliable some sort of averaging is necessary. For this reason, in experimental situations, the whole temporal span of the signal is usually divided into a set of time-windows, P_s is computed separately in each window and then averaged over all the windows. Such temporal averaging is assumed to be equivalent to statistical ensemble averaging under ergodic hypothesis. By calculating the mean frequency $f_D = \int \Omega \cdot P_s(\Omega) d\Omega \Big/ \int P_s(\Omega) d\Omega$ the Doppler shift produced by rotation velocity and turbulence phase velocity is computed as $f_D = (\upsilon_{ph} + \upsilon_{pol})q$, where q is turbulence poloidal wavenumber. This way no assumption about the shape of the spectrum is made.

A much simpler quantity is the average power of the signal, which gives information about the amplitude of the turbulence possessing the poloidal wavenumber that would satisfy the Bragg

rule (3.16) (in the case considered in this thesis the emitter and the receiver are either the same antenna or have the same pattern and position in poloidal plane, both cases will be described in more detail in chapter 5), which in the considered case is double the poloidal wavenumber of the probing wave. By either moving or tilting antenna, a scan can be performed over different turbulence poloidal wavenumbers and as a result, poloidal wavenumber spectrum can be obtained.

Now, as mentioned before, the RCDR is a modification of the DR where the plasma probing is performed at two slightly different frequencies. For heterodyne scheme presented earlier it is a natural upgrade. An example of the RCDR experiment scheme is presented on the figure 3.4.

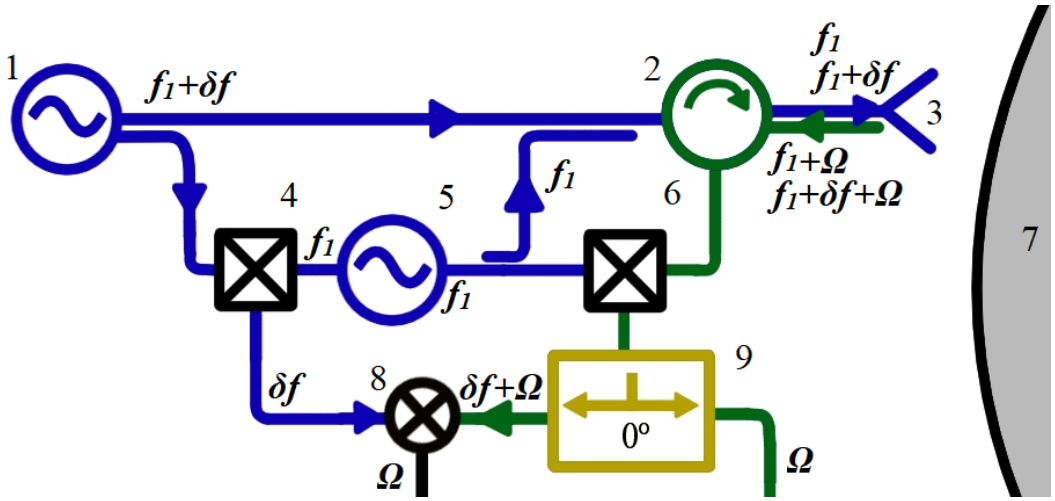

Fig. 3.4. RCDR experiment scheme, where 1,5 are microwave sources, 2 - circulator, 3 - antenna horn, 4,6 - microwave mixers, 7 - plasma, 8 -RF mixer, 9 - 0° power splitter.

The two signals measured by this scheme correspond to the scattering signals coming from the vicinity of turning points corresponding to probing frequencies of $f+\delta f$ and f. Naturally, both of these signals are present in each of the shoulders of the RF splitter, but they can be separated by the lower-frequency filtration, as long as $\delta f >> \Omega$. Once two separate temporal signals are obtained, they can be used to calculate normalized cross-correlation function (CCF):

$$CCF(\delta f,\tau)=\frac{\int\left(S_1(t)-\bar{S}_1\right)\left(S_2(t-\tau)-\bar{S}_2\right)^* dt}{\sqrt{\int\left|S_1(t)-\bar{S}_1\right|^2 dt\int\left|S_2(t)-\bar{S}_1\right|^2 dt}}. \tag{3.17}$$

The value $CCF(\delta f,0)$ provides information about the correlation between the scattering signals, and is related to the correlation between the turbulence at different radial positions (corresponding within this interpretation to the two turning points). By performing a scan over the value of δf a spatial CCF can be obtained and a radial correlation length of the turbulence can be estimated from the radial separation at which CCF decay by e.

3.3. Validity of interpretation

While the experimental approach and data analysis described in the previous section is easily implemented, rigorous theoretical studies have revealed that the interpretation of the data is not always straightforward. To illustrate the possible complications, in this section the simplest analytical consideration of the RCDR and DR diagnostics inspired by [22] is presented. The geometry and variables used here coincide with the ones presented in section 3.1 and correspond

to the slab geometry mentioned in the earlier chapters. In such geometry, magnetic surfaces and therefore cut-off surface for O-mode are planes aligned with *y* axis.

Within this model, we will solve the Helmholtz's equation (3.10) for O-mode probing and linear profile of background density $n(x)=n_c \times x/L$. In this case we do not need to resort to WKB approximation, as the solution of a 1D equation with linear potential is known to be a combination of Airy functions. Thus, the unperturbed solution will correspond to a set of Airy functions for each poloidal harmonic of the probing wave.

$$E_z^{\,0}(x,y)=\frac{1}{\pi}\int_{-\infty}^{\infty}\left(\frac{L(k_y)}{\alpha}\right)^{1/4} f(k_y)Ai\left(\frac{L(k_y)-x}{\alpha}\right)e^{ik_y y-i\frac{2}{3}\left(\frac{L(k_y)}{\alpha}\right)^{3/2}+i\frac{\pi}{4}}dk_y; \tag{3.18}$$

where $\alpha=(c^2L/\omega^2)^{1/3}$ is called Airy scale, $L(k_y)=L-\alpha^3 k_y^{\,2}$ – is a coordinate of the turning point (with L being cut-off coordinate), and $f(k_y)$ is antenna pattern, that defines the boundary condition of the equation. Now, instead of solving the equation for the next order of perturbation theory, a helpful method is using the reciprocity theorem, as explained in [55]. Using it the scattering signal in linear approximation (which we are considering by using perturbation theory) received by antenna can be computed as the following integral [56]:

$$A_s(\omega+\Omega)=i\frac{e^2\sqrt{P}}{4m_e\omega}\int_0^{\infty}\int_{-\infty}^{\infty}\delta n_\Omega(x,y)\cdot\left[E_z^{\,0}(x,y)\right]^2 dxdy. \tag{3.19}$$

Here, P is the power of the probing beam, , $E_z^{\,0}$- is the solution of the unperturbed equation (3.14), describing the probing field normalized by a unit of power, ω is circular probing frequency and Ω is the characteristic frequency of the density perturbation. Substituting (3.18) into (3.19), using Fourier images under the integral, performing the integration over x and y and assuming the probing beam to be Gaussian, one can obtain:

$$A_s(\omega+\Omega)=\frac{\alpha^2e^2}{m_ec^2}\sqrt{P}\sqrt{\frac{i\pi}{\alpha}}\int_{-\infty}^{\infty}\frac{d\kappa dq}{2\pi}\delta n_{\Omega,\kappa,q}\times \tag{3.20}$$

$$\frac{\exp\left(i\frac{(\kappa\alpha)^3}{12}-i\kappa L+i\frac{4}{3}\frac{L\omega}{c}+i\kappa q^2\frac{Lc^2}{4\omega^2}-i\frac{Lc}{2\omega}q^2-\frac{(q-2K)^2\rho^2}{4}\right)}{\left[\kappa+i\left(\frac{2Lc}{\omega\rho^2}\kappa+\frac{Lc^2}{\omega^2\rho^2}\left(q^2-\kappa^2\right)\right)\right]^{1/2}}.$$

Here $\sqrt{2}\rho$ is the probing beam waist (the distance from the axis of the beam at which the field falls by e times), K is the central poloidal wavenumber of antenna defined as $K=\omega \sin\vartheta/c$, where ϑ is once again the antenna tilt angle with respect to normal probing (which in this consideration corresponds to probing along the x direction). This expression was obtained by using a specific form of scattering efficiency, introduced in [56] and applied for example in [22]. This efficiency has its limits of validity, and when the plasma edge plays significant role, might become inapplicable (such a case will be presented for example in chapter 7). Using this expression for the scattering signal it is possible to finally calculate the CCF:

$$CCF(\Delta\omega,\Omega)=\frac{\left\langle A_s(\omega+\Omega)A_s^{\,*}(\omega'+\Omega)\right\rangle}{\sqrt{\left\langle A_s(\omega'+\Omega)A_s^{\,*}(\omega'+\Omega)\right\rangle\left\langle A_s(\omega+\Omega)A_s^{\,*}(\omega+\Omega)\right\rangle}} \tag{3.21}$$

Here the angular brackets have the meaning of the averaging over statistical ensemble of the turbulence. This definition of the CCF technically differs for formula (3.17) but for the

statistically stationary turbulence the two are equivalent and connected by a Fourier transformation. Assuming the separation of frequencies to be negligible compared to their values, the CCF can be expressed as an integral over the radial and poloidal wavenumbers of the turbulence.

$$CCF(\Delta\omega,\Omega)\approx \mathrm{e}^{-4i\frac{L\Delta\omega}{c}}\, J(\Delta\omega,\Omega)/J(0,\Omega);$$
$$J(\Delta\omega,\Omega)=\int_{-\infty}^{\infty}\frac{d\kappa dq}{2\pi}\left|\delta n_{\Omega,\kappa,q}\right|^2\frac{\exp\left(i\frac{\Delta\omega}{\omega}\left[2\kappa L+\frac{Lc}{2\omega}q^2\right]-\frac{\left(q-2K\right)^2\rho^2}{2}\right)}{\left[\kappa^2+\left(\frac{2Lc}{\omega\rho^2}\kappa+\frac{Lc^2}{\omega^2\rho^2}\left(q^2-\kappa^2\right)\right)^2\right]^{1/2}}. \tag{3.22}$$

As in previous sections, q corresponds to the poloidal wavenumber of the density fluctuation while κ – corresponds to the radial one.

Formulae (3.20) and (3.22) provide more in-depth information about the DR and RCDR diagnostics. For DR, as expected scattering signal is proportional to the amplitude of the density fluctuations and is connected to specific poloidal wavenumber of it due to exponential factor $\exp(-(q\text{-}2K)^2\rho^2/4)$ selecting $q=2K$ in formula (3.20), which justifies the poloidal wavenumber spectrum measurements. In the case of RCDR, expression (3.22) is reminiscent of Fourier transform over κ with $\Delta x=2L\Delta\omega/\omega$ (this value, however, corresponds to cut-off separation rather than usually assumed turning points' separation) which means that decay of CCF is indeed connected to the turbulence correlation length. However, the denominator casts doubt on such interpretation as might make dependence of integrand on κ narrower and lead to a massive overestimation of the radial correlation length in experiment.

Moreover, this consideration is performed within the framework of the linear (Born) approximation and is only applicable when the turbulence is weak. All this led to the fact that the interpretation of the DR and RCDR measurements still has a number of open questions, which will be described in the following sections.

3.4. Linear scattering effects

The effect the denominator of the integrand in (3.22) causes was studied analytically within the framework of Born approximation [21][22]. It is clear that the denominator becomes small in the vicinity of $q=0$, $\kappa=0$, amplifying the impact of this part of the spectrum. Thus if the main contribution into the integral comes from the vicinity of $q=0$ (which corresponds to normal probing with the respect to magnetic surface), the correlation function obtained will decay much slower than the turbulence CCF and the radial correlation length will be overestimated.

This effect is connected to the dominance of the small-angle scattering off long-scale fluctuations. Such scattering happens over a large volume of plasma and is consequently amplified. And because of this amplification measured correlation length naturally corresponds more to long-scale fluctuations and is overestimated. This analytical prediction was also confirmed within this thesis in both linear and nonlinear numerical computations (mainly in chapter 9).

Two possible solutions were offered for this issue. First of all it was shown, that for the oblique incidence of the probing beam with respect to magnetic surface, the main contribution in

the integral over q is provided by the vicinity of q=2K. This in turn means that the branching point of the integral over κ in the denominator is located at:

$$\kappa_{FS} = -\frac{2K^2 c}{\omega\left(1+i\rho^2\omega/2Lc\right)}. \tag{3.23}$$

If this value is far away from the main contribution into the integral over κ (which is normally 0). The influence of the denominator is weak. The condition on the angle of the probing was derived in [21][22]:

$$\sin^2\vartheta >> \sin^2\vartheta^{crit} = \frac{c}{2\omega l_{cx}}\sqrt{1+\frac{\rho^4\omega^2}{\left(2Lc\right)^2}}. \tag{3.23}$$

Here, l_{cx} corresponds to the radial correlation length of the density fluctuation, which is an unknown quantity in experiment. This fact complicates the use of the criterion. It was however validated within numerical calculations, where an empirical procedure was suggested to solve this issue [57]. The procedure is based on scanning the probing angle ϑ and finding the value corresponding to the coincidence of it to the critical angle for the measured correlation length. The measured correlation length associated to this value is assumed to be the right one.

An alternative approach, where the influence of the denominator was excluded mathematically was also developed. This procedure was derived and tested for both 1D [58] and 2D [22] models, validated with numerical modelling [59][60] and applied to experimental measurements. However, the FT-2 tokamak, where the method was applied, is a small research machine, where curvature effects excluded by the slab geometry model could be significant.

Recently, a study was performed to consider the impact of velocity shear causing a tilt of the turbulent structures, as described in 2.2 and the possibility of its measurement [49][50]. The study only used the simplest assumption of the RCDR CCF directly corresponding to the turbulence two-point CCF at the turning point positions. While not taking into account complications predicted by results of rigorous analytical study, a number of results was obtained and validated numerically. One of them was the procedure for extracting the value of the turbulence structure tilt angle. The procedure was based on determining t_{max} which would correspond to the maximum value of $CCF(\Delta\omega,t)$ for each value of $\Delta\omega$ and the calculation the dependence coefficient m between $\Delta y=v_{pol}t_{max}$ and Δx defined as turning point radial separation for a given $\Delta\omega$. This value was then linked to the turbulent structures tilting angle γ:

$$\frac{\Delta y}{\Delta x} = m = \cot\gamma - \tan\vartheta. \tag{3.24}$$

The illustration of the logic behind this approach is given on the figure 3.5:

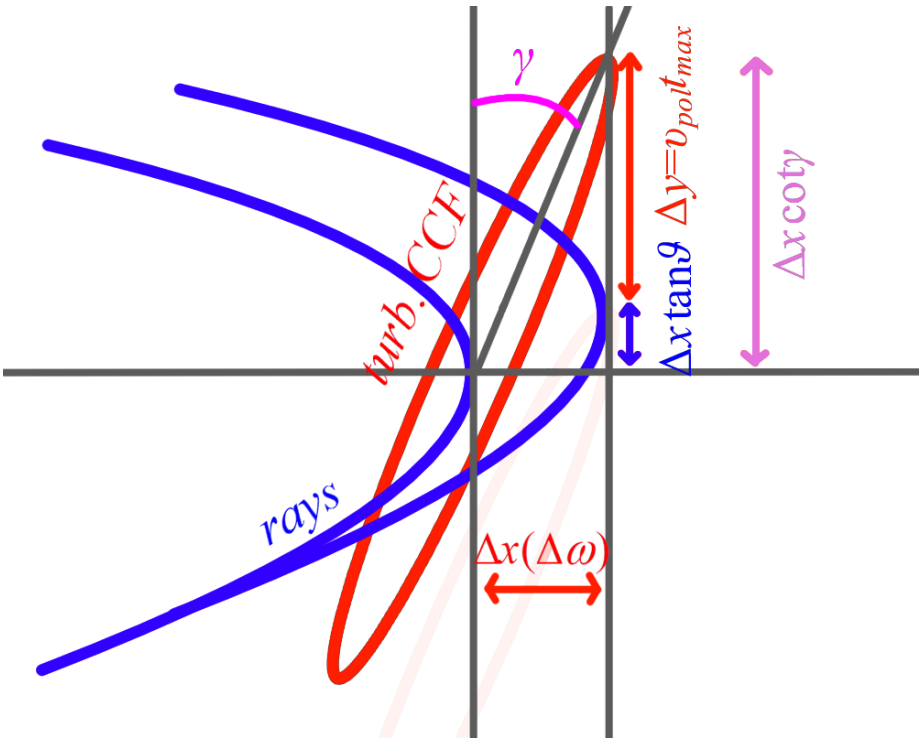

Fig. 3.5. An illustration of the logic behind the turbulent structures' tilt angle measurement technique. The maximum of RCDR CCF is assumed to correspond to temporal shift at which the structure (in red) aligns with the turning points (in blue) of the probing waves.

Such approach was applied in experiments on the ASDEX Upgrade tokamak and TJ-II stellarator, where some qualitative conclusions were obtained. However, rigorous analytical proof of feasibility of the method was not provided in the work describing such experiments [50].

3.5. Nonlinear scattering effects

Probably the biggest issues in the DR and RCDR interpretation are caused by nonlinear scattering processes. Since the interpretation of measured data is largely based on linear theory, they can make the use of the diagnostics extremely challenging. For that reason nonlinear effects have been actively studied both analytically and numerically.

The studies of the nonlinear scattering regime started with [19][20][61] considering the strongly nonlinear regime, when the probing beam is fully scattered which causes extinction of the probing line and saturation of the scattering signal power. Scattering, in this case, becomes a nonlocal random process. The peculiarity of this regime is a very weak dependence of the scattering signal on the turbulence amplitude [61]. Analytical studies on this regime have also shown that the RCDR measurements have qualitatively different dependencies on turbulence parameters, making traditional interpretation inapplicable. For example, RCDR radial correlation length depends more on the amplitude of the turbulence than its correlation length. One of the main analytical results for this case is the criterion on the density fluctuations amplitude corresponding to the onset of this regime. It is given by the expression:

$$\frac{\delta n}{n_c} >> \frac{c}{\omega\sqrt{l_{cx} L \ln\left(L / l_{cx}\right)}}. \tag{3.24}$$

Nonlinear numerical modelling was performed [57][62][63] to study this regime and the possibility of the direct interpretation of DR and RCDR results. It was shown that the measured poloidal spectrum is significantly disturbed and the radial correlation length is often underestimated (in contrast with overestimation in linear regime). On the other hand, the rotation velocity measurements did not seem to be affected by nonlinearity as predicted by analytical studies [61].

More recently, an intermediate nonlinear regime was studied analytically within the physical optics model and validated numerically [64]. This regime corresponded to multiple scattering of the probing wave could not yet be described as a random nonlocal process. By considering the double scattering process the threshold value of density fluctuations amplitude for which it overtakes the linear scattering signal was obtained and based on it the following nonlinearity onset criterion was derived:

$$\frac{\delta n}{n_c} >> \frac{c\,\mathrm{e}^{\frac{-K^2 l_{cy}^2}{4}}}{\omega\sqrt{l_{cx} L \ln\left(\frac{L}{l_{cx}}\right)}\cos\vartheta}. \tag{3.25}$$

This criterion was tested numerically both within physical optics model and full-wave computations and the results have shown a reasonable agreement with analytics. However, physical optics model neglects a number of physical effects, since plasma is considered to be a corrugated mirror and the coincidence with previous results was mostly obtained by artificial normalization. A study of this regime within the framework or strict analytical theory was not performed and has to be done.

The goal of this thesis was to not only produce an interpretation FT-2 tokamak DR and RCDR results, but also to broaden analytical understanding of the diagnostics. To that end, a few directions of analytical studies were explored:

- The impact of plasma curvature effects on the previous analytical results, namely linear model results was considered, as it could be relevant for small research machines and, in particular, for FT-2 experiment, which lies in the center of this PhD thesis.
- By the start of the thesis, an indication of nonlinear effects playing a role in experimental measurements, which will be discussed in the chapter 9, was obtained. For that reason, the study on the transient nonlinear regime was planned within the framework of the strict analytical theory.
- Finally, the mathematical apparatus used for the previous two tasks was also applied to the turbulence tilt angle measurement technique with the ultimate goal of possibly applying the technique to the FT-2 RCDR measurements available.

Most of the analytical results were also numerically validated, with an appropriate for each case numerical modelling. Before moving on to the description of the analytical study and results of the thesis, numerical methods available for the RCDR study will be described in section 4, while section 5 will give a more detailed description of the FT-2 experiment and available data.

4. Numerical modelling

There are a number of approaches, which were suggested and used for the numerical modelling of DR and RCDR diagnostics. The most common are the full-wave methods, which allow covering most of the wave propagation effects, but are very computationally demanding. For that reason simplified methods, such as computations within Born approximation described in the next section, physical optics methods employed in [64][65] or WKB-based solutions are also used. All of these models have their own ranges of applicability in limitations and selecting the model sufficient for a specific task while optimal from the computational resources standpoint is a challenge in itself. In this chapter, numerical models used within this thesis will be covered starting with the simplest ones and working our way up to the most complete model, which was used for the synthetic diagnostics.

4.1. Linear modelling tools

In some cases, there is no need for a model to include complicated nonlinear interactions of the probing wave with the plasma. Such a model could be relevant for example when the application is dedicated to analytical result validations, which were derived in linear approximation, as it will be done in the future sections of this thesis. Another possible application is the analysis of experimental results to check if a “linear” interpretation is applicable, as it was done in [45].

Such linear computations require only the evaluation of the electric field in the case of plasma unperturbed by the turbulence. This can often be done analytically, but in other cases will require numerical solution of the Helmholtz equation (3.14).

When the unperturbed field is obtained the Helmholtz equation for the next order can be solved. However an even simpler method is using the reciprocity theorem and formula (3.19) and calculating directly the signal received by the antenna. In the best case, when the unperturbed field can be found analytically, the task is simplified and only requires an evaluation of the 2D integral for each turbulence realization.

Moreover, for the analytical RCDR studies, instead of performing multiple calculations to properly describe random nature of the turbulence, expression (3.21) can be used in conjuncture with the Wiener-Khinchin theorem, to obtain result within one computation with the help of turbulence power spectrum. A detailed description and application of such an approach to validate analytical results can be found in [60]. A schematic roadmap of the linear modelling approach is given at the figure 4.1:

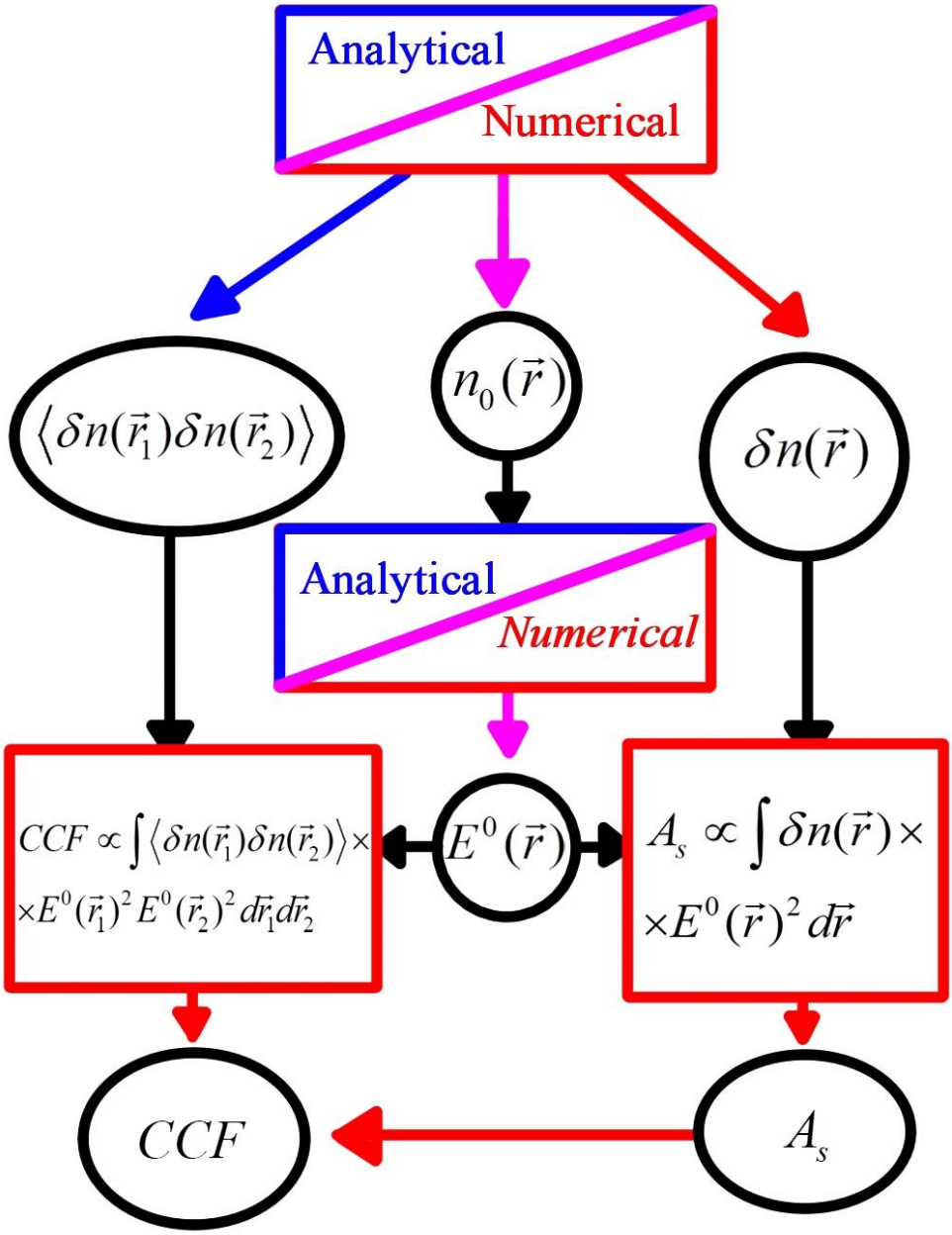

Fig. 4.1. A roadmap illustrating the approach to linear modelling of the DR and RCDR. The red color corresponds to the steps that need to be performed with numerical modelling, blue - to the steps that should be done analytically, purple - to the ones where both methods are can be used depending on the application.

Within this thesis, such an approach will be used for the validation of analytical results produced by the study of the tilted turbulence effects on RCDR, and turbulence structures tilt angle measurement technique described in section 3.4.

The main advantage of the linear reciprocity theorem approach is an extremely fast numerical computation (although in the case of benchmarking with experiment, such as [45] the main limitation comes from the plasma modelling code rather than wave propagation code). The main disadvantage is, naturally, the nonlinear effects being neglected. Another potentially problematic peculiarity of this approach is that it requires the information about the density perturbations and unperturbed profile separately. The process of extracting the fluctuations out of the full density

profile can, in principle, impose some additional limitations on the possibility of description of the low-frequency turbulence and should be performed carefully.

The limit of validity of the linear model is given by the conditions (3.24) and (3.25), except for the fact that in the case of X-mode probing an additional factor is added to it as dictated by [19][20] to account for the complicated dependence of X-mode wavenumber on the plasma parameters. However, as previously stated in the section 3.5, there is still room for exploration of the formula (3.25) within the rigorous wave theory and by the end of this thesis another condition will be obtained as a new nonlinearity criterion.

4.2. Nonlinear modelling tools

Since the end of last century, the state of art method of performing the wave propagation calculations is the so-called finite difference time domain (FDTD) computations. This approach is based on using finite difference method to estimate spatial derivatives of the quantities as the difference between the neighboring points of the spatial grid. The time derivatives then can be used to calculate the state of a wave at the next temporal step. This way, the system of Maxwell's equations (3.1) can be turned into a linear algebra problem. It is still necessary to add some version of Ohm's law to define current to complete the system, which corresponds to a linear response of the plasma. So, when we speak about nonlinearity, we are only considering the non-linear behavior of the probing wave amplitude. As a consequence, there is no way to access such nonlinear effects as soliton generation, due to the fact a second order of the plasma response is required [66]. An approach where all the components of wave field are computed is called full-wave computation and is actively used in the modelling of waves in plasma.

The current equation is usually written in cold plasma approximation, neglecting the collisions and ultimately using the dielectric tensor given by (3.4). The spatial grid is introduced, and since the electric and magnetic fields are dependent on each other's vorticity, "staggered" grids are usually used, meaning that the electric and magnetic fields are calculated on two different grids shifted by half a grid step apart. Similarly, an iterative process of calculation electric field in half a timestep then recalculating magnetic field based on it to then recalculate electric field is used. Such method was suggested by Yee in 1966 and its numerical stability was later demonstrated, although it is still a topic of active research [67]. Further details on the specifics of the Yee method and FDTD calculations in general can be found in [68].

FDTD method, unlike the Helmholtz equation solvers performs the calculation in time domain, meaning that it is necessary to perform the computation long enough to describe the studied process. Combined with the fact that numerical stability requirement also places an upper bound on the timestep size [67][68], this means that FDTD methods are rather demanding resource-wise. Although, due to the fact that normally the equation system for each grid point only includes the neighboring points (due to finite difference method), the computations can be parallelized efficiently.

The code used in this thesis project is the full-wave IPF-FD3D code [25] created by Carsten Lechte. It is used within this thesis in its 2D configuration for both validation of analytical studies and the creation of the synthetic DR and RCDR diagnostics. The full-wave computation is performed under the cold plasma approximation. As an input the code receives the matrices of background density, density perturbations and external magnetic field. The main output used is the complex amplitude recorded by receiver after an amount of time-steps sufficient to exclude

all the transient processes (propagation of incident and scattered wave, multiple scattering). The computations were performed for “frozen” turbulence, meaning that within a computation there was no temporal dependence of the density or magnetic field. This is justified by the fact that even when temporal behavior of the signal was studied, the timescale of density changes due to drift-wave turbulence (μs<) was much bigger than the timescale of wave propagation (~ns) in the studied cases. To obtain the temporal dependence a set of calculations on consecutive “frozen” snapshots of density was performed and this way the time dependence of complex amplitude was obtained.

4.3. Plasma modelling

To develop synthetic diagnostic capable of reproducing experimental results, aside from using the wave propagation code, it is imperative to have as precise density and magnetic field profiles as possible. To produce a density profile describing the perturbations of density numerical modelling is used.

The most complete description of plasma is given by the kinetic theory, where kinetic equation for particle distribution function is used. However, using kinetic approach is often challenging, and moments of the equation are calculated to produce a system of transport equations for particles, momentum and energy. Sometimes these momentum equations are transformed to obtain a system of magnetohydrodynamic (MHD) equations [3] describing plasma as a magnetized fluid.

Numerical modelling of the plasma is usually done within one of these analytical models. Oftentimes a set or transport equations is solved, with sources, sinks and transport coefficients either prescribed externally obtained by coupling with other codes. Examples of such approach is the code ASTRA [69] and B2SLOPS [70], often used for describing the core and the edge regions of the tokamak respectively. The MHD approximation, however, generally breaks down when the phase velocity and the scale of the instability becomes comparable to the velocity and the finite orbit width of the particle. That makes drift-wave instabilities unsuitable for the MHD studies and therefore a code with full kinetic description of particles rather than a fluid approach is required. Since the goal of the thesis was the creation of synthetic diagnostic measuring the parameters of drift-wave turbulence, it was necessary to use a kinetic code.

Most kinetic codes used for plasma modelling, are the gyrokinetic codes in which the kinetic equation is averaged over the gyromotion of particles around the magnetic field lines. Some of these codes solve kinetic equations directly (for example GENE code [71]), while others, including the ELMFIRE code [72] used in this thesis, use Monte Carlo method – creation of randomly generated virtual particles with statistical characteristics of the real plasma and tracking their movement to obtain the distribution functions.

Since the movement of the charged plasma particles is influenced by electric and magnetic fields, which are themselves determined by particle distribution function, an iterative approach is usually utilized. The virtual particles, corresponding to the guiding center of gyrokinetic equations, are modelled on a fine grid, a discrete of their movement is calculated based on the immediate values of the electric and magnetic fields. Based on this discretization, the distribution function is estimated by averaging to a rougher grid and based on this new distribution function fields are recalculated to be used for the next iteration of particle motions. As a result, particles

are modelled on a finer grid than fields and both parts are calculated after each other taking into account the previous modification. Such approach is called particle-in-cell modelling.

Finally, one more distinction between existing codes comes from the fact that some of them limit the computational domain and only perform the computations locally, within a part of the tokamak's volume. Global codes that include the tokamak in its entirety have the advantage of being able to describe the flows of plasma precisely but the drawback is extreme resource demands of such computations.

As previously mentioned, the code used for the modelling of FT-2 tokamak discharge studied in this thesis is the gyrokinetic ELMFIRE code [72]. ELMFIRE is a global particle-in-cell electrostatic code that computes the full distribution function of drift-kinetic electrons and ions. The code receives experimental density and temperature profiles as the input parameters and produces a self-consistent temporal evolution of density used for the full-wave modelling. It is capable of reproducing drift-wave turbulence, although, as it seems to be the case in the results presented in chapter 9, that ability can be limited by the grid resolution.

Another peculiarity is that instead of some sort of plasma magnetic equilibrium that is normally used (either calculated numerically or prescribed analytically), the magnetic surfaces in ELMFIRE are cylindrical. This means that input profiles must be cylindrically symmetrical, which is not the case in experiment. This however, is not a big issue for the FT-2 tokamak, where magnetic configuration is rather close to a cylindrically symmetrical one.

To give a better understanding on the details of the FT-2 gyrokinetic modelling as well as the reasons behind performing the complicated full-wave modelling, next chapter covers the details of the FT-2 DR and RCDR experiments, the EIMFIRE modelling results available, as well as previous effort at the creation of the synthetic diagnostics.

5. FT-2 tokamak experiment

FT-2 tokamak is a classic device with large aspect ratio, its major radius is 0.55 m and its minor radius is 0.08 m. Magnetic field supported by device is up to 3 T, the plasma current is 20-50kA and electron plasma density in the plasma core is $1\text{-}10\times10^{19}\,m^{-3}$. The tokamak operates in limiter configuration, meaning that the charged plasma particles leaving the confinement volume are deposited on a poloidally symmetrical structure at the edge of the device.

The notable feature of the device is it having circular magnetic surfaces, which allowed for simplified gyrokinetic modelling with ELMFIRE. As mentioned in the previous chapter, cylindrically symmetrical pressure profiles were used for the code model. While such an approach neglects Shafranov shift, present in magnetic configuration and shifting the center of each magnetic surface [3] for a stable magnetic configuration, the experimental values of the shift were found to be below 1 cm and the benchmarking of the modelling results seems to not have suffered due to this effect. A reasonable agreement with experimental results will be shown in chapter 9 and all the inconsistencies will be explained.

FT-2 is equipped with a set of microwave diagnostics: DR and RCDR, which are the subjects of this thesis as well as interferometry and enhanced scattering diagnostics. Interferometry was routinely used during discharges to provide electron density profile, later used for numerical modelling with ELMFIRE. Electron and ion temperature profiles also used in gyrokinetic modelling were obtained with the laser Thompson scattering and charge exchange neutral particle analyzing respectively. Spectral measurements of impurity lines in the visible region were also used to determine the ion temperature at the plasma edge.

5.1. Studied discharge

Parameters of the FT-2 ohmic discharge used for the gyrokinetic modelling and studied in this thesis are as follows: B_0=1.7 T, I_p=19 kA, $n^{max}= 4.2\cdot10^{19}\,m^{-3}$. More detailed information on the discharge as well as on experimental profiles can be found in [45][46][47].These parameters correspond to the situation presented on left side of the figure 3.1: the UHR is out of the probing zone due to the cut-off being in front of it, and consequently a reflectometry experiment can be performed. For this discharge, extensive experimental measurements were available, as well as the ELMFIRE results for these discharge conditions.

The reason, why this particular discharge was of interest, is that the measured experimentally RCDR correlation function showed a close agreement with the turbulence radial correlation length provided by ELMFIRE, as presented in [46][47]. This agreement is puzzling, since analytical theory outlined in the chapter 3 predicts a much slower decay of RCDR CCF in the linear scattering regime. The explanation for such a coincidence could be either nonlinear regime of scattering causing the RCDR CCF to decay faster or discrepancies between experiment and ELMFIRE modelling.

To gain the insight on this issue, a synthetic diagnostic was developed [45][46] using the linear approach described in section 4.1. The resulting synthetic CCF has shown a much slower decay than experimental one, suggesting that nonlinear regime of scattering is present in the experiment. As such creation of the full-wave synthetic diagnostic for this discharge seemed to

be a crucial element to improve the understanding of the experimental measurements and, thus, it became the main focus of this Ph. D. project.

The available ELMFIRE modelling results for this case included the temporal dependence of the density profile with the duration of 150 μs and the time-step of 0.15 μs (after being averaged over ELMFIRE intrinsic time step).

The computation used for further full-wave modelling and benchmarking with experiment was performed on a cylindrical grid with 100x8 radial and toroidal cells respectively, while number of poloidal cells, which adjusts the grid size to local Larmor radius, gradually increased with r from 1 point at r=0 up to 950 points at r=7 cm. This allowed for the cell size of 0.07 cm (in radial and poloidal direction) in the probing area (which corresponded to r=5.5-6 cm). Such poloidal resolution allows for poloidal wavenumbers of up to q_{max}=47 cm^{-1} to be resolved by the code at the studied minor radius (r=6 cm), which in turn allows for the value of $q\rho_s$= 2.6, where $\rho_s = \sqrt{T_e / 2T_i}\rho_i$ .and ρ_i is ion Larmor radius. These parameters mean that ELMFIRE can be used to model TEM instability, which was shown to be typical for FT-2 tokamak [36]. On the other hand, small-scale ETG instability cannot be correctly resolved by ELMFIRE, which is not a problem as the wavenumbers probed by DR are limited by $q\rho_s$= 0.7, placing ETG outside of the accessible wavenumber range. Further details on the modes of FT-2 tokamak and their modelling with ELMFIRE can be found in [45][46].

5.2. DR and RCDR setup

In case of DR and RCDR diagnostics, positions of probing antennas are illustrated on figure 5.1:

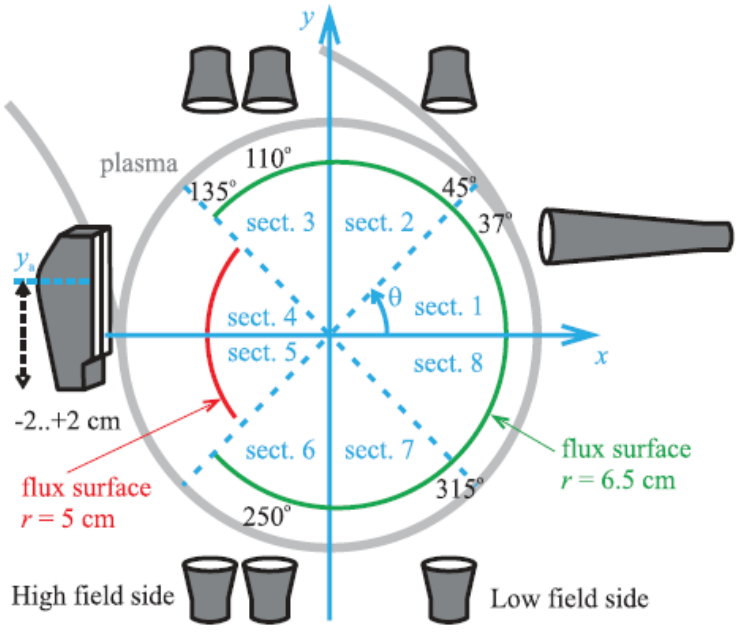

Figure 5.1. The scheme of FT-2 probing antennas, sourced from [47].

In the case of X-mode, for the studied discharge the probing was performed by a movable horizontal double antenna set located at the high-field side (HFS) of the tokamak, which could be shifted vertically from the equatorial plane up to 2 cm, allowing a scan over poloidal wavenumbers. The emitter and receiver antennae while coinciding in poloidal plane where shifted toroidally. To counteract possible toroidal mode selection, the antenna pattern in toroidal

direction was extremely wide. The central probing frequency used was f=70 GHz, which corresponds to cutoff located at r=5.5 cm. Such a setup enabled the probing of the turbulence with poloidal wavenumbers of up to q=12 cm^{-1}. For O-mode probing, a vertically aligned interferometer antenna was used, shifted from plasma core by 5 cm towards the HFS [47]. The probing was performed at the central frequency f=30 GHz with the cutoff also being located in the vicinity of r=5 cm. The turbulence wavenumber probed in this case takes the value of q=9 cm^{-1}. Beam diameter of 2 cm was utilized for both polarizations.

Due to the strong dependence of its refractive index on the plasma density, X-mode is more sensitive to nonlinearities, which, along with the fact that there were more measurements performed for it, made it the prime object of the study. O-mode was also modeled and synthetic diagnostics was developed, but less extensive study was performed.

However, before moving on to present the results of synthetic diagnostic developments and their analysis, next sections cover the analytical studies prefaced in the section 3.5. These studies also utilized numerical modelling and even full-wave numerical modelling, but with the goal of validation the theoretical results rather than that of experimental benchmarking. The studied analytical issues are relevant both for FT-2 experiment and for the DR and RCDR analysis in general.

Next chapter covers the cylindrical effects, which could be significant for a small machine such as FT-2 tokamak then the results for the tilted turbulence structures are presented in chapter 7. Chapter 8 covers the transition to the nonlinear scattering regime, which could be crucial since as it was mentioned in the previous section, the nonlinear scattering effects seem to play a role in the FT-2 RCDR experiment. Finally, in chapter 9, the synthetic diagnostics, the basics for which were laid down in this chapter will be presented.

6. Analytical study of cylindrical geometry effects

The analytical consideration presented in the chapter 3, as well as in the pioneering works on the topic [56][73][22] were performed in the slab geometry approximation, utilizing Cartesian coordinate system and neglecting the curvature geometrical effects. Such model is appropriate for large devices, but is hardly applicable to a small research machine, such as FT-2 tokamak. Thus, one of the goals of the thesis was to fill in the blanks by considering linear DR and RCDR within a more realistic cylindrical coordinate system.

To simplify the derivation, O-mode probing is considered and WKB approximation mentioned in section 3.1 is employed along with reciprocity theorem approach [55]. The new formulae are obtained for DR signal amplitude and RCDR CCF.

6.1. Basic equations

We will consider Helmholtz's equation in cylindrical geometry, and mirroring the slab geometry consideration, we will assume that the background density profile only depends on radial coordinate:

$$\frac{1}{r}\frac{\partial}{\partial r}\left(r\frac{\partial}{\partial r}E_z\right)+\frac{1}{r^2}\frac{\partial^2}{\partial \varphi^2}E_z+\frac{\omega^2}{c^2}\left[1-\frac{n(r)+\delta n(r,\varphi)}{n_c}\right]E_z=0. \tag{6.1}$$

Here, r denotes the radial coordinate and φ denotes the poloidal one. In case of cylindrical coordinates formula (3.19) takes the form:

$$A_s(\omega+\Omega)=i\frac{e^2\sqrt{P}}{4m_e\omega}\int_0^{r_a}\int_0^{2\pi}\delta n_\Omega(r,\varphi)\cdot\left[E_z{}^0(r,\varphi)\right]^2 r dr d\varphi. \tag{6.2}$$

Here P still refers to the incident probing power and ω – to probing frequency. The value r_a in this case corresponds to the minor radius of the studied device. To solve the unperturbed equation, it is useful to represent the density fluctuations with their projection in Fourier space, also referred to as Fourier image:

$$\delta n_\Omega(\vec{r})=\int_{V'}\frac{d\kappa dq}{(2\pi)^2}\exp(i\vec{Q}\vec{r})\delta n_\Omega(\kappa,q);$$
$$\vec{Q}=\left(\kappa,\frac{q}{r}\right). \tag{6.3}$$

In statistically homogeneous plasma, the turbulence spectrum is connected to the amplitude of Fourier harmonic as follows:

$$\left\langle\delta n_\Omega(\kappa,q)\delta n^*_{\Omega'}(\kappa',q')\right\rangle=(2\pi)^2\delta(\kappa-\kappa')\delta(q-q')\delta(\Omega-\Omega')\delta n^2_\Omega(\kappa,q); \tag{6.4}$$

with the angular brackets denoting the statistical averaging, same as in section 3.3. The wave-number spectrum of the density perturbations is also connected to their two-point CCF by the Wiener-Khinchin theorem (2.2), which in case of cylindrical geometry takes the form:

$$\left\langle\delta n_\Omega(\vec{r})\delta n^*{}_{\Omega'}(\vec{r}\,')\right\rangle=2\pi\delta(\Omega-\Omega')\int\frac{d\kappa dq}{(2\pi)^2}\exp(i\vec{Q}(\vec{r}-\vec{r}\,'))\delta n^2_\Omega(\kappa,q). \tag{6.5}$$

Now that we have all the expression, we will need to find the CCF, we can move on to solve the unperturbed equation (6.1). By separating variables and solving poloidal part of the equation, one can arrive to the solution:

$$E_z^{\,0} = \frac{1}{2\pi}\sum_{m=-\infty}^{\infty}\frac{g_m(r)}{\sqrt{r}}\cdot\exp(im\varphi); \tag{6.6}$$

where $g_m(r)$ is a solution of the equation:

$$\frac{\partial^2}{\partial r^2}g_m(r)+\left[\frac{\omega^2}{c^2}(1-\frac{\bar{n}(r)}{n_c})-\frac{4m^2-1}{4r^2}\right]g_m(r)=0. \tag{6.7}$$

It is also necessary to set some boundary conditions. On the external border $r=r_a$ the boundary condition is given by antenna pattern specifying the amplitude of each of the incoming poloidal harmonics. On the inner boundary $r=0$ the absence of singularity is generally used as condition. Since this area is beyond the cut-off, we will just set the solution beyond the cut-off to decrease. As a result, in the WKB approximation the unperturbed solution is given by the expression:

$$\begin{aligned}
&E_z(r,\varphi)=\frac{1}{2\pi}\sum_{m=-m_{\max}}^{m=m_{\max}}W_m(r)\,f_m\exp(im\varphi);\\
&W_m(x)=2\sqrt{\frac{8\pi\omega}{c^2k_m(r)r}}\exp\left(i\int_{r_c(m)}^{r_a}k_m(r')dr'+i\frac{\pi}{4}\right)\cos\left(\int_{r_c(m)}^{r}k_m(r')dr'+\frac{\pi}{4}\right);\\
&f_m=\sqrt{\frac{c}{8\pi}}\int_0^{2\pi}E_{in}(r,\varphi)\big|_{r=r_a}\cdot\exp(im\varphi)d\varphi;\\
&k_m(r)=\sqrt{\frac{\omega^2}{c^2}(1-\frac{\bar{n}(r)}{n_c})-\frac{4m^2-1}{4r^2}};
\end{aligned} \tag{6.8}$$

where f_m is antenna pattern over m, $k_m(r)$ is the radial wavenumber of the probing wave, $r_c(m)$ is the coordinate of the turning point for a poloidal harmonic with the wavenumber m, corresponding to the condition $k_m(r_c)=0$. The value $m_{max}=\omega r_a/c$ determines the limit on the poloidal wavenumber of the probing wave (m/r has the meaning of the poloidal component of the wave vector), under which it is able to propagate inside of plasma.

Substituting expressions (6.3) and (6.8) into (6.2) and performing the integration over poloidal coordinate, the scattered signal can be obtained as:

$$\begin{aligned}
&A_s(\omega_s)=i\frac{e^2\sqrt{P}}{4m_ec^2}\frac{1}{\pi^2}\int_{-2m_{\max}}^{2m_{\max}}\int_{-\infty}^{\infty}\int_{\max(-m_{\max}-q,-m_{\max})}^{\min(m_{\max}-q,m_{\max})}\int_{\max(r_c(m),r_c(-q-m))}^{r_a}\sqrt{\frac{1}{k_{-q-m}(r)k_m(r)}}\times\\
&\delta n_\Omega(\kappa,q)\,f_m\,f_{-q-m}\sum_{s,t=\pm1}\exp(i\Phi)\cdot dq\cdot d\kappa\cdot dm\cdot dr;\\
&\Phi=\frac{\pi}{2}+\int_{r_c(m)}^{r_a}k_m(r')dr'+\int_{r_c(-q-m)}^{r_a}k_{-q-m}(r')dr'+\\
&+s\left(\int_{r_c(m)}^{r}k_m(r')dr'+\frac{\pi}{4}\right)+t\left(\int_{r_c(-q-m)}^{r}k_{-q-m}(r')dr'+\frac{\pi}{4}\right)+\kappa r;
\end{aligned} \tag{6.9}$$

where κ and q/r in agreement with (6.3) are the radial and poloidal wavenumbers of the density perturbation respectively. To simplify further derivation, the discrete sum over m and q will be replaced by a continuous integral, which is justified by the weak change of the integrand when m and q and varied by 1. The complicated form of integration limits is caused by the fact that outside these limits the wave does not propagate into plasma and the electric field exponentially decays instead.

From the expression (6.9) it can be seen that the integrand involves the term the phase of which is changing relatively fast ($s=t$) and relatively slow ($s=-t$). The slower varying members correspond to the wave, which after scattering at the point r is propagating in the same radial direction (which corresponds to forward-scattering). In the case of the other terms, the wave is scattered backwards at the point r and comes back to antenna after going through the turning point zero or two times. An illustration of ray trajectories for such waves is presented at the Fig. 6.1. Due to this circumstance, the $s=t$ terms will be designated at backscattering (BS) ones and the $s=-t$ members will be called forward-scattering (FS). They are qualitatively different and will be considered separately.

The definition of the forward scattering here does not directly correspond to the small-angle scattering mentioned before. Forward scattering describes any scattering that leads to the wave not changing the direction of its propagation along the radial coordinate. Small-angle scattering introduced in chapter 3 refers to the scattering on the turbulence with the small values of wavenumbers q and κ, which happens over a large radial volume and therefore dominates the scattering signal. While these two terms are different, it will be evident from the next sections of this chapter, that small-angle scattering is a subset of forward scattering, as both correspond to small values of κ.

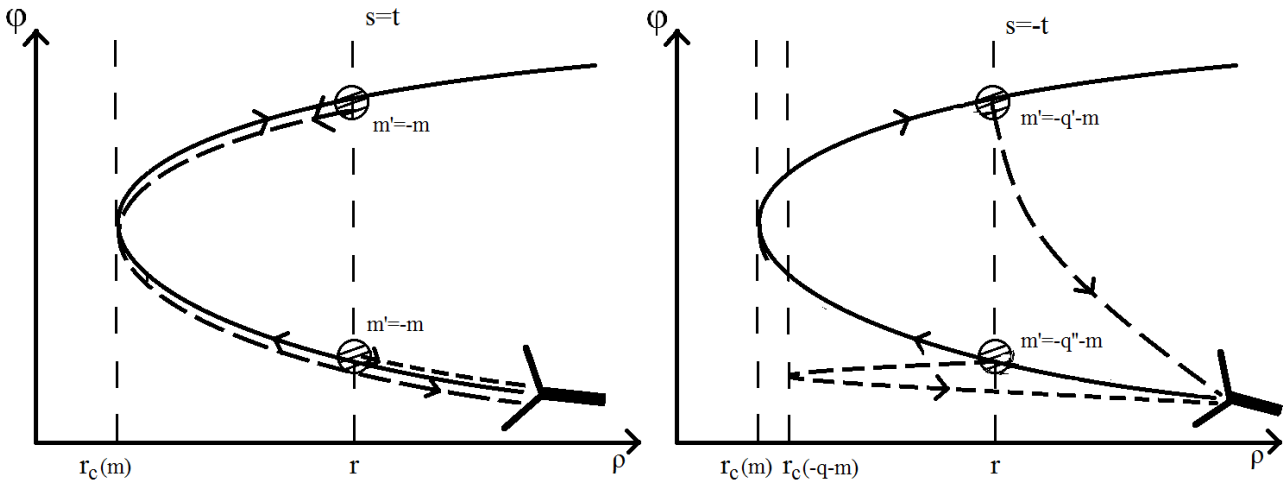

Fig. 6.1. An illustration of ray trajectories for back-scattering and forward scattering.

6.2 BS signal

In the case of BS, fast variations of the integrand phase allow to compute an integral with the stationary phase method. The method is applicable everywhere expect for the cut-off vicinity, where the WKB approximation itself fails. A more precise condition of validity will be presented later. The stationary phase point r_{st} for which the phase derivative becomes zero [74][75] is given by an expression:

$$k_m(r_{st}) + k_{-q-m}(r_{st}) = -s\kappa. \tag{6.10}$$

This condition (which was the previously mentioned in chapter 3 Bragg rule) defines the radial wavenumber of the fluctuations that produce the main contribution to the scattering signal from the point r_{st}, or put another way it defines the area or the main contribution for each turbulence wavenumber. Performing the integration over r in (6.9) we obtain the following expression:

$$A_s^{BS} = i\frac{e^2\sqrt{P}}{m_e c^2}\frac{1}{2\pi^{3/2}}\int_{-2m_{\max}}^{2m_{\max}}\int_{-2\frac{\omega}{c}}^{2\frac{\omega}{c}}\int_{\max(-m_{\max}-q,-m_{\max})}^{\min(m_{\max}-q,m_{\max})}\delta n_\Omega(\kappa,q)\sqrt{\frac{L^3(r_{st})}{\kappa}}f_m f_{-q-m}\times$$

$$\exp(i\Phi(r_{st}) - i\frac{\pi}{4})\cdot dq\cdot d\kappa\cdot dm; \tag{6.11}$$

$$\alpha_c(r) = \left(\frac{(4m^2-1)}{2r_{st}^3} - \frac{\omega^2}{c^2}\frac{d}{dr}\frac{n(r)'}{n_c}\bigg|_{r_{st}}\right)^{-1/3}.$$

The integration limits for the integral over κ changed since not every value has a stationary phase point corresponding to it. The physical meaning of the fact is that fluctuations with too high absolute value of κ are unable to satisfy the Bragg rule anywhere in the plasma volume and therefore they do not provide significant input into the scattering signal in the linear approximation. Parameter α_c is connected to the scale at which the radial wavenumber changes, and in the limit of the slab geometry ($r_c \sim r_{st} \sim r_a >> r_a - r_{st}$) it becomes the well-known Airy scale:

$$\alpha_c(r) = \left(\frac{(4m^2-1)}{2r^3} - \frac{\omega^2}{c^2}\frac{d}{dr}\frac{n(r)'}{n_c}\bigg|_{r}\right)^{-1/3} \approx \left(\frac{(4m_{\max}{}^2-1)}{2r^3} + \frac{\omega^2}{c^2 L_n}\right)^{-1/3} \approx \left(\frac{\omega^2}{c^2 L_n}\right)^{-1/3} = \alpha. \tag{6.12}$$

To continue the derivation we will assume that antenna has a Gaussian pattern:

$$f_m = \frac{(2\sqrt{\pi}\rho)^{1/2}}{r_a}\exp\left(-\frac{(\frac{m}{r_a} - K)^2\rho^2}{2}\right). \tag{6.13}$$

Here, $K = \omega \times \sin\vartheta / c$ is the central poloidal wavenumber of the probing wave (with ϑ being the probing angle with respect to normal probing) and 2ρ is the diameter of the probing beam. After substituting (6.13) into (6.11), integral over m can be calculated with a saddle point method [74][75]. The saddle point is given by the condition $m = -q/2$ (which also corresponds to the Bragg rule), while the scattering signal is represented by an integral over the turbulence wavenumbers:

$$A_s^{BS} = i\frac{e^2\sqrt{P}}{m_e c^2}\frac{1}{\sqrt{\pi}}\int_{-2m_{\max}}^{2m_{\max}}\int_{-\omega/c}^{-\omega/c}\delta n_\Omega(\kappa,q)B(\kappa,q)dqd\kappa; \tag{6.14}$$

where $r_c=r_c(-q/2)$,

$$B(\kappa,q)=\sqrt{\frac{\alpha_c{}^3(r_{st})}{\kappa r_a^2}}\frac{\exp\left(2i\int_{r_c}^{r_a}k_{-q/2}(r')dr'+2is\left(\int_{r_c}^{r_{st}}k_{-q/2}(r')dr'+\frac{\pi}{4}\right)+i\kappa r_{st}-\left(K+\frac{q}{2r_a}\right)^2\rho^2\right)}{\left(\frac{1}{2}\frac{d^2\Phi}{dm^2}\right)^{1/2}\Big|_{m=-q/2}}.$$

The general expression for the second derivative of the integrand phase is rather overwhelming, but it can be simplified in the case of $\kappa<<\omega/c$ which corresponds to the maximum of the integrand:

$$\left(\frac{1}{2}\frac{d^2\Phi}{dm^2}\right)^{-1/2}\Big|_{m=-q/2}=\left(-\Lambda(r_a)+\frac{q^2\alpha_c(r_c)^3}{\kappa r_c^4}+i\frac{\rho^2}{r_a^2}\right)^{-1/2}; \tag{6.15}$$

where $\Lambda(r)=\int_{r_c}^{r}\frac{dr'}{r'^2k_{-q/2}(r')}$.

As a result, the integrand takes the form:

$$A_s^{BS}=i\frac{e^2\sqrt{P}}{m_ec^2}\frac{1}{\sqrt{\pi}}\int_{-2m_{max}}^{2m_{max}}\int_{-\omega/c}^{-\omega/c}\frac{\delta n_\Omega(\kappa,q)\exp(i\Psi)}{\sqrt{\frac{q^2r_a^4}{r_c^4\rho^2}+\frac{\kappa r_a^2}{\alpha_c{}^3(r_c)}\left(\Lambda(r_a)\frac{r_a^2}{\rho^2}-i\right)}}dqd\kappa; \tag{6.16}$$

$$\Psi=2\int_{r_c}^{r_a}k_{-q/2}(r')dr'+2s\left(\int_{r_c}^{r_{st}}k_{-q/2}(r')dr'+\frac{\pi}{4}\right)+\kappa r_{st}+i\left(K+\frac{q}{2r_a}\right)^2\rho^2\approx$$

$$2\int_{r_c}^{r_a}k_{-q/2}(r')dr'+\frac{\kappa^3\alpha_c{}^3(r_c)}{12}+\kappa r_c+i\left(K+\frac{q}{2r_a}\right)^2\rho^2.$$

Here, the first three terms correspond to the phase the probing wave gains while propagating through plasma before and after scattering, while the last term corresponds to the antenna pattern acting as a filter over poloidal wavenumbers. Finally, it should be noted that the sign of s in the phase of BS signals corresponds to the sign of κ, as can be seen from (6.10). The meaning of that is that the fluctuations with positive radial wavenumber cause BS before the turning point, while the ones with negative κ scatter the wave after the turning point (see Fig. 6.1).

6.2. FS signal

For the FS terms, we will start by performing integration over m with the saddle-point method and then calculate the integral over the radial coordinate. The saddle point m_s in this case is given by a condition:

$$m_s=-q/2+q\left(\frac{s\Lambda(r)}{2\Lambda(r_a)-2i\frac{\rho^2}{r_a^2}}\right). \tag{6.17}$$

The difference from $m=-q/2$ in this case is explained by the fact that FS utilizes non-central part of antenna pattern. Indeed, if we were to set ρ to be infinite (plane wave description), we

would arrive to the normal Bragg condition. Also, considering the main contribution in the integral (as will be shown further) is produced by the turning point vicinity, where $\Lambda(r)<<\Lambda(r_a)$, we will assume that the second term in (6.17) is small in comparison with the first one. Therefore, we will neglect it everywhere except for the phase of the integrand, where is will be used as a small value over which the Taylor series will be expanded. Performing the integration over m in the formula (6.9) we obtain:

$$A_s(\omega_s) = i\frac{e^2\sqrt{P}}{2m_e c^2}\frac{\rho}{\pi {r_a}^2}\int_{-2m_{\max}}^{2m_{\max}}\int_{-\infty}^{\infty}\int_{r_c}^{r_a}\frac{1}{k_{-q/2}(r)\sqrt{\Lambda(r_a)-i\frac{\rho^2}{{r_a}^2}}}\delta n_\Omega(\kappa,q)\exp(i\Psi)\cdot dq\cdot d\kappa\cdot dr;$$

$$\Psi = \frac{\pi}{4}+\int_{r_c(m_s)}^{r_a}k_{m_s}(r')dr'+\int_{r_c(-q-m_s)}^{r_a}k_{-q-m_s}(r')dr'+s\left(\int_{r_c(m_s)}^{r}k_{m_s}(r')dr'-\int_{r_c(m_s)}^{r}k_{-q-m_s}(r')dr'\right)+ \qquad (6.18)$$

$$\kappa r+\frac{i}{2}\left(\frac{-q-m_s}{r_a}-K\right)^2\rho^2+\frac{i}{2}\left(\frac{m_s}{r_a}-K\right)^2\rho^2\approx$$

$$\frac{\pi}{4}+2\int_{r_c}^{r_a}k_{-q/2}(r')dr'+\frac{1}{2}\frac{q^2\Lambda(r)^2}{\Lambda(r_a)-i\frac{\rho^2}{{r_a}^2}}+\kappa r+i\left(\frac{q}{2r_a}+K\right)^2\rho^2.$$

To calculate the integral over r in (6.18), we will notice that the main contribution comes from the vicinity of the cut-off r_c. Thus, the radial component of the probing wave wavenumber in can be expanded into Taylor series around the turning point, which allows us to rewrite the integral as:

$$A_s(\omega_s) = i\frac{e^2\sqrt{P}}{2m_e c^2}\frac{\rho}{\pi {r_a}^2}\int_{-2m_{\max}}^{2m_{\max}}\int_{-\infty}^{\infty}\int_{r_c}^{r_a}\frac{{\alpha_c}^{3/2}(r_c)}{\sqrt{r-r_c}\sqrt{\Lambda(r_a)-i\frac{\rho^2}{{r_a}^2}}}\delta n_\Omega(\kappa,q)\exp(i\Psi)dqd\kappa dr;$$

$$\Psi = \frac{\pi}{4}+2\int_{r_c}^{r_a}k_{-q/2}(r')dr'+\frac{q^2L^3(r_c)}{\left(\Lambda(r_a)-i\frac{\rho^2}{{r_a}^2}\right){r_c}^4}(r-r_c)+\kappa r+i\left(\frac{q}{2r_a}+K\right)^2\rho^2. \qquad (6.19)$$

Now the integral over r can be directly calculated and we obtain the final expression for the FS terms. Last thing to note is that expression (6.19) does not depend on s. This means that both trajectories corresponding to FS on the figure 6.1 in our approximation provide the same contribution for both signs of κ, which means that the total FS signal should be obtained by doubling (6.14).

$$A_s(\omega_s) = i\frac{e^2\sqrt{P}}{m_e c^2}\frac{1}{\sqrt{\pi}}\int_{-2m_{\max}}^{2m_{\max}}\int_{-\infty}^{\infty}\frac{{\alpha_c}^{3/2}(r_c)}{\sqrt{\frac{q^2}{{r_a}^2}\frac{{\alpha_c}^3(r_c){r_a}^4}{{r_c}^4\rho^2}+\kappa\left(\Lambda(r_a)\frac{{r_a}^2}{\rho^2}-i\right)}}\delta n_\Omega(\kappa,q)\times \qquad (6.20)$$

$$\exp\left\{i\frac{\pi}{4}+2i\int_{r_c}^{r_a}k_{-q/2}(r')dr'+i\kappa r_c-\left(\frac{q}{2r_a}+K\right)^2\rho^2\right\}\frac{dq}{r_a}d\kappa.$$

Expressions for BS and FS terms coincide in absolute value but have some difference in the phase. These differences, however will not impact the CCF. Also, it should be noted that in the slab geometry limit expression (6.16) coincides with the one obtained in [22].

6.3. Total signal and CCF

To obtain the total scattering signal, in principle, the BS and FS contributions, given by (6.16) and (6.20) should be added. However, due to the limitations of the WKB approximation, the domains of their validity complement each other instead of coinciding with each other. Indeed, the WKB approximation is inapplicable in the vicinity of the cut-off, where the condition of validity is violated (This is a reiteration of the formula (3.13)):

$$k_m(r)^2 >> \frac{d}{dr} k_m(r). \tag{6.21}$$

When approaching the turning point, the WKB solution of (6.7) increases indefinitely and becomes substantially bigger than the exact solution. Therefore, if the main contribution in the integral (6.9) over r is coming from the vicinity of the turning point, the precise scattering signal will be much smaller than our result. It can be estimated by the value at the limit of validity of WKB approximation.

In case of BS terms, the main contribution is provided by the stationary phase point (given by (6.10)). The condition (6.21) in this case provides a lower bound of the κ values, given by the condition:

$$\frac{\kappa^3 \alpha_c^{\,3}}{4} >> 1. \tag{6.22}$$

In the slab geometry case, α_c would be substituted by Airy scale. When the turbulence radial wavenumbers are lower than this limit, expression (6.16) becomes inapplicable and the exact contribution of BS is much smaller than that of (6.16) and that of FS (6.20).

In the case of the FS, on the other hand, the main contribution is always provided by the vicinity of the turning point of the size $(r - r_c) \sim \left(\kappa + \frac{q^2 \alpha_c^{\,3}(r_c)}{\left(\Lambda(r_a) - i \frac{\rho^2}{r_a^{\,2}} \right) r_c^{\,4}} \right)^{-1}$, with part of this area $(r - r_c) < \alpha_c(r_c)$ being the area where WKB constraints are not fullfilled. For the expression (6.20) to be valid, we need the area of the main contribution be a lot wider that the area of WKB constraints violation. This provides the criterion of validity of (6.20) given by the following expression:

$$\left(\kappa+\frac{q^2\alpha_c{}^3(\mathrm{r}_c)}{\left(\Lambda(r_a)-i\frac{\rho^2}{r_a{}^2}\right)r_c{}^4}\right)\alpha_c(\mathrm{r}_c)<<1. \tag{6.23}$$

Finally, it should be noted that for $\kappa \sim q/r_c$ the second term in the left-hand part is much smaller than the first one and can be neglected. Thus, the area of validity of expressions (6.16) and (6.20) complement each other, while their parameter dependencies coincide. In the intermediate area $\kappa \sim \alpha_c(r_{st})^{-1}$, the result can be obtained by extrapolating the two expressions. Similar result was obtained within the analysis of WKB approach in rigorous 1D analysis in [58]. Since the formula (6.16) coincides with (6.20) for $\kappa\ \alpha_c(r_c)<<1$(which corresponds to stationary phase point over r being close to the turning point), in practice it correctly describes the scattering signal in the whole parameter range and will be used next to obtain the expression for the CCF. Also, as mentioned previously formula (6.23) illustrates the fact that forward scattering indeed happens on small values of κ.

The normalized CCF is given by the expression:

$$CCF(\Delta\omega,\Omega)=\frac{\left\langle A_s(\omega+\Omega),A_s{}^*(\omega+\Delta\omega+\Omega)\right\rangle}{\sqrt{\left\langle A_s(\omega+\Omega),A_s{}^*(\omega+\Omega)\right\rangle\left\langle A_s(\omega+\Delta\omega+\Omega),A_s{}^*(\omega+\Delta\omega+\Omega)\right\rangle}}. \tag{6.24}$$

Using expression (6.16) and neglecting the coefficient which will be removed by normalization:

$$\left\langle A_s(\omega+\Omega),A_s{}^*(\omega+\Delta\omega+\Omega)\right\rangle \sim \int_{-2m_{\max}}^{2m_{\max}}\int_{-\omega/c}^{\omega/c} dqd\kappa\left|\delta n_\Omega(\kappa,q)\right|^2 \sqrt{\frac{\alpha_c{}^3(r_{st})}{\kappa r_a{}^2\left(\frac{1}{2}\frac{d^2\Phi}{dm^2}\right)^{1/2}\Big|_{m=-q/2}}}\times \tag{6.25}$$

$$\exp\left(2i\int_{r_c}^{r_a}\frac{\omega^2}{c^2k_{-q/2}(r')}dr'\frac{\Delta\omega}{\omega}-2i\frac{\kappa}{|\kappa|}\left(\int_{r_c}^{r_{st}}\frac{\omega^2}{c^2k_{-q/2}(r')}dr'\right)\frac{\Delta\omega}{\omega}\right)\times$$

$$\exp\left(-\frac{1}{2}\left(2K+\frac{q}{r_a}\right)^2\rho^2-\left(2K+\frac{q}{r_a}\right)\rho^2K\frac{\Delta\omega}{\omega}-\rho^2\left(K\frac{\Delta\omega}{\omega}\right)^2\right).$$

The exponential argument here was simplified by expanding it into Taylor series over $\Delta\omega/\omega$ (such simplification is applicable in the case when the position of stationary and turning points corresponding to different frequencies are close enough so that Φ and Ψ do not change significantly). Further simplification can be obtained for narrow antenna patterns, which are usually used in DR experiments. Assuming the beam radius is much greater than the poloidal correlation length of the turbulence ($\rho>>l_{cy}$), the integral over q in (6.25) can be estimated and CCF in the form of the integral over radial wavenumbers of the turbulence can be obtained:

$$\left\langle A_s(\omega+\Omega), A_s^*(\omega+\Delta\omega+\Omega)\right\rangle \sim \int_{-\omega/c}^{\omega/c} \left|\delta n_\Omega(\kappa,-2Kr_a)\right|^2 \left|\frac{2\alpha_c{}^3(r_{st})}{\kappa r_a^2 \left.\frac{d^2\Phi}{dm^2}\right|_{m=Kr_a}}\right| \times$$
$$\exp\left(2i\int_{r_c}^{r_a}\frac{\omega^2}{c^2 k_{Kr_a}(r')}dr'\frac{\Delta\omega}{\omega} - 2i\frac{\kappa}{|\kappa|}\left(\int_{r_c}^{r_{st}}\frac{\omega^2}{c^2 k_{Kr_a}(r')}dr'\right)\frac{\Delta\omega}{\omega} - \frac{1}{2}\left(\frac{\rho\sin\vartheta}{c}\Delta\omega\right)^2\right)d\kappa. \tag{6.26}$$

This expression can be further simplified by assuming the turbulence to be long-scale so that $\kappa c/2\omega << 1$, in which case the $k_{Kr_a}^2(r)$ can be approximated by the linear dependence around the turning point. The expression for CCF in this case takes the form:

$$\left\langle A_s(\omega+\Omega), A_s^*(\omega+\Delta\omega+\Omega)\right\rangle \propto \int_{-\omega/c}^{\omega/c} \left|\delta n_\Omega(\kappa,-2Kr_a)\right|^2 \times$$
$$\frac{\alpha_c{}^3(r_c)\exp\left(i\int_{r_c}^{r_a}\frac{dr'}{k_{Kr_a}(r')}\frac{\delta r}{\alpha_c(r_c)^3} - i\kappa\delta r - \left(\frac{\rho\sin\vartheta}{2\alpha_c(r_c)^3}\frac{c}{\omega}\delta r\right)^2\right)}{\sqrt{\left(4K^2\frac{\alpha_c{}^3(r_{st})r_a{}^4}{r_{st}{}^4\rho^2} + \Lambda(r_a)\frac{r_a{}^2}{\rho^2}\kappa\right)^2 + \kappa^2}}d\kappa. \tag{6.27}$$

where

$$\delta r = 2\left(\frac{c^2}{\omega^2}\frac{((2Kr_a)^2-1)}{2r_c^3} - \frac{d}{dr}\left.\frac{n(r)}{n_c}\right|_{r_c}\right)^{-1}\frac{\Delta\omega}{\omega} = 2\frac{\omega^2}{c^2}\alpha_c(r_c)^3\frac{\Delta\omega}{\omega}. \tag{6.28}$$

The formula (6.27) also coincides with the results obtained in [22] in the slab geometry limit, in which case parameter δr has the meaning of the cut-off separation. In the general case, however, there is no simple interpretation for the meaning behind δr.

If we were to use the expression (6.20) instead of (6.16) for the CCF calculation, we would arrive to the (6.27) right away. More general expression (6.25) is, as it will be shown next, important in the case of small-scale turbulence, for which the stationary phase point (which is also the Bragg resonance point) is located far from the turning point.

Similarly, to [22], at high enough probing angle the denominator dependence in the area of the main contribution becomes negligible and a criterion for small-angle scattering suppression can be obtained:

$$\sin\theta^2 > \frac{c^2 r_c{}^4\Lambda(r_a)}{4\omega^2 r_a{}^2\alpha_c{}^3(r_c)l_{cr}}\sqrt{1+\frac{\rho^4}{\Lambda(r_a)^2 r_a{}^4}}. \tag{6.29}$$

Pushing the similarity further, the procedure for the turbulence radial spectrum reconstruction can also be determined in our more general consideration. Indeed, formula (6.27) can be interpreted as a Fourier transform and can therefore be used to obtain the turbulence radial spectrum. Expressing $\Delta\omega$ through δr we can obtain:

$$\left|\delta n_{\Omega}(\kappa,-2Kr_a)\right|^2 \propto \frac{\sqrt{\left(4\frac{K^2\alpha_c{}^3(r_c)r_a{}^4}{r_c{}^4\rho^2}+\Lambda(r_a)\frac{r_a{}^2}{\rho^2}\kappa\right)^2+\kappa^2}}{\alpha_c{}^3(r_c)}\int_{-\infty}^{\infty}\exp\left(\frac{\delta r^2}{8}\left(\frac{c\rho}{\omega}\sin\vartheta\alpha_c{}^{-3}(r_c)\right)^2\right)\times$$

$$\exp\left(i\kappa\delta r-i\alpha_c{}^{-3}(r_c)\int_{r_c}^{r_a}\frac{dr'}{k_{Kr_a}(r')}\delta r\right)\left\langle A_s(\omega+\Omega),A_s{}^*(\omega+\frac{c^2}{2\omega\alpha_c(r_c)^3}\delta r+\Omega)\right\rangle d(\delta r). \qquad (6.30)$$

The phase term $\exp\left(-i\alpha_c(r_c)^{-3}\int_{r_c}^{r_a}\frac{dr'}{k_{Kr_a}(r')}\delta r\right)$ corresponds to the phase the wave acquires while moving from the antenna to the turning point and can be compensated experimentally.

Strictly speaking, this procedure is only applicable for the turbulence satisfying $\kappa c/2\omega<<1$, since it is based on (6.27). A more rigorous approach would require the use of the formula (6.26), where a full second derivative of the phase $\left.\frac{d^2\Phi}{dm^2}\right|_{m=-q/2}$ is used rather than a simplified expression (6.15). The integral over $\Delta\omega$ just like in the large-scale turbulence case can be considered a Dirac delta-function $\delta\left(\int_{r_c}^{r_{st}(\kappa)}\frac{dr'}{\alpha_c{}^3(r_c)k_{Kr_a}(r')}-\kappa'\right)$, which helps to estimate the wavenumber integral (6.26) and obtain the turbulence spectrum:

$$\left|\delta n_{\Omega}(\kappa,-2Kr_a)\right|^2 \propto \frac{\left|\kappa r_a^2\frac{1}{2}\frac{d^2\Phi}{dm^2}(r_{st})\right|_{m=Kr_a}}{L^3(r_{st})}\int_{-\omega/c}^{\omega/c}\left\langle A_s(\omega+\Omega),A_s{}^*(\omega+\Delta\omega+\Omega)\right\rangle\times$$

$$\exp\left(-2i\int_{r_c}^{r_a}\frac{\omega^2}{c^2k_{Kr_a}(r')}dr'\frac{\Delta\omega}{\omega}+2i\kappa'\frac{\omega\alpha_c(r_{st})^3\Delta\omega}{c^2}+\frac{1}{2}\left(\frac{\rho\sin\vartheta}{c}\Delta\omega\right)^2\right)d\left(\frac{2\omega\alpha_c(r_{st})^3\Delta\omega}{c^2}\right); \qquad (6.31)$$

where

$$\kappa'=\frac{\kappa}{|\kappa|}\int_{r_c}^{r_{st}(\kappa)}\frac{dr'}{\alpha_c{}^3(r_{st})k_{Kr_a}(r')}.$$

However, applying this expression in practice seems rather challenging. Nevertheless, within the Born approximation, more general expressions were obtained for the RCDR CCF. One qualitative difference form the slab geometry results seems to be the fact, that instead of the cut-off separation, a quantity δr actually characterizes the spatial separation in the CCF.

The main implication for the experimental measurements of the CCF is the expression for δr. To investigate its impact on the FT-2 RCDR system, a dedicated FT-2 experiment was performed with parameters roughly equivalent to those presented in chapter 5, except for the magnetic field being 2.2 T. Unfortunately, this experiment was performed during experimental phase when due to the technical issues the quality of vacuum in the vessel was degraded. Nevertheless, the obtained RCDR measurements seem to be close enough to typical experimental results to provide information on curvature effect.

The probing was performed with the O-mode polarization at 30 GHz, using the vertical antenna, marked as 110° on the figure 5.1. The CCF measured within the experiment with δr calculated according to cylindrical formula if presented at the figure 6.2:

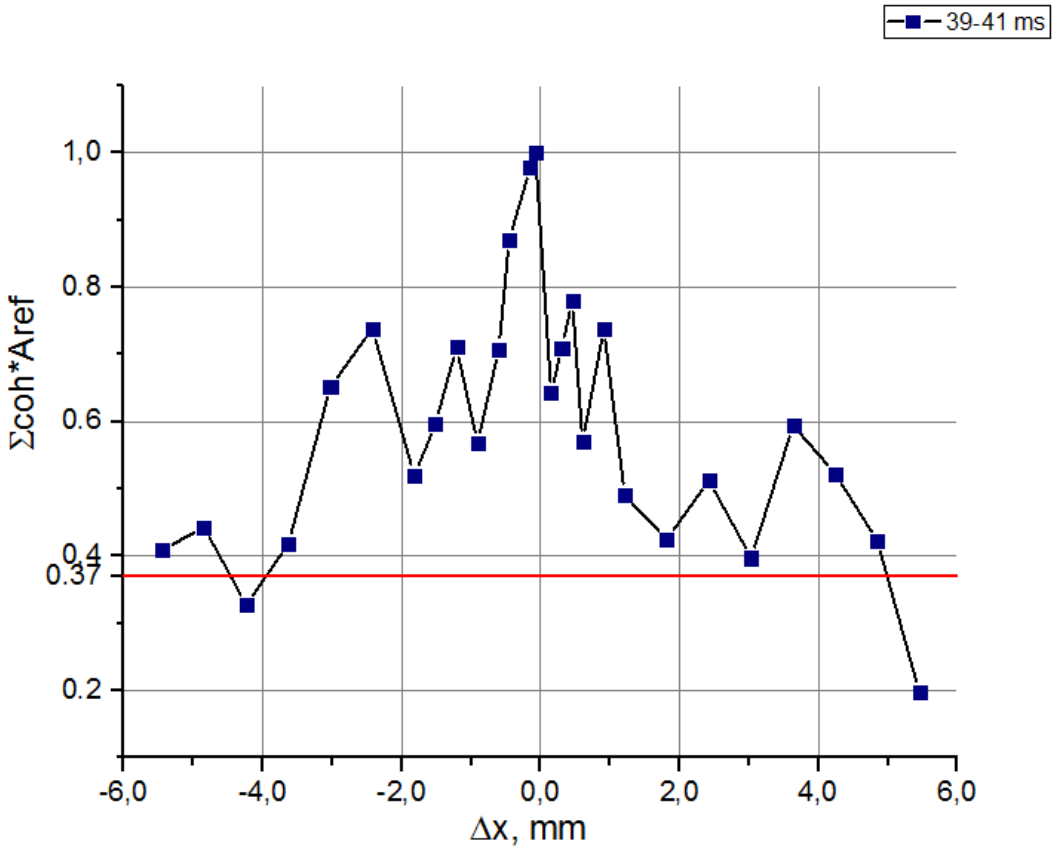

Fig. 6.2. Experimental CCF for cylindrical geometry experiment.

From the figure the value of the radial correlation length can be estimated as 4-5 mm in agreement with other experimental measurements. At the same time, the slab geometry approach of treating cut-off separation as dx for this case would give the value of the radial correlation length higher by 0.5 mm. This difference seems insignificant enough to justify the use of the slab geometry model results for FT-2 experiment analysis.

Overall, new analytical results were obtained describing the effects of plasma curvature on the RCDR diagnostics and underlining the qualitative difference in comparison with the slab geometry model that needs to be taken into account when interpreting the measurements' results.

7. RCDR analysis for tilted turbulent structures

The recently developed technique for the turbulent structures tilt angle measurements, outlined in the section 3.4 was suggested based on the two-point CCF of the turbulence.

The idea behind the diagnostic is that if the turbulent structures are tilted (and anisotropic for the tilt to matter) and moving with poloidal velocity, then the maximum of the turbulence two-point CCF corresponds to nonzero time delay. The reason for such behavior is that, for a given radial separation, the maximum of the correlation can correspond to a nonzero poloidal separation and consequently nonzero delay in time (given by $\Delta y/v_{pol,}$ with Δy being the optimal poloidal separation and v_{pol} being poloidal rotation velocity of plasma, assuming a constant velocity v_{pol}).

The approach suggested and implemented in [49][50] is based on such an interpretation. The dependence of the poloidal separation Δy corresponding to the maximum of CCF for each value of turning point separation Δx (given by $2L(\Delta\omega/\omega)\cos\vartheta^2$ in the notation of chapter 3) is determined and a linear coefficient is extracted. That coefficient is then interpreted according to the formula (3.24) and the turbulence tilt angle is deduced.

The issue with this interpretation is that it is based on the idea that RCDR CCF directly reproduces the turbulence two-point CCF (with two points being the turning points corresponding to the probing frequencies). It was shown within rigorous analysis [22] and was also demonstrated in chapter 3 that even within linear approximation situation could be much more complicated. For that reason, within this thesis a theoretical analysis of this new technique was performed to determine its feasibility.

7.1. Basic equations

The analytical approach of this chapter will mirror the one presented in section 3.3, except for the turbulence spectrum, which now integrates anisotropy, tilt angle, and accounts for poloidal rotation velocity. Once again, slab geometry, linear background density profile and O-mode polarization will once again be employed. An illustration of the geometry of the turbulence as well as the general slab geometry of the model is presented on the figure 7.1.

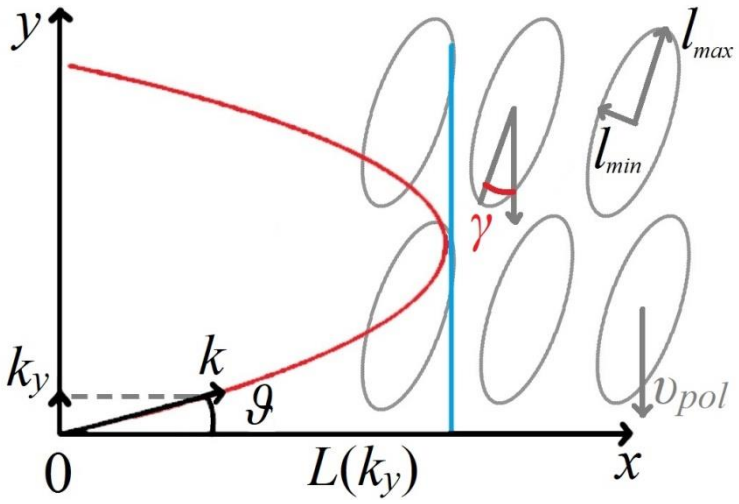

Fig. 7.1. Geometry of the analytical model and illustration of parameters.

The gray ovals of the figure correspond to the turbulent structures, which are assumed to be on average elongated and tilted. The vertical axis corresponds to poloidal direction and consequently v_{pol} corresponds to poloidal rotation velocity of plasma. The red line represents the probing beam, with the blue line being the turning point..

We will start by reiterating the expression for the scattering signal, obtained in 3.3.

$$A_s = \frac{e^2\alpha^2}{m_e c^2}\sqrt{\frac{i\pi}{\alpha}}P\int_{-\infty}^{\infty}\int_{-\infty}^{\infty}\frac{d\kappa dq}{2\pi}\delta n_\Omega(\kappa,q)\frac{\exp\left(i\frac{(\kappa\alpha)^3}{12}-iL\kappa+2i\Phi(\frac{q}{2})+i\kappa q^2\frac{Lc^2}{4\omega^2}-\frac{(q-2K)^2\rho^2}{4}\right)}{\sqrt{\kappa+i\left(\frac{\kappa Lc}{\omega\rho^2}\frac{2-(qc/\omega)^2}{\sqrt{1-(qc/2\omega)^2}}+\frac{Lc^2}{\omega^2\rho^2}\left(q^2-\kappa^2\right)\right)}}. \tag{7.1}$$

To proceed to the normalized correlation function dependent on Δt, we can use the expression, which holds for the statistically stationary turbulence:

$$CCF(\Delta\omega,\Delta t)=\frac{\left\langle\int_{-\infty}^{\infty}A_s(\omega+\Omega)A_s{}^*(\omega+\Omega+\Delta\omega)e^{i\Omega\Delta t}d\Omega\right\rangle}{\left\langle\int_{-\infty}^{\infty}A_s(\omega+\Omega)A_s{}^*(\omega+\Omega)d\Omega\right\rangle\left\langle\int_{-\infty}^{\infty}A_s(\omega+\Omega+\Delta\omega)A_s{}^*(\omega+\Omega+\Delta\omega)d\Omega\right\rangle}, \tag{7.2}$$

where brackets once again designate the averaging over the statistical ensemble of the turbulence, which means they are applied to δn. Like before, density perturbations are assumed to be statistically homogeneous, stationary and independent, and therefore their two-point cross-correlation function can be once more determined from Wiener-Khinchin theorem. After substituting turbulence CCF into (7.2), an expression or CCF takes from.

$$CCF(\Delta\omega,\Delta t)\approx\exp\left[-\left(\frac{\Delta\omega}{\omega}K\rho\right)^2\right]\frac{J(\Delta\omega,\Delta t)}{J(0,0)}; \tag{7.3}$$

$$J(\Delta\omega,\Delta t)=\int_{-\infty}^{\infty}\int_{-\infty}^{\infty}d\kappa dq d\Omega\left|\delta n_\Omega(\kappa,q)^2\right|\exp\left(-\frac{(q-2K)^2\rho^2}{4}+(q-2K)\frac{\Delta\omega}{\omega}K\rho^2\right)\times$$

$$\frac{\exp\left(i2L\kappa\frac{\Delta\omega}{\omega}-2i\Delta\omega\frac{d}{d\omega}\Phi(\frac{q}{2})+i\Omega\Delta t\right)}{\sqrt{\kappa^2+\left(\frac{\kappa Lc}{\omega\rho^2}\frac{2-(qc/\omega)^2}{\sqrt{1-(qc/2\omega)^2}}+\frac{Lc^2}{\omega^2\rho^2}\left(q^2-\kappa^2\right)\right)^2}}.$$

This expression does not yet take into account the specifics of the considered problem, and is very close to the ones obtained in [22][60]. The particularities of the tilted turbulent structure come from the shape of turbulent spectrum and its temporal behavior, which did not play a role in the stationary case considered previously.

To model the tilting angle measurement using RCDR, much like in [49][50] we will consider turbulence with a tilted Gaussian spectrum over wavenumbers rotating uniformly in poloidal direction with velocity v_{pol}:

$$\delta n(\kappa,q)^2=2\pi\delta\left(\Omega-qv_{pol}\right)l_{\min}l_{\max}\delta n_0{}^2\times \tag{7.4}$$

$$\exp(-(\kappa\cos\gamma-q\sin\gamma)^2 l_{\min}{}^2/4-(\kappa\sin\gamma+q\cos\gamma)^2 l_{\max}{}^2/4).$$

Here, γ corresponds to the turbulence tilt angle between the poloidal direction (y-direction) and the stretching direction of the turbulent structure (see Fig.7.1), so γ=0 corresponds to the turbulence being aligned to the poloidal direction. This in turns means that for γ =0 l_{min} and l_{max} are radial and poloidal correlation lengths of the turbulence respectively. This is natural, as turbulent structures are generally elongated along the magnetic field lines.

This spectrum does not include random phases, which are present in the real turbulent structure, but is rather a statistical characteristic of average turbulence in the Wiener-Khinchin theorem (2.2) and is directly related to the turbulence correlation function.

To further simplify the task, we will exploit the paraxial approximation, assuming $|q-2K| << \omega/c$. This assumption will allow us to expand phase Φ into Taylor series over $q-2K$ (a similar procedure was implicitly performed in section 3.3, however around q=0):

$$\Phi = \frac{4}{3}\frac{L\omega}{c}\left(1-\left(\frac{qc}{2\omega}\right)^2\right)^{3/2} \approx \frac{4}{3}\frac{L\omega}{c}\cos^3\vartheta - 2L\cos\vartheta\sin\vartheta\left(q-2K\right) - \frac{Lc\cos 2\vartheta}{2\omega\cos\vartheta}\left(q-2K\right)^2 = \tag{7.5}$$

$$\frac{2}{3}\frac{L\omega}{c\cos\vartheta}\left(2+\sin^2\vartheta+\frac{\sin^2 2\vartheta}{2}\right) - 2L\frac{\sin^3\vartheta}{\cos\vartheta}q - \frac{Lc\cos 2\vartheta}{2\omega\cos\vartheta}q^2;$$

$$\frac{d\Phi}{d\omega}\Delta\omega = 2\frac{L\Delta\omega}{c\cos\vartheta}\left(2+\sin^2\vartheta+\frac{\sin^2 2\vartheta}{2}\right) - 4L\frac{\sin^3\vartheta}{\cos\vartheta}q\frac{\Delta\omega}{\omega} - \frac{Lc\cos 2\vartheta}{2\omega\cos\vartheta}q^2\frac{\Delta\omega}{\omega}.$$

Substituting (7.4) and (7.5) into (7.3), performing the integration over the fluctuation natural frequency Ω and carrying the constant part of Φ out of the integral we obtain:

$$J(\Delta\omega,t) = l_{\min}l_{\max}\,\mathrm{e}^{i\Psi(\Delta\omega)}\int_{-\infty}^{\infty}\int_{-\infty}^{\infty} d\kappa dq \delta n_0{}^2 \frac{\exp\left(i\frac{\Delta\omega}{\omega}\left[2\kappa L + \frac{Lcq^2\cos 2\vartheta}{2\omega\cos\vartheta} + 4Lq\frac{\sin^3\vartheta}{\cos\vartheta}\right] - iq\upsilon_{pol}t\right)}{\sqrt{\kappa^2\rho^4 + \left(\frac{\kappa Lc}{\omega}\frac{2-(qc/\omega)^2}{\sqrt{1-(qc/2\omega)^2}} + \frac{Lc^2}{\omega^2}\left(q^2-\kappa^2\right)\right)^2}} \times \tag{7.6}$$

$$\exp\left(-\frac{l_{\min}^2}{4}\cos^2\varphi(\kappa - q\tan\gamma)^2 - \frac{l_{\max}^2}{4}\sin^2\varphi(\kappa + q\cot\gamma)^2 + \left(q-2K\right)\frac{\Delta\omega}{\omega}K\rho^2 - \frac{\left(q-2K\right)^2\rho^2}{2}\right);$$

where $\Psi = 2\frac{L\Delta\omega}{c\cos\vartheta}\left(2+\sin^2\vartheta+\sin^2 2\vartheta/2\right)$ is the phase that can be excluded by a calibration of the experimental scheme and for that reason it will be omitted as well as the constant numerical coefficients that do not influence the value of the normalized CCF in the subsequent formulae. Integral over poloidal wavenumber q can be once again estimated using the saddle-point method [74]:

$$J(\Delta\omega,t) \propto \int_{-\infty}^{\infty} \frac{\exp\left(i2L\frac{\Delta\omega}{\omega}\kappa - 2\frac{\Delta\omega}{\omega}K^2\rho^2 + \frac{1}{2}\left(\frac{\Delta\omega}{\omega}K\rho\right)^2 - \frac{l_{\min}^2}{4}\kappa^2\cos^2\gamma - \frac{l_{\max}^2}{4}\kappa^2\sin^2\gamma\right)}{\rho^*\left[\kappa^2\rho^4 + \left(\frac{\kappa Lc}{\omega}\frac{2-(q^*c/\omega)^2}{\sqrt{1-(q^*c/2\omega)^2}} + \frac{Lc^2}{\omega^2}\left(q^{*2}-\kappa^2\right)\right)^2\right]^{1/2}} \times \tag{7.7}$$

$$\exp\left(+\frac{1}{2\rho^{*2}}\left[\frac{\kappa\left(l_{\min}^2 - l_{\max}^2\right)\sin 2\gamma}{4} - \left(2+\frac{\Delta\omega}{\omega}\right)K\rho^2 + i\upsilon_{pol}t - 4i\frac{\Delta\omega}{\omega}L\frac{\sin^3\vartheta}{\cos\vartheta}\right]^2\right)d\kappa.$$

Here, q^* and $1/\rho^*$ are defined as follows:

$$q^* = -\left[\frac{\kappa\left(l_{\max}^2 - l_{\min}^2\right)\sin 2\gamma}{4} - \left(2 + \frac{\Delta\omega}{\omega}\right)K\rho^2 + i\upsilon_{pol}t - 4i\frac{\Delta\omega}{\omega}L\frac{\sin^3\vartheta}{\cos\vartheta}\right] / \rho^{*2};$$
$$\rho^* = \sqrt{\rho^2 + l_{\min}{}^2\sin^2\gamma/2 + l_{\max}{}^2\cos^2\gamma/2 - i\frac{\Delta x c\cos 2\vartheta}{2\omega\cos\vartheta}}; \quad (7.8)$$

where q^* corresponds to the saddle point and $1/\rho^*$ is the characteristic width of the region of the main contribution into the integral over poloidal wavenumbers and for realistic parameter values l_{min}, $l_{max} << \rho$ is related to inverse probing beam waist.

For a wide enough beam the expression for the saddle point becomes $q^*=-2K$ which corresponds to the Bragg condition. Here Δx is equal to the separation of cutoffs $2L\Delta\omega/\omega$ and therefore the CCF appears to be a function of cutoff separation rather than of turning points separation given by $2L\cos^2\vartheta\Delta\omega/\omega$. The same result was noted in chapter 3 as well as other RCDR studies [22][58][60].

Next, an integral over radial wavenumber should be determined. The integrand in this case has a saddle point as well as two branching points in the denominator. A similar result was obtained in previous chapter within cylindrical geometry, however, the integration over q in this case is more precise, taking into account the poloidal correlation length of the turbulence spectrum. We will start our consideration with only taking into account the saddle point, which was shown [22] to correspond to a situation when small-angle scattering of long-scale fluctuation is suppressed and the CCF reproduces turbulence correlation function. Other situations will be considered in the later sections.

7.2. CCF at suppressed small-angle scattering

The saddle point κ^* in the integral over κ and the second derivative of the integrand phase in its vicinity are determined by the following expressions:

$$\kappa^* = \frac{i\Delta x + \left(i\upsilon_{pol}t - 2i\Delta x\frac{\sin^3\vartheta}{\cos\vartheta} - \left(2 + \frac{\Delta\omega}{\omega}\right)K\rho^2\right)\left(l_{\max}^2 - l_{\min}^2\right)\sin 2\gamma / 4\rho^{*2}}{\left(l_{\min}^2\cos^2\gamma + l_{\max}^2\sin^2\gamma\right)/2};$$
$$\left.\frac{d^2\Phi}{d\kappa^2}\right|_{\kappa^*} = -l_{\min}^2\cos^2\gamma/2 - l_{\max}^2\sin^2\gamma/2 + \frac{\left(l_{\max}^2 - l_{\min}^2\right)^2\sin^2 2\gamma}{4\rho^{*2}} = -\tilde{l}_{cx}{}^2/2; \quad (7.9)$$

where the value $\tilde{l}_{cx}$ corresponds to the radial localization of the scattering. The first term in it corresponds to the radial correlation length of the turbulence, while the second term corresponds to antenna pattern allowing the scattering of non-central poloidal harmonics of the probing beam and thus affecting localization. The important thing to notice here is that anisotropy of turbulence spectrum introduces real part into the saddle point – due to the tilt of the turbulent structure the nonzero radial wavenumber is prevalent in the spectral component with finite poloidal wavenumber. This effect can play a role for high enough values of probing angle and stronger anisotropy.

The contribution of the saddle point to the integral takes the form:

$$J(\Delta\omega,t)^{saddle} \propto \frac{\exp\left(\frac{1}{2}\left(\frac{\Delta\omega}{\omega}K\rho\right)^2 - 2\frac{\Delta\omega}{\omega}K^2\rho^2 + \frac{1}{2\rho^{*2}}\left[-\left(2+\frac{\Delta\omega}{\omega}\right)K\rho^2 + i\upsilon_{pol}t - 2i\Delta x\frac{\sin^3\vartheta}{\cos\vartheta}\right]^2\right)}{\rho^*\tilde{l}_{cx}\left[\kappa^{*2}\rho^4 + \left(\frac{2\kappa^* Lc}{\omega} + \frac{Lc^2}{\omega^2}q^{*2}\right)^2\right]^{1/2}} \times$$
$$\exp\left(\frac{\left[i\Delta x + \left(i\upsilon_{pol}t - 2i\Delta x\frac{\sin^3\vartheta}{\cos\vartheta} - \left(2+\frac{\Delta\omega}{\omega}\right)K\rho^2\right)\left(l_{\max}^2 - l_{\min}^2\right)\sin 2\gamma / 4\rho^{*2}\right]^2}{\tilde{l}_{cx}^{\,2}}\right). \quad (7.10)$$

Since tilt angle measurement technique is based on determining the t_{max} corresponding to maximum of absolute value of $CCF(\Delta\omega,t)$, it is enough consider terms of exponential that depend on t:

$$J(t)^{saddle} \propto \exp\left(-\frac{(\upsilon_{pol}t)^2}{2\rho^{*2}}\left(1+\frac{\left(l_{\max}^2 - l_{\min}^2\right)^2\sin^2 2\gamma}{8\rho^{*2}\tilde{l}_{cx}^{\,2}}\right) - \frac{\Delta x\upsilon_{pol}t\left(l_{\max}^2 - l_{\min}^2\right)\sin 2\gamma}{2\rho^{*2}\tilde{l}_{cx}^{\,2}}\right) \quad (7.11)$$
$$\exp\left(-i\frac{\upsilon_{pol}t}{\rho^{*2}}\left(1+\frac{\left(l_{\max}^2 - l_{\min}^2\right)^2\sin^2 2\gamma}{8\rho^{*2}\tilde{l}_{cx}^{\,2}}\right)\left[\left(2+\frac{\Delta\omega}{\omega}\right)K\rho^2 + 2i\Delta x\frac{\sin^3\vartheta}{\cos\vartheta}\right]\right);$$

Next, we will consider a situation when l_{min}, l_{max} << ρ which will allow to significantly simplify the resulting formulae. A complete formula for t_{max} without this assumption is derived in Appendix 1. The simplified version of formula takes the following form:

$$J(t)^{saddle} \propto \exp\left(-\frac{\left(\upsilon_{pol}t\right)^2}{2\rho^{*2}} - \frac{\upsilon_{pol}t}{2\rho^{*2}}\frac{\Delta x\left(l_{\max}^2 - l_{\min}^2\right)\sin 2\gamma}{l_{\min}^2\cos^2\gamma + l_{\max}^2\sin^2\gamma} - 2\left(2+\frac{\Delta\omega}{\omega}\right)\frac{iK\rho^2\upsilon_{pol}t}{\rho^{*2}} + \frac{2\Delta x}{\rho^{*2}}\frac{\sin^3\vartheta}{\cos\vartheta}\upsilon_{pol}t\right). \quad (7.12)$$

Substituting expression for ρ^* into it and selecting real component of the exponent's argument after neglecting smaller terms one can write to the following expression:

$$J(t)^{saddle} \propto \exp\left(-\frac{\left(\upsilon_{pol}t\right)^2}{2\rho^2} - \frac{\Delta x\left(l_{\max}^2 - l_{\min}^2\right)\sin 2\gamma}{l_{\min}^2\cos^2\gamma + l_{\max}^2\sin^2\gamma}\frac{\upsilon_{pol}t}{2\rho^2} + \frac{\Delta x}{\rho^2}\frac{\sin\vartheta\cos 2\vartheta}{\cos\vartheta}\upsilon_{pol}t + \frac{2\Delta x}{\rho^2}\frac{\sin^3\vartheta}{\cos\vartheta}\upsilon_{pol}t\right) = \quad (7.13)$$
$$\exp\left(-\frac{\left(\upsilon_{pol}t\right)^2}{2\rho^2} - \frac{\Delta x\left(l_{\max}^2 - l_{\min}^2\right)\sin 2\gamma}{l_{\min}^2\cos^2\gamma + l_{\max}^2\sin^2\gamma}\frac{\upsilon_{pol}t}{2\rho^2} + \frac{\Delta x}{\rho^2}\frac{\sin\vartheta}{\cos\vartheta}\upsilon_{pol}t\right).$$

Using it, the final result for t_{max} as well as the temporal Gaussian width Δ_t of the CCF can be obtained:

$$\upsilon_{pol}t_{\max} = -\frac{1}{2}\frac{\Delta x\left(l_{\max}^2 - l_{\min}^2\right)\sin 2\gamma}{l_{\min}^2\cos^2\gamma + l_{\max}^2\sin^2\gamma} + \Delta x\tan\vartheta; \quad (7.14)$$
$$\upsilon_{pol}\Delta_t = \sqrt{2}\rho.$$

The last term in the first line is a result of combining the last two terms of (7.13). Some remarks should be made about this result. Primary one is that while expression for t_{max} looks similar to the one obtained in the "heuristic" approach [49][50] the definition of Δx there is different, as it is defined as the turning point separation, which in our case takes the form $\Delta x = 2L\cos^2\vartheta\Delta\omega/\omega$. This in turn means that for higher probing angles formula (7.14) gives drastically different values compared to the one introduced in [49][50] due to a difference of a factor $\cos^2\vartheta$. At the same time for low probing angles, poorly localized scattering considered in

the next section and in previous chapters starts playing a role and provides qualitatively different results.

Another thing to note is that from the expression (7.10) radial correlation length of the CCF for the case of tilted turbulence can also be estimated as $l_{cx}^2 = l_{min}^2\cos\gamma^2 + l_{max}^2\sin\gamma^2$, which corresponds to a projection of the tilted turbulence spectrum on the radial coordinate. For the considered case of large ρ* this result could also be readily obtained from the formula ()

7.3. CCF for small-angle scattering dominance

Aside from the saddle point predominance described in the previous section, another situation can be considered. When the saddle point provides exponentially small input into the integral (7.7) compared to the input of branching point vicinity, its contribution can be neglected. We want to estimate the CCF in this case.

To determine branching points, we will simplify denominator in expression (7.7) by substituting $q^*=-2K$ into it. The reason for such treatment is the assumption of correlation lengths being much smaller than ρ coupled with the fact that Δx and t can be estimated as having the same order of magnitude as the radial correlation length l_{cx} and the typical time width Δ_t. In this case, the expression for the branching points in (7.7) takes form, which, under the same assumption of a small probing angle (which is appropriate for the small-angle scattering consideration), naturally coincides with the one obtained in [22]:

$$\kappa_{br}^{\pm} = -2L\sin^2\vartheta\frac{\frac{2Lc}{\omega}\pm i\rho^2}{\left(\frac{2Lc}{\omega}\right)^2+\rho^4}. \tag{7.15}$$

Similarly, a criterion for the critical angle above which the small-angle scattering contribution should be negligible can be obtained. The only difference to the one introduced in [22] is due to the turbulence tilting angle, which causes dominance of nonzero κ in the turbulence spectrum, as mentioned before and also complicates the expression for l_{cx}. The final criterion of small-angle scattering suppression in this case takes a more restricting form:

$$\sin\vartheta^2 >> \sin\vartheta_*^2 = \frac{c}{2\omega}\left(\frac{1}{l_{cx}}+\frac{l_{\max}^2-l_{\min}^2}{l_{cx}^2}\left|\sin 2\gamma\right|\frac{\omega}{c}\sin\vartheta\right)\sqrt{1+\frac{\rho^4\omega^2}{(2Lc)^2}}. \tag{7.16}$$

The case when the branching point provides a dominant contribution into the integral corresponds to the situation when the value of the integrand in κ_{br} is exponentially bigger than the value at κ^* (which corresponds to large value of Δx, when the two points are moved far apart). In this case the main temporal dependence is determined by the value of the integrand at the branching point:

$$J(\Delta\omega,t)\propto Const(\mathrm{t})\exp\left(\frac{1}{2\rho^{*2}}\left[\frac{\kappa_{br}\left(l_{\max}^2-l_{\min}^2\right)\sin 2\gamma}{4}+i\upsilon_{pol}t-\frac{\Delta\omega}{\omega}K\rho^2-4i\frac{\Delta\omega}{\omega}L\frac{\sin^3\vartheta}{\cos\vartheta}\right]^2\right). \tag{7.17}$$

This once again allows determining of the values of t_{max} and Δ_t:

$$\upsilon_{pol} t_{\max} = \frac{L \sin^2 \vartheta}{4\rho^2} \frac{\left(l_{\max}^2 - l_{\min}^2\right) \sin 2\gamma}{\left(\frac{2Lc}{\omega\rho^2}\right)^2 + 1} + \Delta x \tan \vartheta; \tag{7.18}$$

$$\upsilon_{pol} \Delta_t = \sqrt{2}\rho.$$

Same as in the transition from (7.13) to (7.14), the tangent function in (7.18) arises from combining the last two terms of (7.17) when extracting the real part. The value of Δ_t stays the same, since it is determined by integral over q as early as (7.7). The formula (7.18) illustrates that in the case when the scattering signal is dominated by the poorly localized small-angle scattering, the dependence of t_{max} on Δx might not provide information on the turbulence reproducing antenna tilt angle instead. This effect will be observed in numerical calculations in further chapters and it limits the possibility of using t_{max} to obtain information on the turbulence tilt angle.

This result is not so precise due to the fact that we only considered the temporal dependence within the exponential argument. Moreover, it is not possible offer the limits of validity for this result without a much deeper consideration of the integration contour and the saddle point method. But it is important to underline the qualitative possibility of the tmax not being dependent on turbulence parameters (as the first term in (7.18) is often negligible) and moreover, such situation will be demonstrated in calculations in the further sections.

Finally, aside from two considered cases there is an intermediate situation when the CCF is not dominated by small-angle scattering, but it still plays a significant role. In this case the interplay between small-angle scattering and back-scattering needs to be taken into account, since it is impossible to neglect either. Obtaining precise results for such a situation is problematic and its existence further complicates analysis of calculation results.

7.4. Validation with numerical modelling

To validate the results obtained in the previous chapters, numerical modelling was performed using wave propagation solvers. Since results of this chapter were obtained within the Born approximation, linear modelling described in section 4.1 was used. Namely the CCF was numerically computed using expression (3.21), analytical solution E^0 (3.18) and analytical expression for turbulence CCF. While simple, such an approach allowed for recovery of all the relevant physical effects in linear scattering regime.

After calculating the CCF this way, the maximum of its absolute value for each frequency separation $\Delta\omega$ was determined and corresponding t_{max} was obtained. The dependence of t_{max} on Δx was compared with the one described by formula (7.14).

A result of applying such a procedure can be seen on the figure 7.2. On the figure $y_{max} = \upsilon_{pol} t_{max}$ and $\Delta x = 2L\Delta\omega/\omega$. Parameters used for presented calculation were chosen to be relevant to experimental condition and are as follows: L=10 cm, l_{min}=1 cm, l_{max}=1.5 cm, ρ=3 cm, γ=45°, f=30 GHz.

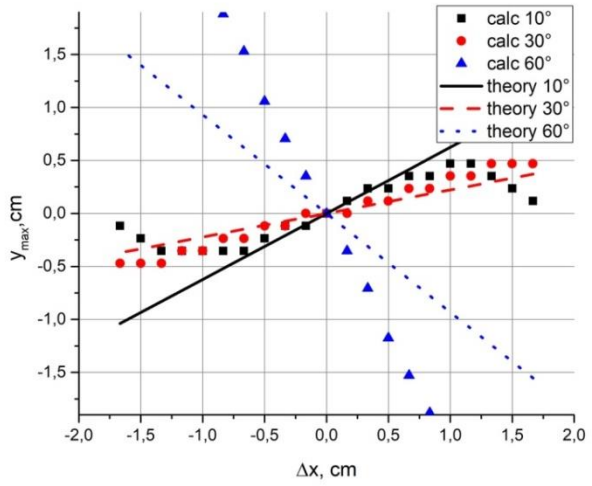

Figure 7.2: CCF maximum dependence on the radial separation. L=10 cm, l_{min}=1 cm, l_{max}=1.5 cm, ρ=3 cm, γ=45°,f=30 GHz. Lines correspond to formula (7.14), symbols correspond to numerical evaluations, while different colors, line and symbol types designate different probing angles ϑ.

It can be seen that for higher probing angle 30° the agreement between theory and calculation is rather good (although not for the angle 60°, which was attributed to edge effects rendering scattering efficiency used in section 3.3 inapplicable, as described in [56]), whereas for the low angle 10° the agreement deteriorates due to small angle scattering. This is in agreement with the theoretical results, predicting that higher probing angles benefit from suppressed small-angle scattering.

A more favorable situation is shown at figure 7.3. In this case the input parameters are as follows: L=4 cm, l_{min}=0.2 cm, l_{max}=1.4 cm, ρ=1.6 cm, γ=45°, f=70 GHz. As it can be seen from the figure significant disagreement can only be observed for the probing angle 10°. Improvement of the situation for these parameters goes in line with the small-angle scattering suppression criterion (7.16).

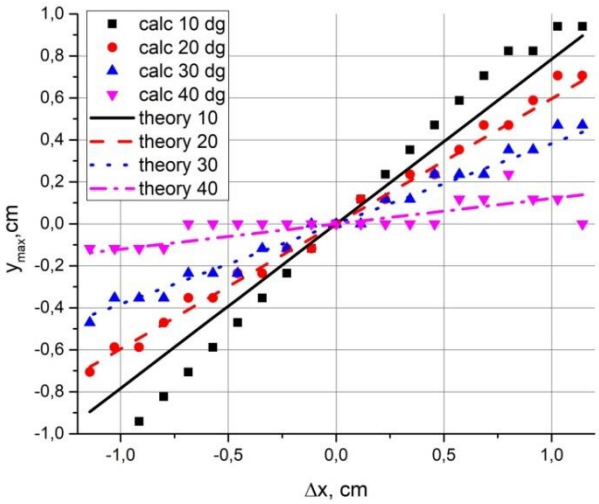

Figure 7.3: CCF maximum dependence on the radial separation. L=4 cm, l_{min}=0.2 cm, l_{max}=1.4 cm, ρ=1.6 cm, γ=45°, f=70 GHz. Lines correspond to formula (7.14), symbols correspond to numerical evaluations, while different colors, line and symbol types designate different probing angles ϑ.

To illustrate the situation when small-angle scattering dominates the scattered signal and dependence on the turbulence parameters becomes negligible, the numerical results for this case are shown on the figure 7.4.

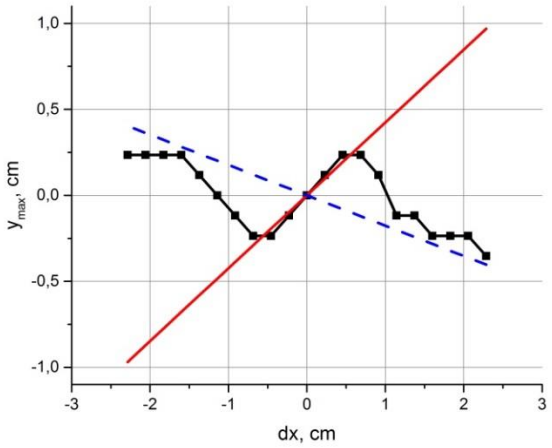

Figure 7.4: CCF maximum dependence on the radial separation for L=8 cm, l_{min}=0.5 cm, l_{max}=1 cm, ρ=2 cm, γ=45°,f=70 GHz. Black line with squares corresponds to computation results, solid red line corresponds to theoretical formula (7.14) while dashed blue line corresponds to formula (7.18)

In agreement with the explanation given in the previous section, for small values of Δx the branching point does not influence integral (7.7) and computation results are adequately described by formula (7.14). As the radial separation grows, the branching and saddle points move further apart and the dependence on the turbulence parameters disappears in agreement with (7.18). The red line seemingly crossing origin corresponds to the fact that constant offset in formula (7.18) for these parameters has the value of 0.01 cm. This corresponds to the fact that small-angle scattering contribution into scattering signal decays much slower with radial separation than that of the backscattering. As it can be seen from the figure 7.4, the influence of small angle scattering can potentially even change the sign of the linear dependence coefficient, which can be used for experimental confirmation of the theoretical predictions.

Finally, to illustrate significance of the difference in Δx definition between this PhD thesis and [50] figure 7.5 demonstrates calculated value of y_{max} together with theoretical predictions given by both (7.14) and "heuristic" interpretation given in [50] as a function of frequency separation. This difference being a factor $\cos^2\vartheta$ is quite significant for larger probing angles, which seem to be more suitable as they allow suppressing small-angle scattering effects. The calculation used is the same at the one presented at figure 7.3, while probing angle is 30°.

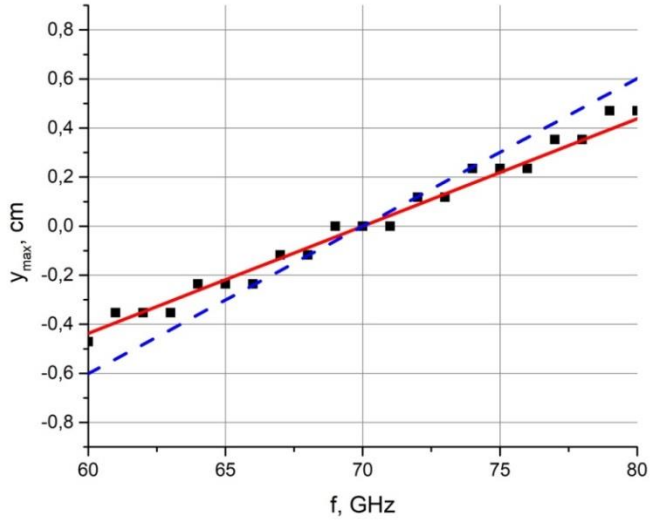

Figure 7.5: Dependence of y_{max} on the probing frequency. L=4 cm, l_{min}=0.2 cm, l_{max}=1.4 cm, ρ=1.6 cm, γ=45°, f=70 GHz. Black symbols correspond to numerical evaluations, solid red and dashed blue lines are given by formula (7.14) and "heuristic" interpretation given in [50] respectively.

To see the impact of difference between analytical formulae we have calculated the turbulence tilt angle from calculation results according to formula (7.14) and to [50] neglecting l_{min} in both cases. The results obtained were 45° and 41° respectively, which means that while rigorous analytical formula provides a better estimate, the difference in the considered case is not that large.

7.5. Discussion

Overall, the numerical modelling results confirm analytical conclusions and highlight the importance of the effects caused by small angle scattering. There is however a number of effects excluded from the model that could complicate things further.

First and foremost, the results of this chapter are derived in Born approximation, which means they are not applicable for nonlinear regime of scattering, which corresponds to higher values of density perturbation amplitude.

Another assumption made is the linear dependence of the density profile on the radial coordinate, which allowed performing explicit integration both in the scattered field and in the phase expressions. In experimental situation, density profile is often nonlinear and moreover, X-mode probing is often used, with k^2 having dependence on both density and magnetic field resulting in a nonlinear radial profile. However, the most efficient scattering takes place in the vicinity of the cut-off, and k^2 can be approximated by a linear dependence. In such a case, the corresponding scale length should replace L in the theoretical results presented here (for X-mode the expression for it is more complicated, but can be inferred from [19][20]).

Such a method could for example be relevant for the H-mode plasma where pressure gradient in the edge area is much steeper than in the core plasma. Due to the main contribution coming from the vicinity of the cut-off deeper areas of the plasma pedestal are well described by such a substitution of a local gradient scale length.

The turbulence profile was also simplified. Firstly, the Gaussian turbulence power spectrum was done both in this thesis and in [49][50]. While experimental spectra follow a power law rather than a Gaussian, it was shown in the [76] that the use of power law spectrum provides the same qualitative result in regards to the influence of small-angle scattering, which decays logarithmically slow, as a function of Δx. Thus, the results of this work are relevant for the experimental situation. The quantitative effect of using turbulence spectrum close to experimental is, however, an interesting topic for future numerical studies. Secondly, the model does not take into account the turbulence temporal decorrelation, which takes place in plasma. The influence of such decorrelation processes, however, can be obtained (as it was done in [50]) by introducing it into turbulence CCF as a factor $\exp(-t^2/t_c^2)$, where t_c is the correlation time. This factor would then be added to formula (7.7) and ultimately result in formulae (7.14) and (7.18) being modified by a factor:

$$\upsilon_{pol} t_{\max}{}^{corrected} = \frac{\upsilon_{pol} t_{\max}}{1+\frac{\rho^2}{\upsilon_{pol}{}^2 t_c^2}}; \qquad \upsilon_{pol} \Delta_t{}^{corrected} = \sqrt{\frac{2\rho^2}{1+\frac{\rho^2}{\upsilon_{pol}{}^2 t_c^2}}}. \tag{7.19}$$

This correction is in agreement with the one described in [50]. Finally, the statistical parameters of the turbulence were assumed to be constant in time and space. Former is acceptable for the measurements in stationary phases of discharge and should not be a problem, as well as a slow temporal variation of the turbulence spectrum asymmetry, while latter is justified by the same logic as the linear background profile. Indeed, in the case when the technique is applicable the main contribution into the scattered signal comes from the vicinity of the turning point and the local parameters can be used in the formulae.

The simplification of the beam waist being much larger than turbulence correlation lengths used to obtain results (7.14) and (7.18) generally holds true in RCDR experiments. Similarly, paraxial approximation used in the section 7.1 is usually applicable.

One more simplification was implicitly made by using the specific form for scattering efficiency in the section 3.3. As mentioned there, in some cases, for example the one presented at figure 7.2, a different scattering efficiency should be used.

Another simplification, which was not explicitly stated before is the infinite limits on the integral in (7.7). The actual limits correspond to κ having to be smaller than $2\omega/c$ for the possibility of scattering to happen following the Bragg rule. Mathematically, this corresponds to the condition of existence of stationary point in the integral over radial coordinate, when calculating A_s (see, for example [56]). While this limitation is not relevant for isotropic turbulence, in the anisotropic case, according to formula (7.7), the saddle point can move out close to this limit and make it meaningful.

Aside from the aforementioned differences with the results obtained in [50] and limitation caused by small angle-scattering effects, a few other conclusions can be drawn. The main one is that, considering equation (7.7), one can see that aside from negligible addition to ρ^*, parameters of turbulent spectrum only participate in the formula in two combinations – the first being $l_{min}^2\cos\gamma^2 + l_{max}^2\sin\gamma^2$ corresponding to l_{cx} and the second being $(l_{max}^2 - l_{min}^2)\sin 2\gamma$. These are exactly the combinations that can be determined from t_{max} dependence on Δx and from the CCF decay with Δx at $t_{max} = 0$. Thus, formula (7.7) shows that it is not possible to resolve individual parameters l_{max}, l_{min}, γ and obtain more information on turbulence tilt from CCF, even if a different technique is used.

Another method however, seems to be applicable – formula (7.10) indicates that dependence of imaginary part of CCF on Δx also provides information on parameter $(l_{max}^2 - l_{min}^2)\sin 2\gamma$, which can be extracted. Advantage of this method is that it does not require temporal analysis of CCF. This method is also possibly more suitable for the reconstruction procedure proposed in [22] and validated in [60] to counteract the influence of small-angle scattering, as the t_{max} approach did not work well with reconstruction procedure in preliminary calculations due to strong influence on numerical errors. Verification of this speculation as well as more detailed study of this alternative method could be the subject of future work.

In the special case when ρ is comparable with the turbulence correlation lengths, additional combination of parameters is present in ρ^* and one could theoretically obtain parameters l_{max}, l_{min}, γ by fitting them into (A1.2) and on the dependence of CCF on Δx given by (7.10). This approach, however, was not further explored within the thesis due to improbability of this situation.

8. Nonlinear regime transition study

As described in the chapter 3, while linear and strongly nonlinear scattering regimes were extensively studied within rigorous analytical theory [19]-[22][56][73], the intermediate regime, which in fact defines the limit of the applicability of the linear theory was only studied within physical optics model [64]. The model considers perturbation of the plasma cut-off, substituting plasma with a corrugated mirror [65][77]. While convenient, this model is not rigorous and neglects plasma volume effects. For that reason, a study devoted to this intermediate nonlinear regime using the rigorous analytical theory was performed and is presented in this chapter.

Similarly to [64], the DR diagnostic will be the object of the analysis, because generalizing the results to the case of RCDR is a rather challenging task. The general approach will also be similar. Since the linear regime is in essence limited by applicability of the perturbation theory, the way to determine this limit is to consider the next step of the perturbation theory and determine the threshold turbulence amplitude for which the next order signal is no longer much smaller than the linear contribution.

8.1. Basic equations

Once again, we will employ the slab geometry, linear background density profile and O-mode polarization to solve the Helmholtz equation. The geometry of the model repeats that of the chapter 3 and is illustrated on the figure 8.1.

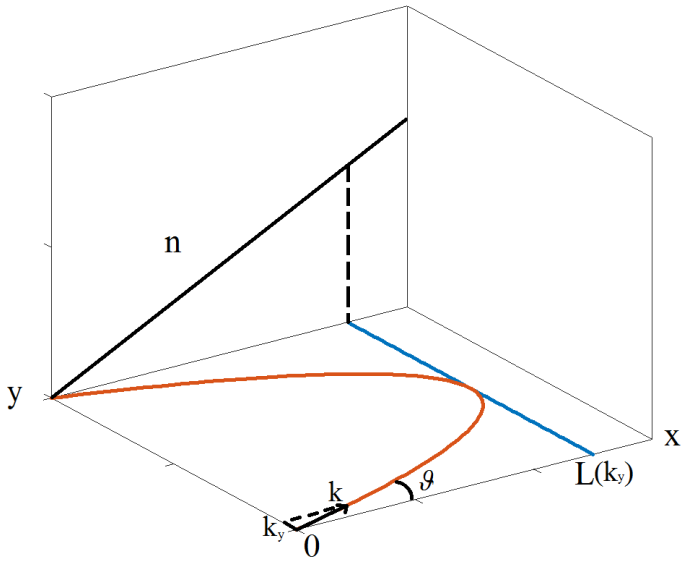

Figure 8.1. The scheme of geometry used in model. Background density profile is linear along x direction.

Unlike section 3.3, we will, however, employ the WKB approximation to obtain the solutions of Helmholtz equation. The same results could be obtained with precise solution (given by Airy function), but our approach allows for a much clearer form of the derivation while retaining all the relevant results.

The solution of the unperturbed equation (3.14) s given by the expression:

$$E_z^{\,0}(x,k_y) = f(k_y)\sqrt{\frac{k(0,k_y)}{k(x,k_y)}}\,\mathrm{e}^{\,i\Phi(k_y)+i\frac{\pi}{4}}\cos\left(\int_x^{L(k_y)} k(x,k_y)dx+\frac{\pi}{4}\right).. \qquad (8.1)$$

Here, once again $\Phi(k_y)=\int_0^{L(k_y)} k(x,k_y)\,dx$, $f(k_y)$ is the probing beam amplitude distribution over poloidal wavenumbers. $L(k_y)$ is radial turning point position for a given poloidal wave number and $k(x,k_y)^2=k^2(x)-k_y^2$. Since we are looking for the next order solution, we cannot just plug formula (8.1) into reciprocity theorem and will have to solve the perturbed Helmholtz equation. Using the solution (8.1) and performing Fourier transform along y, equation (3.15) can be rewritten as:

$$\frac{d^2}{dx^2}\frac{c^2}{\omega^2}E_z^{\,1}(x,k_y)+\frac{c^2}{\omega^2}k(x,k_y)^2E^1(x,k_y)=$$
$$\sqrt{\frac{k(0,k_y)}{k(x,k_y)}}\int_{-\infty}^{\infty}\frac{\delta n(x,q)}{n_c}\exp\left(i\Phi(k_y-q)+i\frac{\pi}{4}\right)\cos\left(\int_x^{L(k_y-q)}k(x',k_y-q)dx'+\frac{\pi}{4}\right)f(k_y-q)dq. \tag{8.2}$$

The convolution in the right-hand part is performed over the poloidal wavenumber of the density fluctuation q. To find the solution of this equation a major simplification that will be employed – the density fluctuations will be assumed to be uniform over radial (x) direction (this corresponds to the radial correlation length of a turbulence having large value $l_{cx}\sim L$). Such simplification is a strong one, but is goes in line with the physical optics model, which has already provided relevant results. Moreover, the obtained result will also be generalized to the case of arbitrary radial correlation length of the turbulence.

Relying on such simplification, and determining boundary conditions from the perturbation theory, the solution of the next order can be obtained:

$$E_z^{\,1}(x,k_y)=\sum_{t=\pm1}\frac{\frac{\omega^2}{c^2}\frac{\delta n(q)}{n_c}f(k_y-q)e^{i(t+1)\frac{\pi}{4}}}{k(x,k_y)^2-k(x,k_y-q)^2}\sqrt{\frac{k(0,k_y-q)}{k(x,k_y-q)}}\exp\left(i\Phi(k_y-q)+it\left(\int_x^{L(k_y-q)}k(x',k_y-q)dx'\right)\right)-$$
$$\sum_{s=\pm1}\sum_{t=\pm1}\frac{1}{2}\left(1-t\frac{k(0,k_y-q)}{k(0,k_y)}\right)\frac{\frac{\omega^2}{c^2}\frac{\delta n(q)}{n_c}f(k_y-q)e^{i(s+1)\frac{\pi}{4}}}{k(0,k_y)^2-k(0,k_y-q)^2}\sqrt{\frac{k(0,k_y)}{k(x,k_y)}}\exp\left(i\Phi(k_y)+(t+1)\Phi(k_y)+is\left(\int_x^{L(k_y)}k(x',k_y)dx'\right)\right). \tag{8.3}$$

This solution includes two terms, one of them represents a solution of the differential equation (8.2) when it is homogeneous, whereas the other does not. They can be interpreted as the "propagating" term and the "forced" term and for that reason we will introduce the designation A^F and A^P:

$$A^F=\sum_{p=\pm1}\sqrt{\frac{k(0,K)}{k(x,K)}}\exp\left(i\Phi(K)+ip\left(\int_x^{L(K)}k(x',K)dx'+\frac{\pi}{4}\right)\right);$$
$$A^P=\sum_{p=\pm1}\sum_{t=\pm1}\frac{1}{2}\left(1-\frac{tk(0,K)}{k(0,K+q)}\right)\sqrt{\frac{k(0,K+q)}{k(x,K+q)}}\times \tag{8.4}$$
$$\exp\left(ip\frac{\pi}{4}+i\Phi(K+q)+i(t+1)\Phi(K)+ip\int_x^{L(K+q)}k(x',K+q)dx'\right)\Bigg].$$

Once again, we will employ the reciprocity theorem [55] to determine both linear and quadratic scattering signals. The formula (3.18) is this case can be rewritten in the following form:

$$A_s^{linear} = \frac{ie^2}{4m_e\omega^2}\omega\sqrt{P}\int_{-\infty}^{\infty}\int_{-\infty}^{\infty}\frac{\delta n(y)}{n_c}E_z{}^0(x,y)^2\,dxdy \propto \delta n;$$
$$A_s^{quadratic} = \frac{ie^2}{4m_e\omega^2}\omega\sqrt{P}\int_{-\infty}^{\infty}\int_{-\infty}^{\infty}\frac{\delta n(y)}{n_c}E_z{}^0(x,y)E_z{}^1(x,y)dxdy \propto \delta n^2. \quad (8.5)$$

Linear response is then given by a formula:

$$A_s = -\frac{e^2\sqrt{P}}{4m_e\omega}\int_{-\infty}^{\infty}dq\int_{-\infty}^{\infty}dk_y\int_0^{\min(L(k_y),L(k_y+q))}dx\sum_{s,t=\pm1}\frac{\delta n(q)}{n_c}\mathrm{e}^{i(s+t)\frac{\pi}{4}}\sqrt{\frac{k(0,k_y)k(0,k_y+q)}{k(x,k_y)k(x,k_y+q)}}\times$$
$$f(-k_y-q)\,f(k_y)\exp\left(i\Phi(k_y+q)+i\Phi(k_y)+it\int_x^{L(k_y)}k(x',k_y)dx'+is\int_x^{L(k_y+q)}k(x',k_y+q)dx'\right). \quad (8.6)$$

Now, like usual, we will assume antenna to have a Gaussian poloidal wavenumber spectrum $f\left(k_y\right)=\left(2\sqrt{\pi}\rho\right)^{1/2}\exp\left[-\left(k_y-K\right)^2\rho^2/2\right]$, where once again $K=\omega\sin\vartheta/c$, ϑ is a probing angle with respect to normal to magnetic surface (which in our case is directed along x) and $\sqrt{2}\rho$ is probing beam waist. The integrals over q and k_y in (8.5) can be calculated using saddle-point method, however to simplify further derivation we will assume wide enough beam corresponding to the cutoff situated in the antenna near field.

$$\rho^2 >> \int_0^{L(K)}\frac{dx}{k\left(x,K\right)}. \quad (8.7)$$

In this case antenna pattern determines the main contribution to integrals over poloidal wave numbers in (8.5) and the result of the integration is:

$$A_s = \frac{ie^2}{4m_e\omega^2}\frac{4\pi^{3/2}}{\rho}\omega\sqrt{P}\int_0^{L(K)}dx\sum_{t=\pm1}\sum_{s=\pm1}\frac{\delta n(-2K)}{n_c}\frac{k(0,k_y)}{k(x,K)}\times$$
$$\exp\left(2i\Phi(K)+i\frac{\pi}{2}+i(s+t)\left[\int_x^{L(k_y)}k(x,K)dx+\frac{\pi}{4}\right]\right). \quad (8.8)$$

In this formula two contributions having a different origin can be seen. Contributions possessing same indexes $s=t$, which correspond to backscattering in radial direction and contributions possessing $s=-t$ which correspond to the forward-scattering. The same result was seen in more detail in a cylindrical description presented in chapter 6. The difference here is that our turbulence has the radial wave number equal to zero and therefore the forward-scattering will dominate the scattering signal. This is seen mathematically by the fact that in the case of $s=t$ the fast oscillation of phase will reduce the value of the integral (making it negligible for large radial correlation length $l_{cx}>>(Lc^2/\omega^2)^{1/3}$).

Up to this point, we didn't make any assumptions about density profile shape. To calculate integral over x we will assume that density profile is linear, which means that $k(x)$ can be written as $k(x,k_y)=\frac{\omega}{c}\sqrt{\frac{L(k_y)-\mathrm{x}}{L(0)}}$ which allows us to calculate the scattering signal. Neglecting the back-scattering component, we obtain:

$$A_s^{lin} = -4\frac{\pi^{3/2}e^2\sqrt{P}}{m_e\omega\rho}\frac{\delta n(-2K)}{n_c}L(K)\exp\left(i\frac{4}{3}\frac{\omega L(K)^{3/2}}{cL(0)^{1/2}}\right). \tag{8.9}$$

8.2. Quadratic scattering signal

Next, to determine the quadratic scattering signal we will substitute (8.1) and (8.3) into the second expression in (8.5). Utilizing the same wide beam approximation (8.7), we can obtain:

$$A_s = \frac{e^2}{4m_e\omega}\frac{4\pi^{3/2}}{\rho}\sqrt{P}\frac{\omega^2}{c^2}\int_{-\infty}^{\infty}dq\int_0^{L_{\min}}dx\sum_{s=\pm1}\frac{\delta n(q)}{n_c}\frac{\delta n(-q-2K)}{n_c}\times$$
$$\exp\left(i\Phi(K)+is\int_x^{L(K)}k(x,K)dx+is\frac{\pi}{4}\right)\sqrt{\frac{k(0,K)}{k(x,K)}}\frac{\left(A^F-A^N\right)}{q(q+2K)}; \tag{8.10}$$

where L_{min} is the smallest value between $L(q)$ and $L(q+K)$.

Firstly, we will consider A^F together with the t=-1 term of A^P since they can cancel each other out for specific values of q. Integrals over x can be written as:

$$I_F = \sum_{s,p=\pm1}\int_0^{L(K)}\frac{k(0,K)}{k(x,K)}\exp\left(i\Phi(K)+i(s+p)\left[\int_x^{L(K)}k(x',K)dx'+\frac{\pi}{4}\right]\right)dx \approx$$
$$4L(K)\exp\left(i\frac{2}{3}\frac{\omega L(K)^{3/2}}{cL(0)^{1/2}}\right); \tag{8.11}$$
$$I_P = \sum_{s,p=\pm1}\int_0^{L_{\min}}\sqrt{\frac{k(0,K)}{k(x,K)}\frac{k(0,K+q)}{k(x,K+q)}}\exp\left(i\Phi(K+q)\right)\times$$
$$\exp\left(is\left[\int_x^{L(K)}k(x',K)dx'+\frac{\pi}{4}\right]+ip\left[\int_x^{L(K+q)}k(x',K+q)dx'+\frac{\pi}{4}\right]\right)dx.$$

The main contribution to the signal is once again provided by forward-scattering (s=p) due to faster variation of the phase in the backscattering term integrand. Due to the faster integrand phase variation, I_P is negligible compared to I_F for most values of q. The exception is q=0 and q=-2K when the two integrals coincide. For that case, we will expand the phase of integrand of I_P into Taylor series over q and calculate the integral. Since the integrand in (8.10) is symmetrical around q = -K, the results will also apply to vicinity of q=-2K.

The area where I_P is not negligible is defined as $|q| << \Delta q = \frac{1}{\sqrt{L(0)L(K)}sin\vartheta}$, which corresponds to slow variations of the integrand phase over integration domain. In such a case after performing the integration over x we obtain the following:

$$I_P^{FS} = 4L(K)\exp\left(i\frac{2}{3}\frac{\omega L(K)^{3/2}}{cL(0)^{1/2}}-2i\sqrt{L(0)L(K)}\frac{c}{\omega}Kq\right)\times$$
$$\frac{\sin\left(2\sqrt{L(0)L(K)}\frac{c}{\omega}Kq\right)}{2\sqrt{L(0)L(K)}\frac{c}{\omega}Kq}. \tag{8.12}$$

This approach, however, is only valid, when the special points in (8.10) can be considered separately, which corresponds to $K > \Delta q$. Also, similar result can be obtained for t=1 term in A^P. It is, however, smaller than a combination of terms in (8.12) and can be neglected.

Substituting (8.12) into (8.10) and neglecting A^P, where it is appropriate, we get:

$$A_s = 8\frac{e^2}{m_e c^2}\frac{\pi^{3/2}}{\rho}\omega\sqrt{P} = L(K)\exp\left(i\frac{4}{3}\frac{\omega L(K)^{3/2}}{cL(0)^{1/2}}\right)\times$$
$$\left[\int_{-K}^{-\Delta q}\frac{\delta n(q)\delta n(-q-2K)}{q(q+2K)n_c^{\,2}}dq + \int_{\Delta q}^{\infty}\frac{\delta n(q)\delta n(-q-2K)}{q(q+2K)n_c^{\,2}}dq + \right. \tag{8.13}$$
$$\left. i\sqrt{L(0)L(K)}\frac{c}{\omega}\int_{-\Delta q}^{\Delta q}\frac{\delta n(q)\delta n(-q-2K)}{n_c^{\,2}}dq\right].$$

To continue the analysis, we will assume the Gaussian spectrum of the density fluctuations $\delta n(q) = \delta n_0 l_{cy}\exp\left[-q^2 l_{cy}^2/8\right]$. In this case, estimating the main contribution to A_s one can obtain:

$$\begin{cases} A_s \propto \dfrac{e^2\sqrt{P}}{m_e\omega\rho}\dfrac{\omega^2}{c^2}\dfrac{L(K)l_{cy}}{K^2}\dfrac{\delta n_0^{\,2}}{n_c}\times & \\ \exp\left(i\dfrac{4}{3}\dfrac{\omega L(K)^{3/2}}{cL(0)^{1/2}} - \dfrac{l_{cy}^2K^2}{4}\right); & Kl_{cy} >> 1; \\ A_s \propto \dfrac{e^2\sqrt{P}}{m_e\omega\rho}\dfrac{\omega^2}{c^2}\dfrac{L(K)l_{cy}^2}{K}\dfrac{\delta n_0^2}{n_c^{\,2}}\times & \\ \exp\left(i\dfrac{4}{3}\dfrac{\omega L(K)^{3/2}}{cL(0)^{1/2}}\right); & Kl_{cy} < 1. \end{cases} \tag{8.14}$$

In the intermediate case Kl_{cy}~1 an integral evaluation is difficult, but these two parametric dependencies coincide with each other in this case which points to the conclusion that parametric dependencies properly describe the whole range of parameters. Here and in the following we neglect the numerical factors and only show parameter dependencies due to the fact that some of the estimates performed are somewhat imprecise and therefore numerical factors cannot always be trusted. This, of course, adds a degree of uncertainty to the use of the obtained results. To overcome it we employ full-wave numerical modelling which reveals that, for experimentally relevant results, omitted coefficients only come into play under extreme conditions.

For the opposite case of $K<\Delta q$, we can also expand the phase of (8.11) into Taylor series in the vicinity of q=0. In this case the area of validity of such expansion is $q << \Delta q_2 = \sqrt{\omega/cL(0)\cos\vartheta}$. After performing integration over x under the same assumptions as before we get:

$$I_F^{\,FS} = 4L(K)\exp\left(i\frac{2}{3}\frac{\omega L(K)^{3/2}}{cL(0)^{1/2}}\right);$$
$$I_P^{\,FS} \approx 4L(K)\exp\left(i\frac{2}{3}\frac{\omega L(K)^{3/2}}{cL(0)^{1/2}} - i\sqrt{L(K)L(0)}\frac{c}{\omega}q(q+K)\right)\times \tag{8.15}$$
$$\frac{\sin\left(\sqrt{L(K)L(0)}\dfrac{c}{\omega}q(q+K)\right)}{\sqrt{L(K)L(0)}\dfrac{c}{\omega}q(q+K)}.$$

Once again, taking the contribution of A^P into account only in vicinity of q=0, we can split A_s into two integrals over different domains:

$$A_s = 8\frac{e^2}{m_e c^2}\frac{\pi^{3/2}}{\rho}\omega\sqrt{P}L(K)\exp\left(i\frac{4}{3}\frac{\omega L(K)^{3/2}}{cL(0)^{1/2}}\right)\times$$
$$\left[\int_{\Delta q_2}^{\infty}\frac{\delta n(q)\delta n(-q-2K)}{q(q+2K)n_c^{\,2}}dq + \right. \tag{8.16}$$
$$\left. i\sqrt{L(K)L(0)}\frac{c}{\omega}\int_{-K}^{\Delta q_2}\frac{q+K}{q+2K}\frac{\delta n(q)\delta n(-q-2K)}{n_c^{\,2}}dq\right].$$

Estimating the main contribution into the integral over q for different ranges of l_{cy} we obtain

$$\begin{cases} A_s \propto \dfrac{e^2\sqrt{P}}{m_e\omega\rho}\dfrac{\delta n_0^{\,2}}{n_c^{\,2}}l_{cy}\sqrt{L(K)^3L(0)}\times \\ \dfrac{\omega}{c}\exp\left(i\dfrac{4}{3}\dfrac{\omega L(K)^{3/2}}{cL(0)^{1/2}}-K^2l_{cy}^2/4\right); \end{cases} \quad \Delta q l_{cy} >> 1; \tag{8.17}$$
$$\begin{cases} A_s \propto \dfrac{e^2\sqrt{P}}{m_e\omega\rho}\dfrac{\delta n_0^{\,2}}{n_c^{\,2}}l_{cy}^2L(K)\dfrac{\omega^2}{c^2}\times \\ \sqrt{\dfrac{\sqrt{L(K)L(0)}c}{\omega}}\exp\left(i\dfrac{4}{3}\dfrac{\omega L(K)^{3/2}}{cL(0)^{1/2}}\right); \end{cases} \quad \Delta q l_{cy} << 1.$$

These parametric dependencies also coincide in the intermediate parameter range at $\Delta q l_{cy}$~1. Moreover at K~Δq formulae (8.17) and (8.14) are in agreement with each other.

8.3. Nonlinear transition criterion

We have obtained both linear and quadratic contributions to the scattering signal, which correspond to single and double scattering of the probing wave. Comparing both contributions allows us to derive the threshold amplitude for δn above which nonlinear effects significantly influence the scattering signal. Combining (8.9), (8.14) and (8.17) we obtain the final criterion set:

$$\begin{cases} \begin{cases} \dfrac{\delta n}{n_c} >> \dfrac{c}{\omega L\cos\vartheta}\mathrm{e}^{-K^2l_{cy}^2/4}; & \Delta q_2 l_{cy} >> 1 \quad (a) \\ \dfrac{\delta n}{n_c} >> \dfrac{c}{\omega l_{cy}}\sqrt{\dfrac{c}{\omega L\cos\vartheta}}; & \Delta q_2 l_{cy} << 1 \quad (b) \end{cases} & \Delta q >> K; \\ \begin{cases} \dfrac{\delta n}{n_c} >> \dfrac{\sin^2\vartheta}{\sqrt{\pi}}\mathrm{e}^{-K^2l_{cy}^2/4}; & K >> 1/l_{cy} \quad (c) \\ \dfrac{\delta n}{n_c} >> \dfrac{c\sin\vartheta}{\omega l_{cy}}; & K << 1/l_{cy} \quad (d) \end{cases} & \Delta q << K. \end{cases} \tag{8.18}$$

While this system is consistent in itself, the interpretation of different parameter ranges using it is difficult. This system of inequalities can be rewritten with respect to the values of L, l_{cy}, c/ω and ϑ. After these changes, we obtain two cases corresponding to different value of poloidal correlation length of turbulence.

For $l_{cy}^{\,2} >> Lc/\omega$:

$$\frac{\delta n}{n_c} >> \frac{c}{\omega L\cos\vartheta}\exp\left(\frac{-K^2 l_{cy}^2}{4}\right);\quad \sin\vartheta << \sqrt{\frac{c}{\omega L\cos\vartheta}};\quad (a)$$
$$\frac{\delta n}{n_c} >> \sin^2\vartheta\exp\left(\frac{-K^2 l_{cy}^2}{4}\right);\qquad \sqrt{\frac{c}{\omega L\cos\vartheta}} << \sin\vartheta;\quad (b) \tag{8.19}$$

In the opposite case of $l_{cy}^2 << Lc/\omega$, the criterion set is expressed as:

$$\frac{\delta n}{n_c} >> \frac{c}{\omega l_{cy}}\sqrt{\frac{c}{\omega L\cos\vartheta}};\qquad \sin\vartheta << \sqrt{\frac{c}{\omega L\cos\vartheta}};\quad (a)$$
$$\frac{\delta n}{n_c} >> \frac{c\sin\vartheta}{\omega l_{cy}};\qquad \begin{array}{l}\sqrt{\frac{c}{\omega L\cos\vartheta}} << \sin\vartheta;\\ \sin\vartheta << \frac{c}{\omega l_{cy}};\end{array}\quad (b) \tag{8.20}$$
$$\frac{\delta n}{n_c} >> \sin^2\vartheta\exp\left(\frac{-K^2 l_{cy}^2}{4}\right);\quad \frac{c}{\omega l_{cy}} << \sin\vartheta;\quad (c)$$

The latter case (8.20c) seems to be relevant to the Doppler backscattering experimental measurements, however for these results to be applicable the density perturbation should be smaller than that prescribed by the criteria of the transition to fully nonlinear regime described in section 3.5. This regime is characterized by the strong probing wave phase modulation and by saturation of the scattering signal power growth with the probing microwave power. Using the approach described in [19][20] together assuming a linear density profile and large radial correlation length the condition of strong phase perturbation of the probing beam can be rewritten.

Indeed, the formula describing the probing beam phase perturbation in [19] following our notation and under the assumption of 1D density fluctuations and linear background profile can be written as:

$$\delta\Phi(k_y) = -\frac{\omega^2}{2k_y c^2}\int_0^{y_0}\frac{\delta n(y)}{n_c}dy;$$
$$y_0(k_y) = 4k_y\frac{Lc}{\omega}\cos\vartheta. \tag{8.21}$$

Then, the phase perturbation correlation function becomes:

$$\sigma_{ji} = \left\langle \delta\Phi(k_{yi}), \delta\Phi(k_{yj})\right\rangle = -\frac{\omega^4}{4k_{yi}k_{yj}c^4}\int_0^{y_0(k_{yi})}\int_0^{y_0(k_{yi})}\frac{\left\langle\delta n(y)\delta n(y')\right\rangle}{n_c^{\,2}}dydy'. \tag{8.22}$$

Assuming the turbulence to be statistically stationary and homogeneous, it is reduced to:

$$\sigma_{ii} = -\frac{\omega^4}{k_y^{\,2}c^4}\int_{-\infty}^{\infty}\frac{\left|\delta n(q)\right|^2}{n_c^{\,2}}\sin^2\left(qy_0(k_{yi})/2\right)\frac{dq}{q^2}. \tag{8.23}$$

Now, assuming the turbulence has the Gaussian poloidal wavenumber spectrum and taking into account narrow antenna angular pattern, this integral can be estimated as:

$$\sigma_{ii} = \begin{cases}\left(\frac{L\omega}{c}\cos\vartheta\right)^2\frac{\delta n^2}{n_c^{\,2}};\quad \frac{L}{l_{cy}}\sin\theta\cos\vartheta << 1;\\ \frac{\omega^2 l_{cy}L\cos\vartheta}{c^2\sin\vartheta}\frac{\delta n^2}{n_c^{\,2}};\quad \frac{L}{l_{cy}}\sin\theta\cos\vartheta >> 1.\end{cases} \tag{8.24}$$

Numerical factors are neglected here once again. This expression can finally be used to obtain threshold density values:

$$\frac{\delta n^{saturation}}{n_c} >> \frac{c}{\omega L \cos\vartheta}; \qquad \sin\vartheta << \frac{l_{cy}}{L\cos\vartheta}; \quad (a)$$
$$\frac{\delta n^{saturation}}{n_c} >> \frac{c}{\omega}\sqrt{\frac{\sin\vartheta}{l_{cy} L\cos\vartheta}}; \quad \sin\vartheta >> \frac{l_{cy}}{L\cos\vartheta}. \quad (b) \tag{8.25}$$

Now that we have obtained the criteria for both nonlinear regime and saturated regime, we can see under which conditions it is possible to obtain nonlinear regime without immediately going into a saturated one

Comparing (8.25) to (8.19) and (8.20) we can see that even for a small nonzero probing angle large enough value of l_{cy} can lead to an existence of nonlinear regime that is not saturated. It can also be seen that in case of $l_{cy}<c/\omega$ the strong phase modulation threshold is never higher than the threshold of nonlinear regime we are considering in this work.

The most interesting question however, is: How does the obtained criterion correspond to the one resulting from the physical optics model [64]? To draw comparison between the two models' resutls we first need to change the normalization employed in [64] to take the plasma volume phenomenon into account and based on [19][20]. In the case of 1D turbulence considered in the present study the condition of strong phase modulation utilized for normalisation in [64] takes the form of (8.25) instead of

$$\frac{\delta n}{n_c} >> \frac{c}{\omega\sqrt{l_{cx} L \ln\left(L/l_{cx}\right)}}. \tag{8.26}$$

Thus, the condition of nonlinear regime onset derived in [64] coincides with (8.19a). According to [64], however, this criterion should be valid for the whole parameter range and other criteria are not obtained. The reason for that might be Kirchhoff approximation [77] used in [64]. Under our assumption, the Kirchhoff aproximation imposes the condition $\delta n/n_c<<c/\omega L$, which contradicts most of parameter ranges in (8.19) and (8.20).

Finally, in order to generalise criteria (8.19) and (8.20) to the case of real 2D turbulence we will employ the same normalization approach as described in [64]. Firstly, we will note that in the case of 1D density fluctuations and normal probing of plasma the criterion (8.19a) coincides with the saturation criterion (8.25a). While we are unable to derive nonlinearity criterion that would account for radial inhomogenity of the turbulence and to include radial correlation length, a saturation criterion at normal incidence of the probing wave was obtained in [19][20]. Assuming that both criteria coincide in for normal incidence general case of the 2D turbulence and using the strong phase modulation criterion (8.26) obtained for the 2D turbulence one can obtain from (8.19) the following criteria:

$$\frac{\delta n}{n_c} >> \frac{c\,\mathrm{e}^{\frac{-K^2 l_{cy}^2}{4}}}{\omega\sqrt{l_{cx} L \ln\left(\frac{L}{l_{cx}}\right)}\cos\vartheta}; \qquad \sin\vartheta << \sqrt{\frac{c}{\omega L\cos\vartheta}}; \quad (a)$$

$$\frac{\delta n}{n_c} >> \sin^2\vartheta \sqrt{\frac{L}{l_{cx}\ln\left(\frac{L}{l_{cx}}\right)}}\,\mathrm{e}^{\frac{-K^2 l_{cy}^2}{4}}; \quad \sqrt{\frac{c}{\omega L\cos\vartheta}} << \sin\vartheta. \quad (b) \tag{8.27}$$

Then, taking into account that (8.19) and (8.20) are consistent in the intermediate parameter ranges, new expression for (8.20) can also be obtained:

$$\frac{\delta n}{n_c} >> \frac{c}{\omega l_{cy}}\sqrt{\frac{c}{\omega l_{cx}\ln\left(\frac{L}{l_{cx}}\right)\cos\vartheta}}; \quad \sin\vartheta << \sqrt{\frac{c}{\omega L\cos\vartheta}}; \quad (a)$$

$$\frac{\delta n}{n_c} >> \frac{c\sin\vartheta}{\omega l_{cy}}\sqrt{\frac{L}{l_{cx}\ln\left(\frac{L}{l_{cx}}\right)}}; \quad \begin{array}{l}\sqrt{\frac{c}{\omega L\cos\vartheta}} << \sin\vartheta;\\ \sin\vartheta << \frac{c}{\omega l_{cy}};\end{array} \quad (b) \tag{8.28}$$

$$\frac{\delta n}{n_c} >> \sin^2\vartheta \sqrt{\frac{L}{l_{cx}\ln\left(\frac{L}{l_{cx}}\right)}}\,\mathrm{e}^{\frac{-K^2 l_{cy}^2}{4}}; \quad \frac{c}{\omega l_{cy}} << \sin\vartheta. \quad (c)$$

These formulae are obtained by normalizing (8.19) and (8.20) with a coefficient $\sqrt{\frac{L}{l_x\ln(L/l_x)}}$ coming from [19][20]. The physical meaning behind this normalization is the fact that for finite radial corerlation length the area of where the scattering happens is limited not by the whole volume L but by an area defined by $l_{cx}\ln(L/l_{cx})$as shown in [19].

While this procedure is based on assumption of the concidence of nonlinearity and saturation criteria in the case ϑ=0, direct analytical confirmation of which seems challenging (although it should be possible within 1D consideration and could be a topic of future study), the numerical validation is possible. The results of full-wave modelling presented both in [64] and in latter sections of this chapter are in agreement with the generalized formulae (8.27) and (8.28).

The generalized expression (8.27a) also explicitly coincides with the one obtained in [64]. While the parameters determining transition to nonlinear regime include turbulence correlation length, that is not nesecessarily known in experiments, formulae (8.27) and (8.28) still provide some information about the possibility of obtaining linear scattering regime in experiments.

Overall, it seems that while results of the rigorous analysis reproduce those of physical optics model, they also add additional expressions for different parameter ranges.

8.4. Analytical results discussion

After establishing criteria for the transition to nonlinear regime, we would like to consider their relevance to experiment. But before doing that all the limitations of the model should be accounted for. Such limitations as the use of slab geometry, Born approximation and linear

background density profile coincide with the ones mentioned in the section 7.5 However, some additional limitations, specific to the considered problem, have to be taken into account.

First and the most experimentally limiting approximation of the model is that of the radially uniform density fluctuations in the turning point area. It was used to obtain the solution of the equation (8.2). To overcome this limitation, generalized formulae (8.27) and (8.28) are proposed, though they are not rigorously derived from basic equations.

Another assumption that was used is (8.7), which generally holds true in the Doppler backscattering experiment.

We also used WKB approximation, but the same results can be obtained by using the exact Airy solutions, through derivation includes more complicated expressions. This was demonstrated in [56] for the Born approximation.

Finally, once again the Gaussian poloidal wavenumber spectrum of the turbulence was assumed to calculate the integrals (8.13) and (8.16). If another spectrum were to be considered, it should be substituted into those expressions, but with the way the integrals were estimated here, the use of a different spectrum would only change the numerical coefficients, which were neglected anyway. So results obtained in this chapter should be applicable for more realistic power-law spectra. Nevertheless numerical validation for non-Gaussian spectra could still be an interesting topic for future work.

A more qualitative understanding of the result for Gaussian spactrum can also be gained. The term $\delta n(-2K)$ in formula (8.9) corresponds to the fact that the main contribution to the scattering signal in the linear (Born) approximation is provided by the density fluctuations fulfilling the Bragg rule $q=-2K$. In the next order of perturbation theory the Bragg rule should be also fulfilled which means that the total poloidal wavenumber of the fluctuations taking part in the scattering is also $-2K$, which is evident from formula (8.10). However, having multiple scattering events allows a certain degree of freedom in selecting the poloidal wavenumber of each separate fluctuation. The combination of the Gaussian spectra in formula (8.13) and (8.16) leads to $q=-K$ being the poloidal wavenumber providing dominant contribution to the scattered signal in the case of quadratic approximation. This is also represented by the exponents in the formulae (8.27) and (8.28).

These arguments woud also apply for further orders of the perturbation theory, which means that for j-th order the dominant contribution to the scattering signal would be provided by fluctuations with $q=-2K/j$. That in turn means, that scattered signal power would be proportional to $\exp(-K^2 l_{cy}^2/j)\times(\delta n/n_c)^j$.

Taking this into account, one can speculate, that with the growth of δn consecutively higher orders would dominate the scattered signal, as they have weaker exponential supression. This speculation explains the results of numerical modelling presented further as well as numerical results of [64].

While formulae (8.27) and (8.28) provide the criteria of nonlinear transition for a wide parameter range we would like to note the ones relevant to experimental parameters.

In FT-2 Doppler reflectometry experiment [47] the probing parameters for O-mode lead us to L=1.5 cm, f= 30 GHz. Radial and poloidal correlation lengthes determined from experimental data are 0.2-0.4 cm, and are in agreement with gyrokinetic simulation results. In such a scenario,

formula (8.28) is applicable and for the probing angle of 35° used in experiments and the threshold value of $\delta n/n_c$ is roughly 0.2, which is higher than the one required for saturation in this case. Therefore, our threshold (8.28) predicts that nonlinear regime cannot be obtained under these experimental conditions, though curvature effects not included in the model might be significant in this case.

Another example is ASDEX Upgrade Doppler reflectometry experiment [48] with simultaneous measurement of l_{cy} and l_{cx}. In this case L=10 cm, f~ 30 GHz. The correlation lengthes defined from experiment are l_{cy}~1 cm and l_{cx}~ 3 cm. Authors also propose corrected values $l_{cy,}$ l_{cx} ~0.6 cm, which are based on numerical calculations performed to account for broadening of correlation in radial correlation reflectometry measurements predicted by linear theory [58] and described by authors similar effects in poloidal correlation reflectometry. For either pair or values, the relevant formula is (8.28) and normal probing used in experiment does not provide a possibility for nonlinear regimes. In the case of probing under similar conditions, but with a tilted antenna, formula (8.28c) would be the most relevant. Assuming that l_{cy} and l_{cx} value obtained in [48] are relevant to another L-mode ASDEX Upgrade Doppler reflectometry experiments, we can consider diagnostic setup with a tilted antenna [43]. In this case for f= 60 GHz corresponding L is roughly 20 cm which means formula (8.28) is relevant again. For a probing angle ϑ= 20° formula (8.28c) provides threshold value of $\delta n/n_c$ of 0.04, which is significantly higher than the threshold $\delta n/n_c$~0.003 provided by physical optics.

To conclude, the formulae (8.28) seem to be the most relevant for experimental parameters, in particular (8.28c) describes the situation where it is possible to observe nonlinear scattering regimes between linear and saturated regimes.

8.5. Numerical validation

To validate obtained analytical results, same as in the previous chapter numerical modelling was employed. In this case, however, linear modelling was not sufficient and therefore full-wave modelling with the IPF-FD3D code [25] described in section 4.2 was performed.

Two types of simulations were carried out. The first one directly corresponded to the theoretical model and featured a 1D turbulence uniform in radial direction. The second type corresponded to a more realistic 2D turbulence possessing finite radial correlation length.

Like analytical consideration, computations were performed in the slab geometry. To generate random turbulence the density fluctuation Fourier transform amplitude $\delta n(\kappa,q)=\delta n_0\sqrt{l_{cy}l_{cx}/8\pi}\exp\left[-q^2l_{cy}^2/8-\kappa^2l_{cx}^2/8\right]$ was used. Random phases were added to the amplitude of each harmonic and then an inverse Fourier transform was performed. Each random turbulence field obtained this way was set to have r.m.s. of 1 and then scaled to a certain fraction of n_c. The turbulence field was applied to a linear backgorund profile.

Each computation was performed over 6000 separately generated turbulence fields. Numerical results were then averaged to produce the final result. This way a realistic random turbulence was used in calculation while it's spectral properties were still in agreement with analytical model. All the calculus was performed for a "frozen" density without temporal dependence in agreement with the analytical model.

An example of densities for two types of computation can be seen on figures 8.2 and 8.3 respectively. For the first figure, l_{cy}=1 cm and turbulence r.m.s. is set to 0.1n_c. The probing

frequency f is 40 GHz and L is 20 cm. In the second figure radial correlation length of the turbulence is 1 cm and the rest of parameters are same as in figure 8.2.

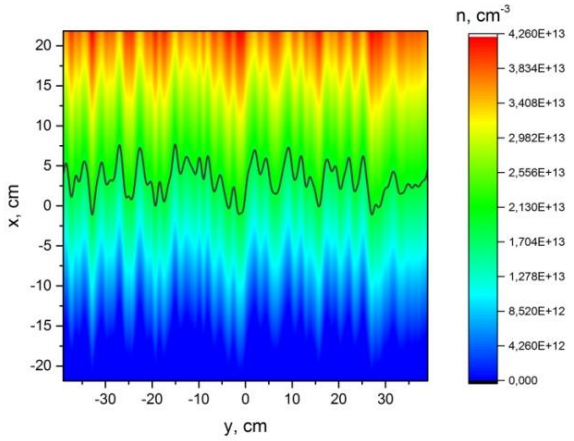

Figure 8.2: Density profile with random fluctuations uniform in the radial direction. Grey line designates cut-off density for the probing frequency used in FD3D calculations.

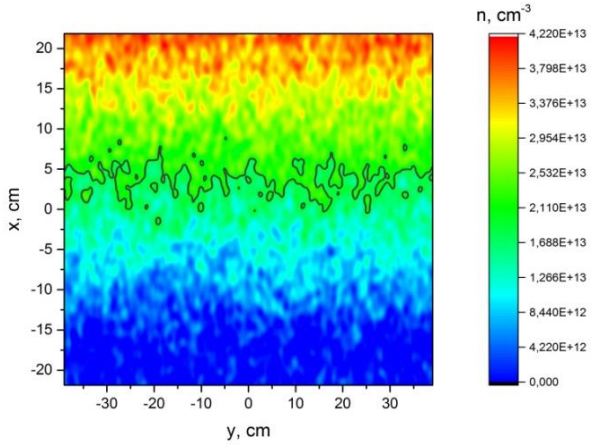

Figure 8.3: 2D density profile with random fluctuations. Grey line designates cut-off density for the probing frequency used in FD3D calculations.

Moving on to the computations, for the one with radially homogenous turbulence L=20 cm, l_{cy}=1.3 cm and ρ= 4 cm were used. On the figure 8.4, scattered signal power depending on turbulence amplitude is plotted for two different probing angles. Turbulence amplitude characterized by as follows: r.m.s.$(\delta n)=a\times n_c$. Lower half of the graph also shows the power scaling value $n_i=\ln(P_{i+1}/P_i)/\ln(a_{i+1}/a_i)$. The subscript i in this formula refers to a specific value of tubulence r.m.s. a_i used in a calculation. The value n_i is a characteristic of the power dependence of scattered field power with the growth of turbulnce amplitude: $P \propto a^n$

In the linear regime scattered field amplitude depends linearly on turbulence r.m.s. which means that dependence of the scattered signal power is quadratic and the value of n_i is 2, which is indeed the case for small values of a. As the fluctuations become stronger, higher regime of nonlinearity can be seen with n_i increasing to higher numbers. After that the transition to the strong phase modulation regime occurs which leads to saturation of the scattered power, which can be seen in n_i decrease.

Vertical lines on the picture correspond to different criteria derived previously. Solid olive line corresponds to approptiate for this case (8.19b), dashed purple line is saturation criterion (8.25a) and dotted brown line corresponds to physical optics result which is described by (8.19a). It can be seen that for these parameters the difference between our consideration and physical optics results is quite significant. It seems that in the considered case of radially uniform turbulence our criteria predicts the transition to nonlinear regimes more precisely than physical optics model.

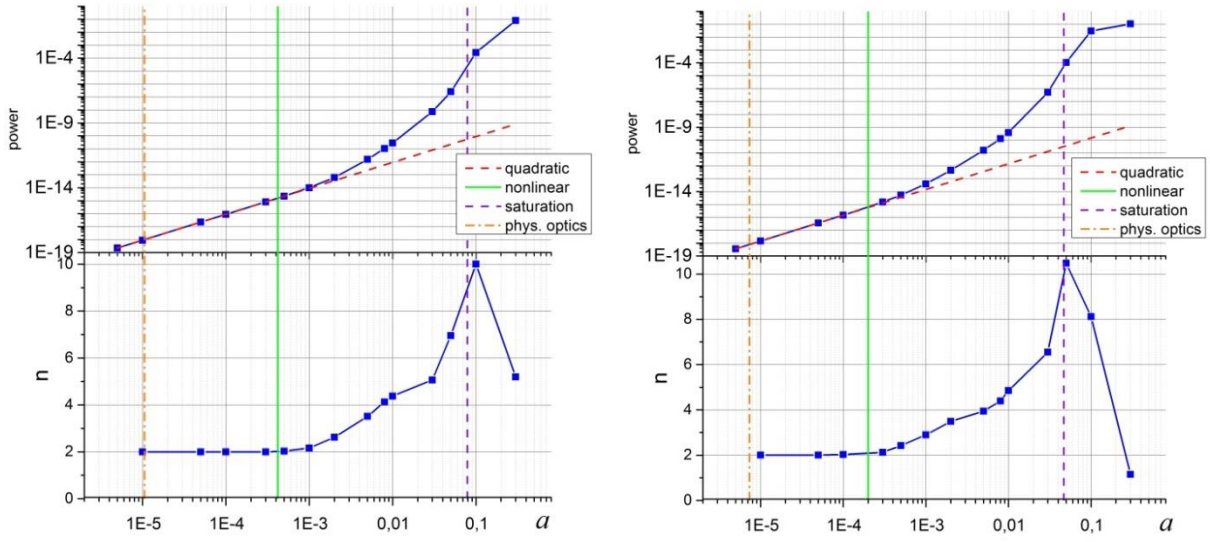

(a) (b)

Figure 8.4. Scattered signal power and its exponential scaling calculated in case of radially uniform turbulence depending on turbulence amplitude a for (a) l_{cy}=1.3 cm and the probing angle ϑ= 40° and for (b) l_{cy}=1.3 cm and the probing angle ϑ= 30°. The dashed red line corresponds to quadratic power dependence. Vertical lines correspond to nonlinearity thresholds: solid green line - our analysis, formula (8.19b); orange dash-dotted line - physical optics, formula (8.19a); purple dashed line –saturation, formula (8.25a).

An example of a more realistic calculation with 2D isotropic turbulence is plotted on the figure 8.5. Probing parameters in this case were also L=20 cm, ϑ= 40° and ρ=4 cm. The vertical lines in this case correspond to generalized version of the same criteria - solid olive line is formula (8.28c), the dash-dotted brown line is the criterion obtained in [64] (and given by (8.27a)) and dashed purple line is saturation criterion (8.26). Just as in the case of 1D turbulence, in 2D calculations physical optics model underestimates the threshold density fluctuation amplitude for the transition to nonlinear regimes while our criterion provides a correct value. As can be seen from figure 8.5, the difference between both is more than of one order of magnitude which makes physical optics criterion significantly more limiting in this case. Although it should be mentioned, that for different values of parameters this diffference can be much smaller and even neglegible (which happens as the paramater values approach the intermediate region in agreement with (8.27) and (8.28)).

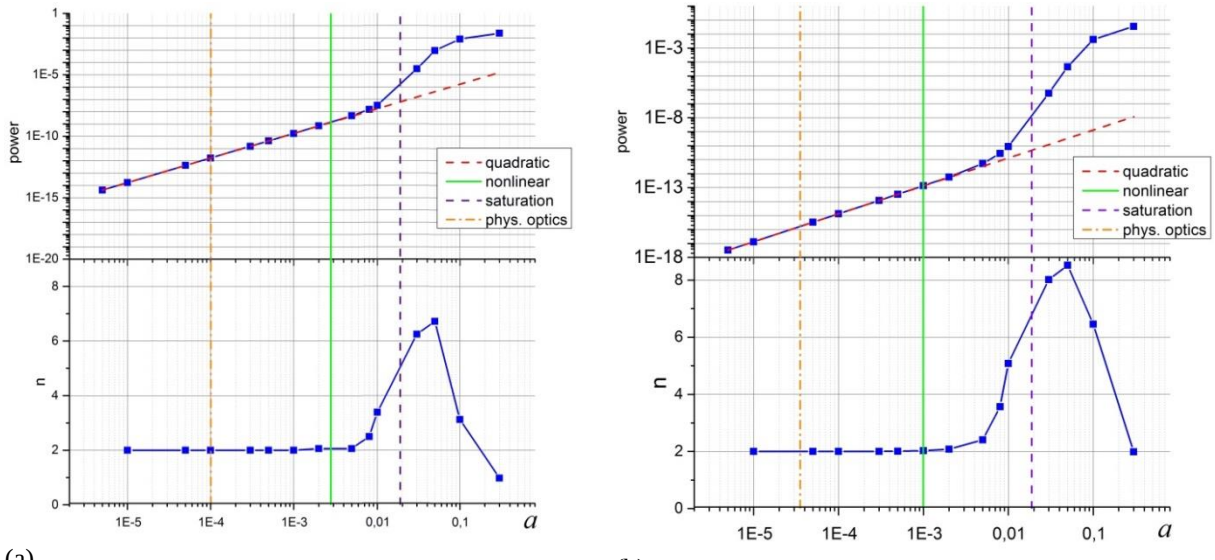

(a) (b)

Figure 8.5: Scattered signal power and its exponential scaling depending on turbulence amplitude a in case of 2D turbulence with (a) l_{cx}=l_{cy}=1.3 cm and (b) l_{cx}=l_{cy}=1.2 cm. The dashed red line corresponds to quadratic

power dependence. Vertical lines correspond to nonlinearity thresholds: solid green line -formula (8.28c); orange dash-dotted line - physical optics (8.27a); purple dashed line –saturation, formula (8.26).

However in the cases when (8.28c) predicts a nonlinear transition at density perturbation amplitudes so high that saturation would happen before the nonlinear transition occurs, our numerical results are not in agreement with (8.28c). An example of such a calculation can be seen at figure 8.6.

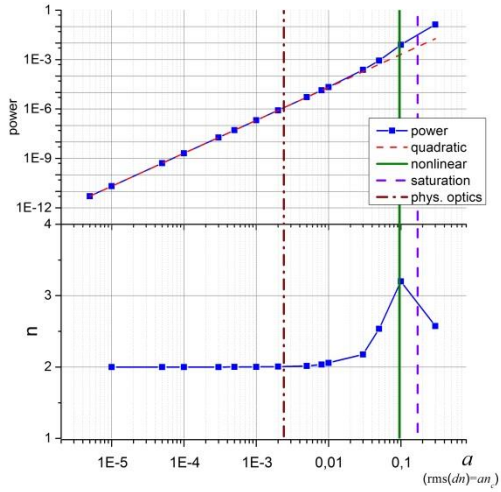

Figure 8.6: Scattered signal power calculated depending on turbulence amplitude a in case of radially uniform turbulence with f=30 GHz and l_{cy}=0.6 cm. The dashed red line corresponds to quadratic power dependence. The vertical lines correspond to nonlinearity thresholds: solid olive line - formula (8.20c); brown dash-dotted line - physical optics, formula (8.19a); purple dashed line –saturation, formula (8.25a).

The possible cause of this discrepancy could be that in such situation Kl_{cy}~1, which is the limit of validity of formula (8.20c). In this case formula (8.20b) becomes relevant, however numerical coefficient associated with it is unclear since the integral estimation in that case was rather rough (which is why it was neglected). This omitted numerical coefficient we assume that is the main cause for discrepancy. However, an exact estimation of the coefficient and consequently validation of this explanation would require further studies of the analytical formulae derived in previous sections of this chapter with the help of simulations.

One issue that was adressed during computations was the fact that uniform turbulence shown in figures 8.2 and 8.3 displays a very high turbulence level at plasma edge. To remove this effect the turbulence was suppressed at the edge by multiplying the initial turbulent function by a hyperbolic tangent with a step located at $L/2$. Despite the fact that such operation could limit the area of small-angle scattering and cause the change of treshold value of a, even for such a drastic damping, the outcome of full-wave computation did not qualitatively change, leading us to a conclusion that a strong edge turbulence did not significantly influence the scattered signal in presented cases in the first place. An example of the computation presented on the figure 8.5a for both original turbulence and “damped edge” turbulence is presented on the figure 8.7. The change of threshold, while present, did not put the numerical resutls out of range of the theoretical prediction.

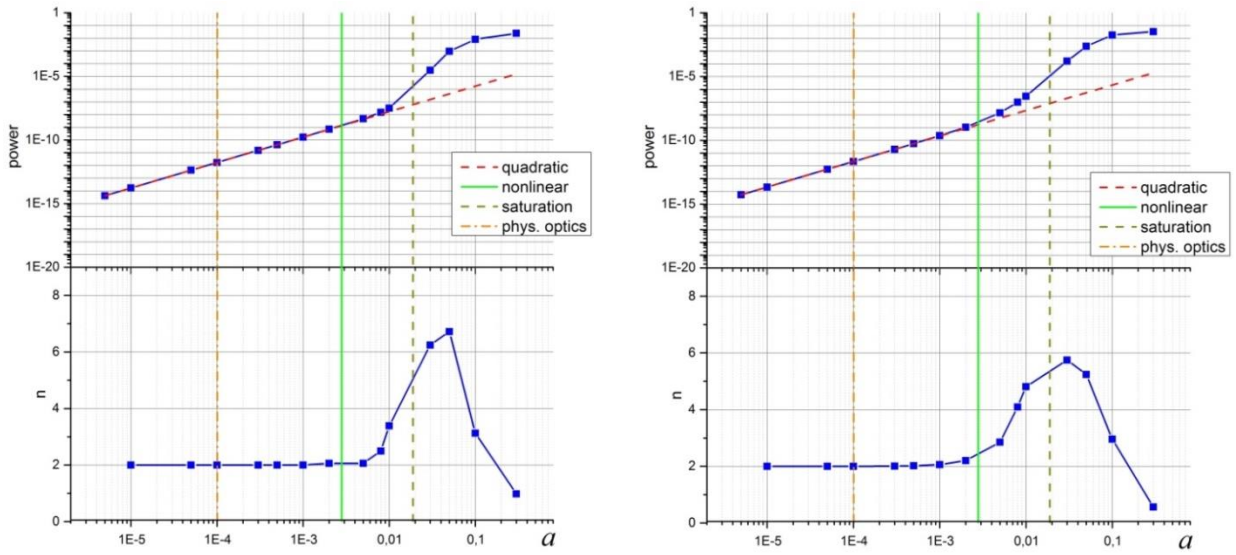

(a) (b)

Figure 8.7: Scattered signal power and its exponential scaling depending on turbulence amplitude a in case of 2D turbulence with (a) uniform amplitude and (b) amplitude damped at the plasma edge. The dashed red line corresponds to quadratic power dependence. Vertical lines correspond to nonlinearity thresholds: solid green line - our analysis, formula (8.28c); orange dash-dotted line - physical optics (8.27a); olive dashed line –saturation, formula (8.26).

Finally, to validate the explanation for a continuous growth of nonlinearity with the growth of δn proposed in 2.3 a calculation with a step-like poloidal turbulence spectrum was performed:

$$\delta n(\kappa, q) = \begin{cases} \delta n_0 & |q| < k_0, |\kappa| < k_0 \\ 0 & |q| > k_0 \text{ or/and } |\kappa| > k_0 \end{cases}$$

The value of k_0 was selected so that $K<k_0<2K$. For this spectrum according to our speculation, higher orders of nonlinearity would lose the exponential advantage provided by the Gaussian spectrum, while linear scattering would be suppressed due to absence of turbulence with high enough poloidal wavenumbers. The numerical values for the simulation were: f= 30 GHz, L= 20 cm, ϑ= 40° (which means that K=4.4 cm^{-1}), ρ=4 cm and k_0=5 cm^{-1}. The results are presented at figure 8.8:

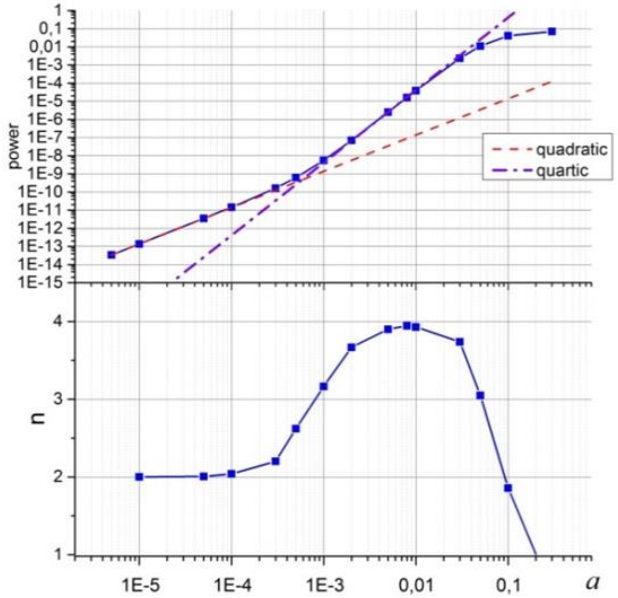

Figure 8.8: Scattered signal power and its exponential scaling in cases of step-like spectra. The red dashed line and purple dash-dot lines correspond to quadratic and quartic power dependencies respectively.

The value n_i in this case does not exceed 4, which is in agreement with our expectations, as it means higher orders of scattering are no longer dominating scattered signal. This confirms our speculation that higher orders of scattering only become possible when fast decrease of turbulence amplitude with poloidal wavenumber is present. At low turbulence amplitude linear scattering regime is observed despite the absence of density fluctuations capable of producing linear scattering signal in the turbulence spectrum. This can be explained by the finite width of the probing beam which makes linear backscattering at lower poloidal wavenumbers possible. Such backscattering signal is weak due to the absence of corresponding poloidal wavenumbers in antenna pattern, but can dominate a scattered signal when turbulence amplitude is low enough.

A final topic that should be addressed the effects observed in the simulations not presented in this thesis. While only some key computations are presented a range of parameter values was explored to gain some insight into the sensitivity to parameters. First of all, in agreement with the explanation previously given for the figure 8.6 the inconsistencies with the analytical formula only seemed to manifest when Kl_{cy}~1. Changing parameters like L and ρ did not seem to affect the agreement with theory. Secondly, while in the presented results suppressing the edge fluctuations did not cause a significant change in the simulation results, for some cases the change of the threshold would be as drastic as a factor of 10 for the suppression at $L/2$. A further numerical study could be worthwhile to study inconsistencies with analytical results in more detail.

8.6. Conclusions and discussion

In this chapter we have analytically investigated the onset of nonlinearity for the DR diagnostic. The analytical results were obtained for radially uniform plasma turbulence and then generalized to describe turbulence with arbitrary radial correlation length. Depending on the set up and plasma parameters different thresholds for a transition to nonlinear regimes were established. Analytical results were validated with full-wave simulations for both radially uniform and fully 2D turbulence and an agreement between analytical nonlinear thresholds and full-wave simulation results has been shown. This agreement shows that the thresholds obtained can be applied to experiments according to the mentioned restrictions. An explanation for the scattered signal power dependence has been deduced from the extension to higher orders of perturbation method and validated numerically.

Such explanation based on the interplay before turbulence poloidal wavenumber spectra and amplitude effects gives us grounds to make another prediction for the case of experimental (power law) spectrum. Since such spectrum decays slower than exponential one, it would make it harder to access higher orders on nonlinearity since the suppresion of linear signal due to the absense of the turbulence with high enough q in the spectrum would not be as strong. That in turn means that we would expect nonlinear effects to come into play for higher turbulence amplitudes. This effect of the spectrum slope on the onset of nonlinearity will be demonstrated in practice in the chapter 9.

The new expressions obtained, in particular, expression (8.28c) are relevant for determining the limits of validity of linear approximation and numerical scheme based on it (as described in section 4.1). Since the synthetic diagnostic, which is described in the next chapter focuses mainly on the impact of nonlinear effects, it would certainly be interesting to apply the obtained results for the specific FT-2 experiment, which is under consideration in the next chapter.

For O-mode, we already estimated the threshold value to be higher than saturation value in section 8.4. In the case of the X-mode, using the scale length of the squared wavenumber in the vicinity of the turning point (which was obtained from the gyrokinetic modelling results) instead of L, the threshold value of 0.07 was obtained for the antenna positioned at +2cm above equatorial plane and experimental conditions described in section 5.2. The saturation criterion for this case also provides the same threshold value of 0.07.

The gyrokinetic data also provides the value $\delta n/n_c$=0.06-0.09 from the turbulence r.m.s. in the probed area. This means that FT-2 diagnostic should indeed be operating in linear regime for O-mode and close to nonlinear regime for X-mode. As the next chapter will show, that is indeed the case.

9. Synthetic DR and RCDR diagnostics

The last and the main part of this thesis is the creation of the synthetic DR and RCDR diagnostics, their benchmarking with experiment as well as analysis of the nonlinear scattering effects and their impact on measurements.

The path chosen to create the diagnostics is as follows: first of all, RCDR experiment at the FT-2 tokamak was conducted, DR and RCDR measurements were performed and experimental frequency spectra, CCF and poloidal wavenumber spectrum were obtained. Besides that, as described in chapter 5 experimental profiles were used to perform plasma modelling with ELMFIRE code and 2D arrays of electron density, accounting for the plasma turbulence, were obtained. These modelling results were then used as input parameters for the IPF-FD3D computation (they were preprocessed to have smoother edges by adding a layer of exponential decrease to the ELMFIRE density's edge), which provided the synthetic DR signal. This signal was then used to extract spectra and CCF, which finally, were compared with experimental ones.

As described in the chapter 5, ELMFIRE computations produced the density temporal dependence with the simulation duration of 150 μs and by steps of 0.15 μs. Since this step is larger in comparison with the propagation time of the probing wave, the IPF-FD3D computations were performed separately for each turbulence instance, meaning the turbulence in each computation did not change in time. Also, the ELMFIRE computation provided the density over 8 poloidal cross-sections corresponding to different toroidal angle. These cross-sections were assumed to be independent one from each other, and were used as a source of additional statistics.

The computations were performed simultaneously for all the probing frequencies necessary for RCDR modelling and the largest grid size used was 1300x700 cells (corresponding to the case of X-mode probing and $dx=c/24f$, where f is the highest probing frequency in the computation). In this case, the computation of all 8000 snapshots of density on a single Intel Xeon 2.4 GHz CPU took approximately 400 hours. For the reference, the same computation with a linear diagnostic described in section 4.1 and in [45] only took four hours. Such computation, however, has proven to be insufficient for the FT-2 RCDR modelling.

Aside from the benchmarking with experiment, a number of computations were performed to study the nonlinear scattering effects. For that the density that is the output of ELMFIRE was separated into background density profiles and density perturbations profiles (by averaging in time) and the latter was multiplied by a factor a same as it was done in chapter 8. This approach allowed to scan over the amplitudes of density perturbations and to distinguish between linear and nonlinear regimes of DR and RCDR.

Due to the strong dependence of its refractive index on the plasma density, X-mode is more susceptible to nonlinearity, which made it the prime object of the studies, as well as numerical modelling. For that reason, the results presented in sections 9.1 and 9.3 will correspond to X-mode probing, with O-mode probing modelling being presented later in the section 9.4.

9.1. Experimental benchmarking of X-mode modelling

In this section, we will compare the results of the synthetic diagnostic developed within the scope of this thesis with experimental measurements as well as previously developed linear ("fast") synthetic diagnostic's results.

In the case of DR, first of all, the frequency spectrum was considered for a number of possible antenna vertical displacements from equatorial plane y_a (as described in chapter 5). The results of the nonlinear synthetic diagnostic are presented on the figure 9.1 along with linear modelling results and experimental measurements:

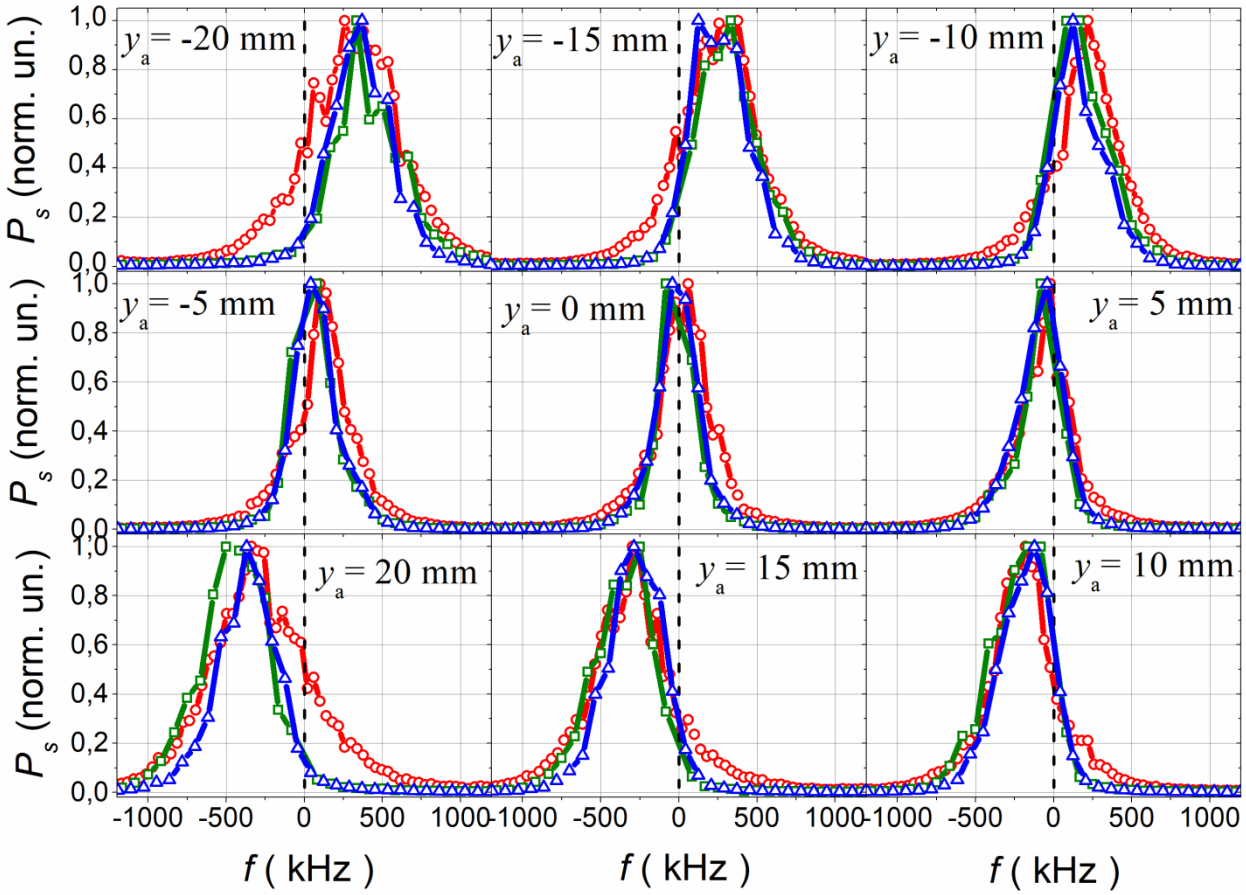

Figure 9.1: DR frequency spectra corresponding to different vertical positions of the probing antenna. Blue triangles correspond to linear synthetic diagnostic, green squares –full-wave synthetic diagnostic, red circles – experiment.

To obtain these spectra, the total of 8000 temporal points of the ELMFIRE calculation were divided into windows of 80 points (=12 μs), where the frequency spectrum was computed. After computation, the resulting power spectrum was averaged over all the windows to produce the final result. In case of linear modelling, the method was exactly the same, while in case of experimental measurements, available temporal interval was larger.

As it is seen in the figures, the spectra provided by both of the synthetic diagnostics fit reasonably well the experimental ones for all the antenna positions. Only at the maximal antenna shifts both of the synthetic diagnostics fail to describe the wing of the experimental spectrum opposite to the spectrum frequency shift direction. Nevertheless, the shifts of both spectra are close in all cases, and their shapes are similar too. This impression is further confirmed by figures 9.2 and 9.3, where the mean frequency shift $f_D = \int f P_s(f) df \,/\, \int P_s(f) df$ and the mean frequency width $\Delta f = \int (f - f_D)^2 P_s(f) df \,/\, \int P_s(f) df$ of the experimental and synthetic spectra (obtained as the first and the second moment of the spectrum, respectively) are plotted as a function of the antenna vertical displacement and the turbulence poloidal wavenumber.

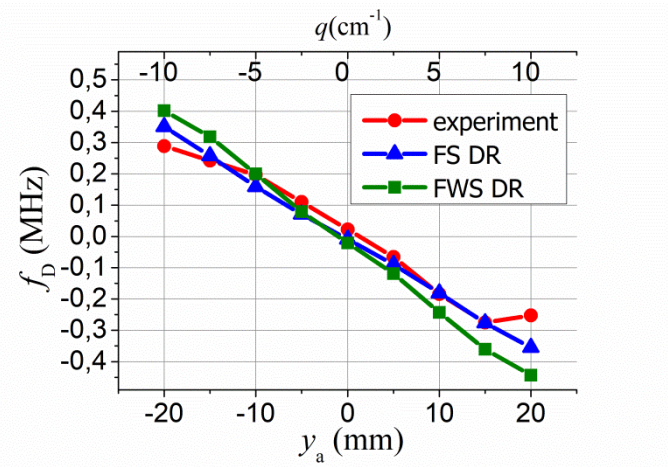

Figure 9.2: Dependence of the DR signal frequency shift on the antenna vertical displacement y_a and fluctuation wavenumber. Circles –experiment; triangles – fast (linear) synthetic DR; squares full-wave synthetic DR.

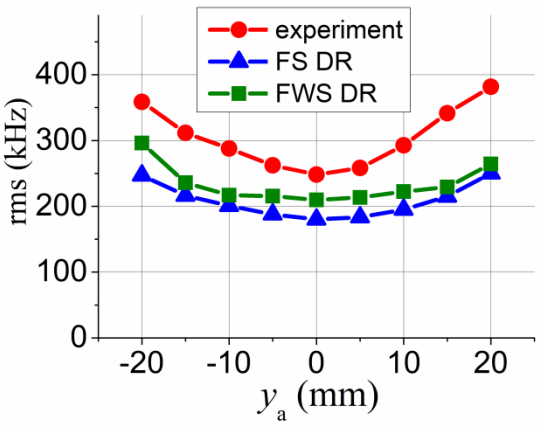

Figure 9.3: Dependence of the DR signal frequency width (rms) on the antenna vertical displacement y_a. Circles –experiment; triangles – fast synthetic DR; squares full-wave synthetic DR.

The relation between the antenna displacement and the fluctuation poloidal wavenumber was obtained using the X-mode ray-tracing (as the doubled value of the probing wave poloidal wavenumber at the turning point). The spectral shift data provided by the experiment and GK modelling agree rather well. The meaningful difference is only observed at the largest antenna displacement $y_a = \pm 2.0$ cm. This difference is probably due to a contribution of experimental spectrum wings becoming especially heavy and asymmetric at high antenna displacement and, consequently, fluctuation poloidal wavenumber. As it was mentioned, the wing is opposite to the mean frequency shift of the spectrum and, presumably, is caused by small-scale drift modes excited in the plasma at a low level. These modes rotating in the direction of the ion diamagnetic drift might be poorly described by the GK code, since the smallest scales can be close to limit of grid resolution and are also most sensitive to the particle noise

Fig. 9.2 allows us to obtain estimations for the fluctuation poloidal velocity in experiment and in the computation. The estimation of the mean fluctuation poloidal velocity in experiment is given by $v_{pol}=2\pi f_D/q \approx 2.1$ km/s, whereas the synthetic DR computations result in $v_{pol}=2\pi f_D/q \approx 2.0$ km/s for the fast diagnostics and $v_{pol}=2\pi f_D/q \approx 2.4$ km/s for the full-wave one. The obtained agreement between the measured and computed DR spectra, which are determined by the plasma flows, provides evidences in favor of correct modelling of plasma poloidal rotation and a correct reproduction of the radial electric field behavior in the FT-2 tokamak by the ELMFIRE code. Moreover, the velocity obtained directly from ELMFIRE using the value of radial electric field also provides the value 2.1 km/s, while the temporal correlation analysis of the density fluctuations gives the value 2.5 km/s. Both of these values are close to the ones obtained in experiment and by synthetic diagnostics. It should also be noted that the discrepancy between all these values is of the same order at the difference of poloidal velocities between r=5.5 cm and r=6.5 cm.

As it is seen in Fig 9.3, the mean width of synthetic spectra is systematically smaller than in experiment. However, the difference is in the range of only 20 – 30 %. It could be attributed to the contribution of the spectral wings, which are higher in the experiment.

We have also compared the DR signal intensity $\int P_s(f)df$ dependence on the vertical antenna displacement, which is expressed at the figure 9.4 in terms of the poloidal wavenumber

of the turbulence. As mentioned previously, this dependence characterizes the poloidal wavenumber spectrum of the turbulence.

As it is seen in Fig.9.4, the decrease of the DR signal power with growing fluctuation poloidal wavenumber is substantially faster than in experiment for both synthetic diagnostics. The difference could be attributed to at least two possible reasons. The first reason is related to incorrect modelling of ETG mode-scale fluctuations leading to their suppression, and absence of the inverse energy cascade in the wavenumber space, which can result in an underestimation of the turbulence poloidal wavenumber spectrum also in the intermediate-scale domain q~10 cm^{-1}. It can occur in spite of a sufficiently high density of the ELMFIRE code grid (poloidal cell size 0.07 cm). This reason could lead to a faster decay of the synthetic signal power at large antenna displacement.

The second reason is related to a possible underestimation of the total density fluctuation level by the GK code. As it was previously described, higher amplitude of the turbulence could cause the saturation of the signal for some spectral components and result is a slower decay of signal amplitude than dictated by turbulence poloidal spectrum. The same consequences could result from neglecting multiple wave reflections between the cutoff and the antenna taking place at the equatorial probing in the synthetic diagnostics. To illustrate this reason, figure 9.5 shows the dependence of the amplitude of synthetic signal for the case of ELMFIRE turbulence being artificially multiplied by a factor of 1.5.

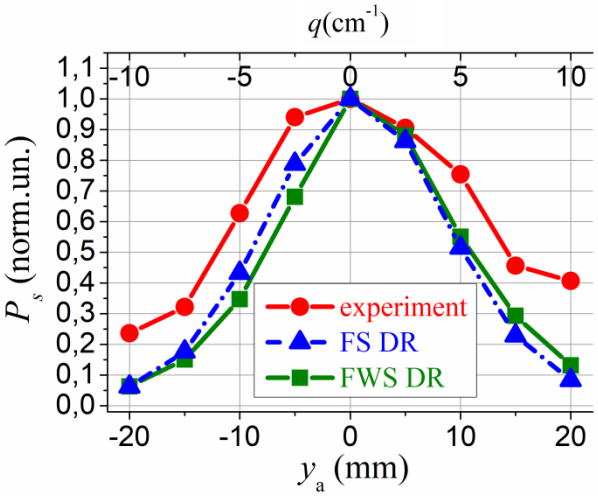

Figure 9.4 Dependence of the backscattering power on the fluctuation poloidal wavenumber and antenna vertical shift. Circles –experiment; triangles – fast synthetic DR; squares – full-wave synthetic DR.

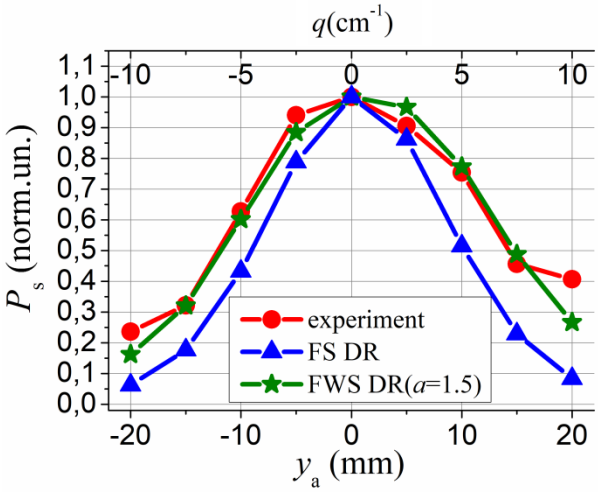

Figure 9.5. Dependence of the backscattering power on the fluctuation poloidal wavenumber and antenna vertical shift. Circles –experiment; squares – full-wave synthetic DR, stars– FWS DR with density fluctuations level multiplied by 1.5.

Finally, the poloidal spectrum of the turbulence can be directly calculated from ELMFIRE data. The result of such calculation in comparison with the synthetic diagnostics and experimental data is presented at figure 9.6 for both positive and negative antenna displacements. It can be seen, that the general shape of the slope is actually closer to the synthetic diagnostics rather than to the experimental results, as it would be expected.

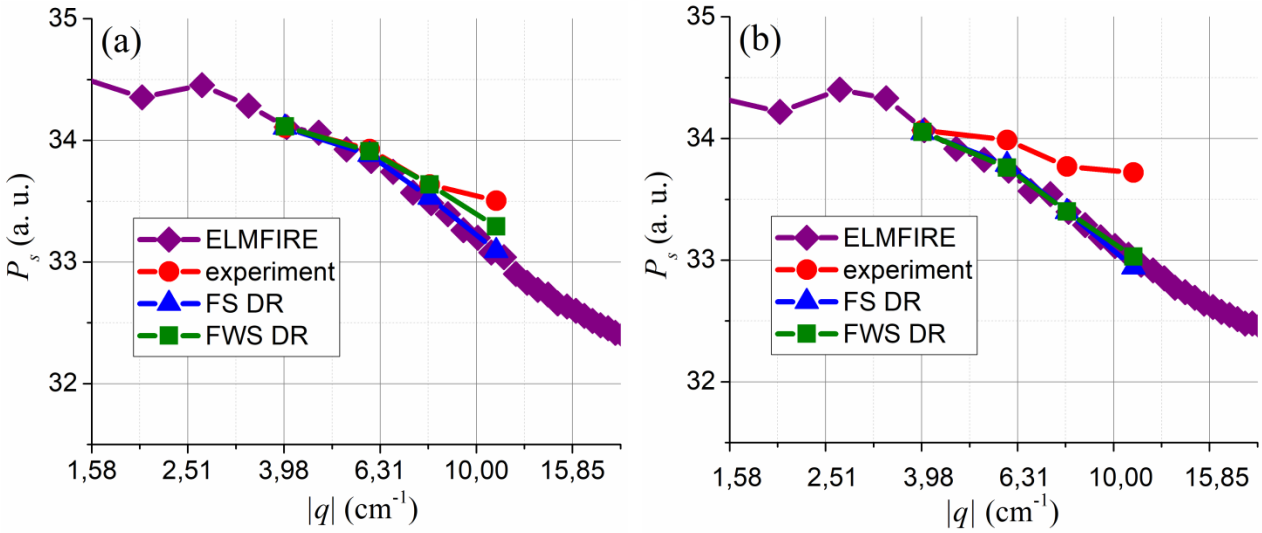

Figure 9.6. The comparison of the turbulence poloidal wavenumber spectrum directly computed from ELMFIRE data with the ones inferred from DR measurements and synthetic signal at the (a) upper and (b) lower HFS of the tokamak in double logarithmic scale. Diamonds corresponds to the ELMFIRE data direct Fourier transform, circles – experiment, triangles – fast synthetic diagnostic, squares - full-wave synthetic diagnostic.

Overall, both full-wave and linear synthetic diagnostics show a good agreement with experimental measurements, suggesting not only validity of ELMFIRE results, but also a linear regime of DR operation. The only observable discrepancy is in the turbulence poloidal spectrum measurement, and possible explanations for it were proposed. At the same time, the agreement between modelling results for linear and full-wave modelling, as well as with direct ELMFIRE data analysis suggest that in this case the diagnostic operates in the linear regime. This notion will be further explored in subsequent section, where analysis of nonlinear effects will be performed.

But before that, the final part of this section is the comparison of RCDR measurements with the synthetic data. We have performed the comparison of the computed and measured RCDR CCFs using the X-mode DR antenna displaced by +2.0 cm from the equatorial plane at the high-field side of the FT-2 tokamak. The corresponding CCFs (shown in Fig.9.7 as functions of the frequency difference in the master and slave channels (a) and of the separation of turning points (b), which was determined using ray tracing for different probing frequencies, as the difference of minimal radii of the two trajectories) appear to be different, whereas the density fluctuations two-point CCF for frequency f_s-f_i= *300 kHz* computed in the measurement region based on the GK data and shown in Fig.9.7b is close to the measured RCDR CCF, as it was mentioned in [47]. However, we assume that this coincidence is just accidental. The CCF provided by the fast synthetic DR is much wider than the experimental one, whereas the full-wave synthetic CCF is situated in between, as it is seen in Fig.9.7a.

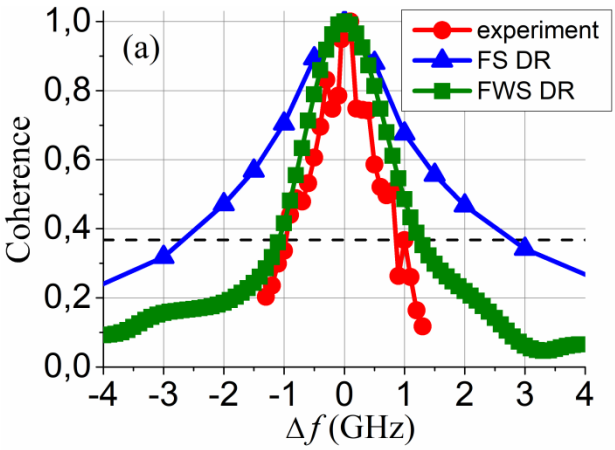

Figure 9.7a: The RCDR CCF against the channel frequency separation. Triangles – fast synthetic DR; squares – full-wave synthetic DR; circles – experiment.

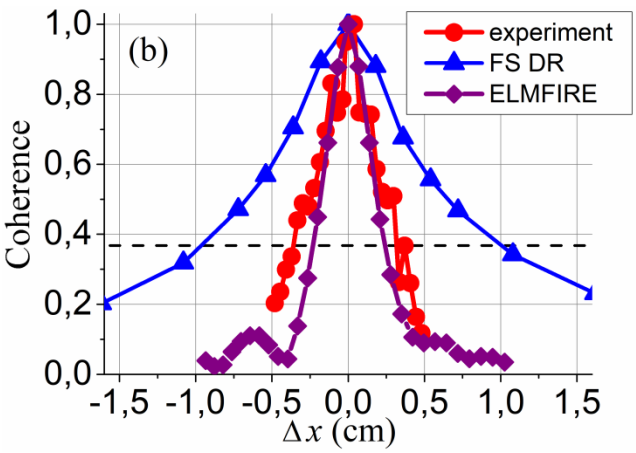

Figure 9.7b: The RCDR CCF against the turning point radial separation. Triangles – fast synthetic DR; circles – experiment; diamonds – turbulence CCF computed directly from ELMFIRE.

There are two possible reasons of the drastic difference between the experimental and the fast synthetic RCDR CCFs. The first one is related to the influence of nonlinear effects, in particular, the multiple small-angle scattering, or strong probing wave phase modulation, according to theory [19][20], coming into play with growing turbulence level and not being included in linear synthetic diagnostic. The importance of this effect for the DR diagnostics performance was shown recently at ASDEX Upgrade [30]. The slow decay of the CCF provided by fast synthetic diagnostics shown in Fig9.7a,b is then determined by the small-angle-scattering contribution to the DR signal (as described in chapter 3), which is not suppressed at the angle of incidence corresponding to y_a = +2.0 cm.

The second reason is related to the GK code spatial grid limitations leading to an underestimation of the turbulence radial wavenumber spectrum width, and thus – to the overestimation of the RCDR CCF width. As it is seen in Fig.9.7a, the CCF provided by the full-wave synthetic diagnostics is much closer to the experimental one. This agreement shows that the second reason mentioned above probably plays a minor role, thus providing an argument in favour of a correct description of the turbulence radial wavenumber spectrum by the GK code.

9.2. Different ELMFIRE cases used for modelling

Aside from the experimentally relevant ELMFIRE case, which was used to obtain the results of the previous section, two other ELMFIRE computations were available.

One of them was ELMFIRE run based on a temperature profile which did not directly correspond to the experimental one and had higher electron temperature in the probing wave cutoff region (220 eV instead of actual experimental value of 100 eV). The grid in the poloidal direction only had 150 points at every minor radius and the resulting turbulence obtained in this case possesses a steeper poloidal wavenumber spectrum. While less comparable to the FT-2 tokamak experiment, this case was expected, as it was predicted in the chapter 8, to provide clearer indication of nonlinear effects influencing the DR frequency spectra compared to the experimental one while still using a realistic turbulence. This is connected to the fact that the linear signal is proportional to the components of spectrum with higher poloidal wavenumber q while nonlinear one is caused by multiple scattering off the lower q turbulence, which makes steeper spectrum be more favorable for nonlinear effects to manifest.

Finally, the ELMFIRE calculation that breached the gap between both cases by using experimental profiles and hoarse grid with 150 poloidal points was available. This calculation was not used for the full-wave computations, aside from a quick computation of DR spectrum using only partial data available and demonstrating the absence of the principally new effects in this case.

The poloidal wavenumber spectrum of the turbulence, calculated directly from the ELMFIRE data for all the cases is shown on the figure 9.8 for upper and lower HFS. It can be seen that the experimental case indeed possesses a flatter spectrum, while the narrower spectrum in the lower temperature case can be connected both with the input difference and hoarse grid (since all three cases give different shape of spectrum at the upper HFS).

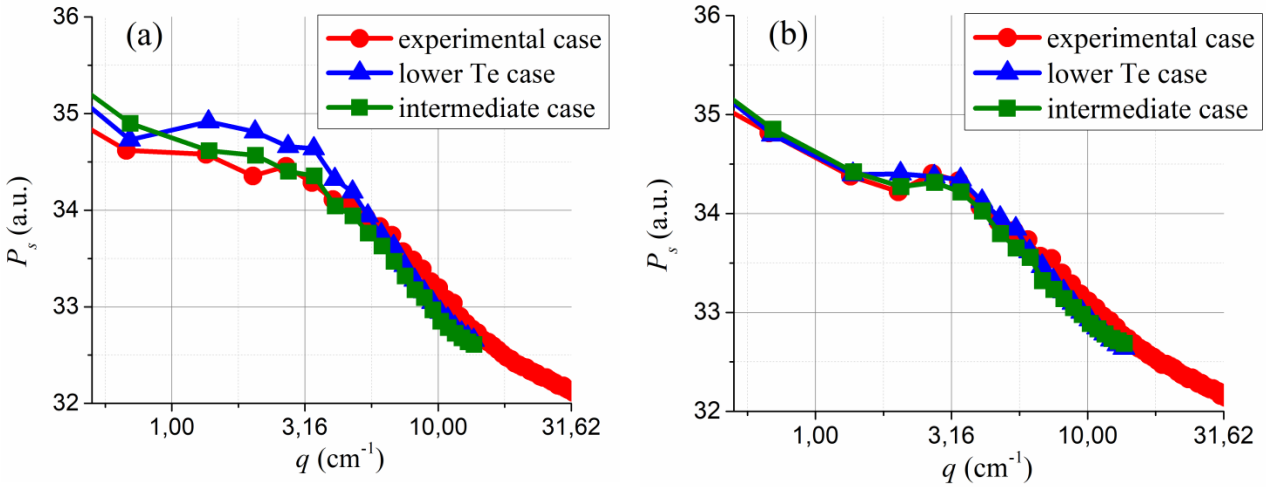

Figure 9.8: The poloidal wavenumber spectrum calculated for probed minor radius r=6 cm from ELMFIRE data for different simulations at the (a) lower and (b) upper HFS. Circles correspond to case with fine used in section 9.1, triangles – lower T_e case, squares – intermediate case.

9.3. Nonlinear scattering effects in X-mode modelling

We will start this section by presenting the lower-temperature case that does not directly correspond to the experiment, since it is the most interesting from the standpoint of studying the nonlinear scattering effects.

First of all, the figure 9.9 presents the computation of the DR spectra corresponding to this case for different antenna positions. The most drastic difference between this case and experimental one is observed at large antenna shifts. This goes in line with the idea that the narrow poloidal wavenumber spectrum of the turbulence for this case causes the linear scattering signal to become smaller than nonlinear one (since it corresponds to lower values of q and is less affected by a steeper spectrum). For that reason, the antenna position y=2 cm was chosen for further study.

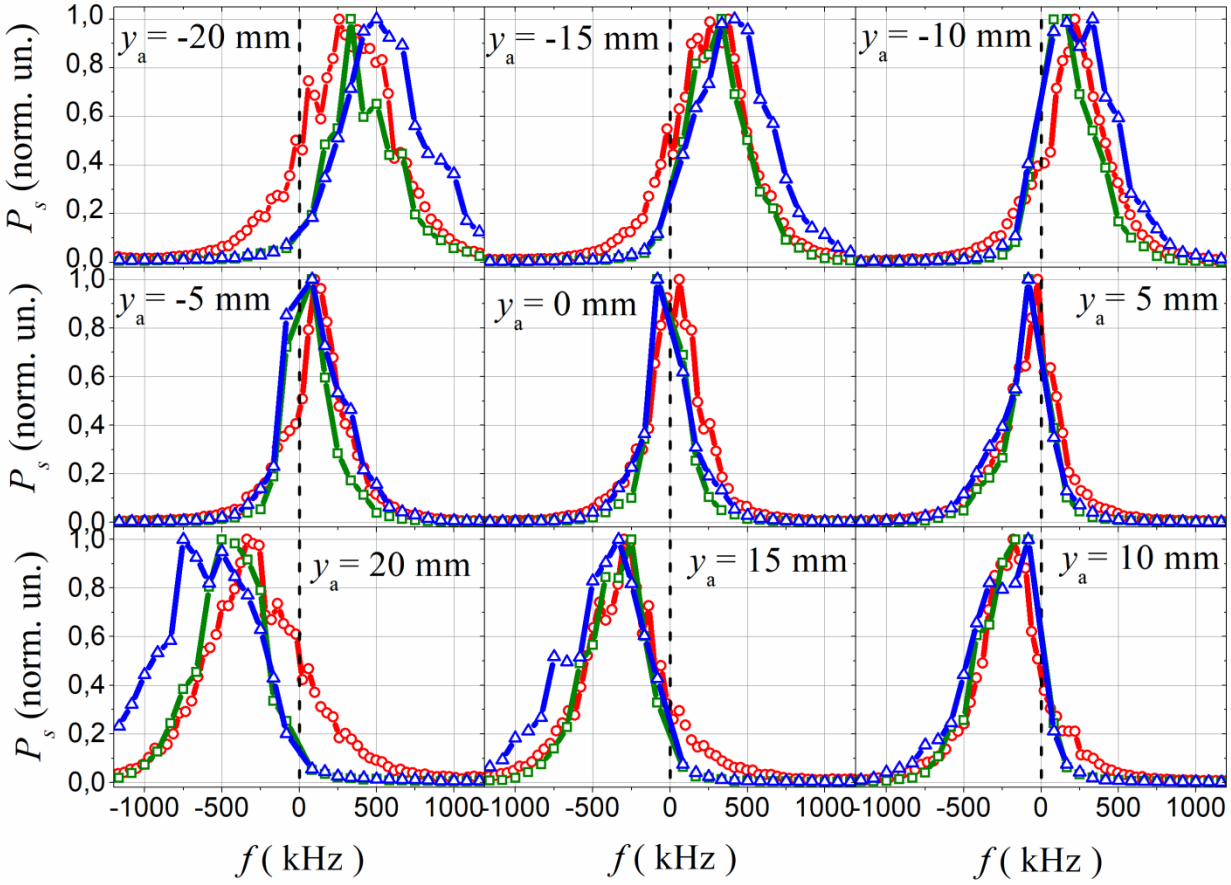

Figure 9.9: Synthetic DR spectrum for two ELMFIRE cases corresponding to different vertical displacement of the probing antenna. Blue triangles correspond to the lower T_e case synthetic diagnostic, green squares –experimental case synthetic diagnostic, red circles – experimental measurements.

A scan over the turbulence amplitude was performed by artificially changing the amplitude of the turbulence provided by ELMFIRE and full-wave computations for each amplitude were performed. The DR frequency spectra for a number of different turbulence amplitudes (with Δf corresponding to the frequency shift from central probing frequency f_0) is plotted in the figure 9.10, while figure 9.11 demonstrates the dependence of the total scattered power received by the antenna. Figure 9.11 is plotted against the dimensionless factor a by which the amplitude of the turbulence produced by ELMFIRE code is multiplied. That means that a=1 corresponds to the original ELMFIRE turbulence, while a=2 means that the turbulence was artificially enhanced twofold for the full-wave computation.

From the figures it can be seen that with the growth of the turbulence amplitude, DR spectra shift to higher frequencies. The notion of this shift being caused by a nonlinear effect is further confirmed by the signal power growing at a rate different from quadratic for the higher a-values in the figure 9.11. On the top half of the figure the scattered signal power is plotted. At about a=0.5 the growth becomes faster than linear, which corresponds to the nonlinear regime, described in chapter 8, while for a-values of 1 and higher the nonlinear saturation described by the analytical theory [19][20] and shown in the computations of chapter 8 can be observed. To make the nonlinearity more noticeable, an exponential factor defined for two values of a as $(\ln(P_2)- \ln(P_1))/(\ln(a_2)- \ln(a_1))$, where P_i is the scattering signal power, is plotted at the bottom half of figure 9.11. In the case of quadratic dependence corresponding to the linear scattering regime this factor has the value of 2, for the nonlinear regime this value is higher than 2, while in the saturated nonlinear regime the value becomes lower than 2.

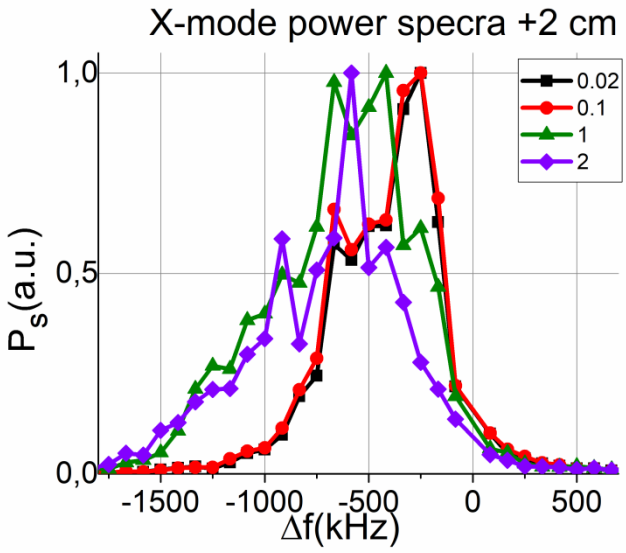

Figure 9.10: DR signal power spectra for X-mode probing at antenna vertical shift +2cm.

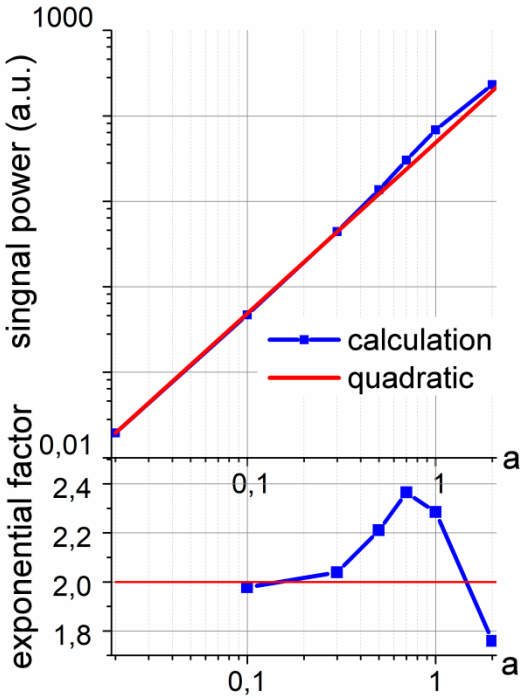

Figure 9.11: DR signal power dependence on the turbulence amplitude and exponential power factor.

Nonlinear scattering, however, does not by itself explain the shift of the scattering spectrum to higher frequencies. The explanation we propose also includes nonlinear dispersion of turbulent fluctuations leading to a lower phase velocity at the higher fluctuation poloidal wavenumbers observed in the GK computations, shown as green solid curve in figure 9.12. That curve on the figure corresponds to the direct computation of the density fluctuations poloidal wavenumber spectrum from ELMFIRE data with consecutive computation of the mean frequency of each wavenumber spectral component. The frequency f_D for all the curves is calculated, same as in section 9.1, as the first moment of the spectrum. For the solid curve it can be seen that for the higher poloidal wavenumber values this mean frequency saturates and stop increasing. This behavior is consistent with the theoretical expectations [13] providing the following dependence of the drift wave phase velocity in the plasma reference system: $v_{ph} = v_{dr}(1 + k_\perp^2 \rho_s^2)^{-1}$. The earlier onset of such saturation, in comparison with what other curves (corresponding to synthetic signals) display, is explained by the fact that due to the turbulence amplitude getting smaller at higher q the numerical noise plays a bigger role and adds a systematic error shifting the value of mean frequency closer to zero. Additionally, DR signal is a result of a convolution between antenna pattern and turbulence spectrum, which means that it corresponds to lower turbulence wavenumbers [78].

It should also be mentioned, that, strictly speaking, the points on the figure 9.12 correspond to different radial positions of the turning point, which depend on the probing poloidal wavenumber. However, in the previous work on the topic [45] with the means of ray-tracing and the weighting function, the difference in radial position was shown to be up to 0.3 cm which is less than the weighting function localization and should not impact results significantly.

In the nonlinear regime characterized by multiple scattering, the backscattering signal is provided in part by fluctuations possessing a factor of 2 smaller poloidal wavenumbers than those satisfying the Bragg condition. Therefore, for the nonlinear turbulence dispersion law shown in figure 9.12 the multiple scattering of the lower-k fluctuations will result in a larger frequency shift than a single scattering induced by the fluctuation possessing a high poloidal wavenumber and satisfying the Bragg condition.

To confirm this idea, we considered the average DR signal spectrum frequency shift corresponding to the different antenna positions and consequently, different poloidal wavenumbers of the probing wave. If the proposed explanation is correct, in the linear regime we would see a saturation of the Doppler frequency shift with growing q due to the turbulence dispersion law. However, in the nonlinear regime of scattering we would obtain the dependence much closer to a linear one. This indeed turned out to be the case and the corresponding plot is shown in the figure 9.12, where the average frequency shift of scattered signal dependence is plotted along with the dispersion calculated directly from the turbulence. The quantities are plotted against the double poloidal wavenumber of the probing X-mode in the turning point (corresponding to poloidal wavenumber of the turbulence) as well as against the antenna vertical shift y.

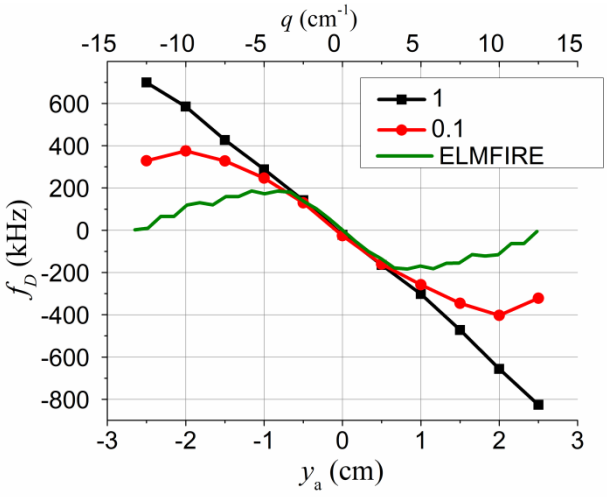

Figure 9.12: Average frequency shift of scattering signal for X-mode against the double probing poloidal wavenumber on top and the vertical position of antenna y. Lines with markers correspond to synthetic DR signal for different amplitudes of the turbulence. Solid line – the turbulence dispersion provided directly by ELMFIRE plotted against the turbulence poloidal wavenumber.

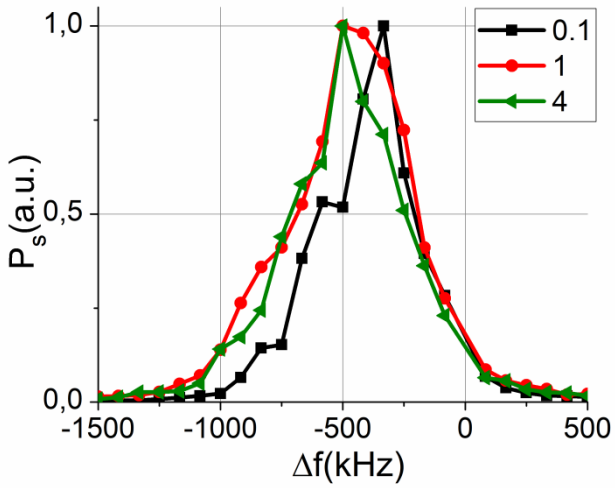

Figure 9.13: Power spectra probing at antenna vertical shift +2cm. Different lines correspond to different amplitudes of the turbulence.

Next, we return to the modelling of DR signals utilizing the turbulence computed for the experimental profile of electron temperature. This case is characterized by a slower decay of the poloidal wavenumber spectrum of the turbulence, which in turn means that nonlinear regime of scattering will now dominate the signal at higher turbulence amplitudes, as predicted by the analytical theory in chapter 8. The spectra, obtained in this case for different turbulence levels and presented on figure 9.13, exhibit a substantially smaller frequency shift, while the DR signal power dependence on the turbulence level transits straight into the nonlinear saturation from the

linear regime as it is seen in figure 9.14, which is a possibility predicted by the analytical theory in the chapter 8 for the case when turbulence spectrum is not steep enough.

The reason, why the difference of spectra in this case is milder, is probably the larger value of the linear Bragg backscattering signal, which dominates over the nonlinear one. Also, during the transition from a single to multiple scattering, the frequency shift does not change significantly (as seen in figure 9.15), likely due to the turbulence dispersion law saturation starting at higher q-values due to a smaller electron temperature. Unfortunately, these values lie in the range where direct computation from ELMFIRE is impossible due to the strong numerical noise, as mentioned previously.

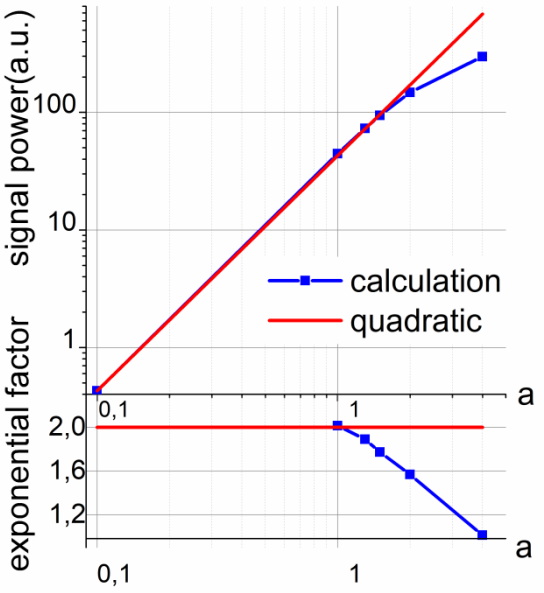

Figure 9.14: DR signal power dependence on the turbulence amplitude and exponential power factor.

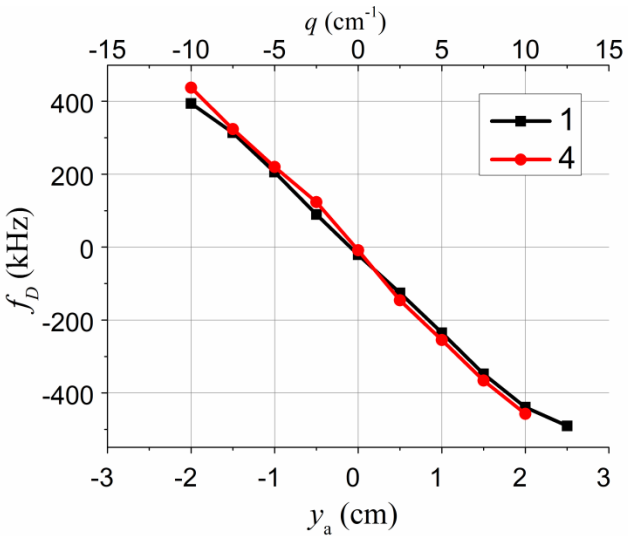

Figure 9.15: Average frequency shift of scattered signal for X-mode. Different lines correspond to different amplitudes of the turbulence.

Overall, it seems that the main effect that the nonlinear regime has on the DR frequency spectrum is “linearization” of the Doppler frequency shift dependency on the poloidal wavenumber of the probing wave. It is caused by the multiple scattering off the longer-scale turbulence dominating DR signal. The backscattering spectrum frequency shift in this regime is determined by the long-scale turbulence dispersion law, as displayed at figure 9.12 and figure 9.15. This in turn means that the saturation of a linear dependence of the frequency shift could be considered as an indicator of the diagnostic operating in linear regime.

The effect of nonlinear scattering on the DR turbulence poloidal wavenumber spectrum measurements and on RCDR is well described in [61], and was reproduced in the simulations [63]. In the case of DR signal power dependence on the antenna vertical shift y, which in the linear scattering regime is related to the turbulence poloidal wavenumber spectrum, the nonlinear effects lead to broadening of the dependence due to the nonlinear saturation of the spectral components corresponding to lower q as it is shown on figure 9.16. In case of the RCDR CCF, analytical theory predicts that in linear regime the correlation decay is slow due to the nonlocal small-angle scattering [22] while in the nonlinear regime, CCF does not directly correspond to the turbulence spatial correlation [19][20] and was shown to be as steep or steeper than the

turbulence correlation function [57]. The same effect was observed in this work and is presented on the figure 9.17. Both figures are plotted for the case of the experimental temperature values.

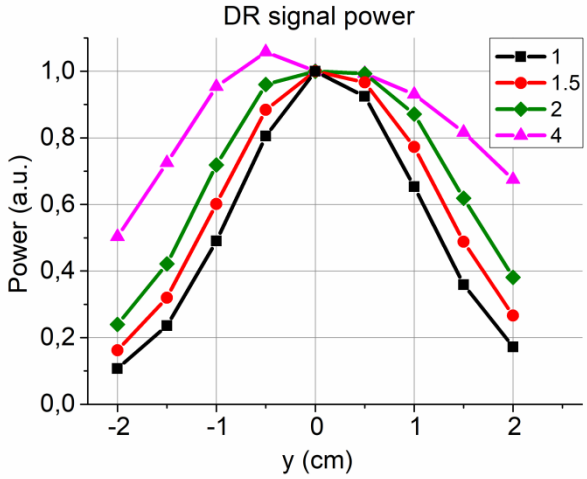

Figure 9.16: DR power dependence on antenna vertical shift. Different lines correspond to different amplitudes of the turbulence.

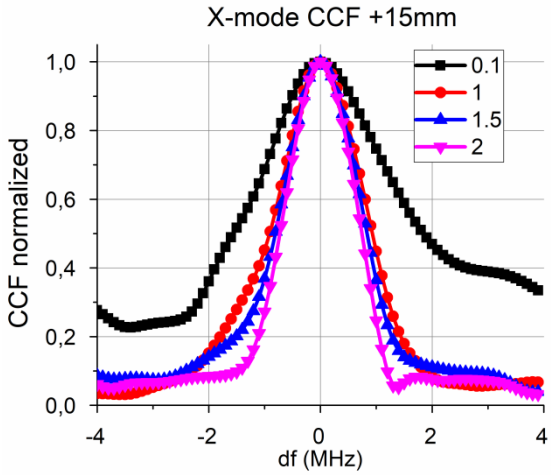

Figure 9.17: Normalized RCDR CCFs. Different lines correspond to different amplitudes of the turbulence.

Both of the nonlinear effects observed are in agreement with the previous results and complicate the interpretation of experimental data. Moreover, obtained results indicate that RCDR diagnostic transitions into the nonlinear regime at lower amplitudes of the turbulence compared to DR for the FT-2 experiments. Overall, is seems that to produce the correct interpretation of experimental data, numerical modelling is necessary.

9.4. O-mode synthetic diagnostic

In the case of O-mode, some full-wave computations were performed, but not the extensive amount that was carried out for X-mode. While experiments were performed for a number of different antennae, as indicated by figure 5.1, only two positions of the antennae were considered. The main position that was studied was the vertical interferometer antenna probing the plasma from above and shifted horizontally by 4.6 cm towards the HFS. In combination with Shafranov shift, it provided a 5cm shift from the discharge center.

The benchmarking of the synthetic RCDR CCF with experimental measurements provided a good agreement, while the DR frequency spectrum showed a strong difference. Respective quantities are shown at figures 9.18 and 9.19. It should be noted however, that the DR spectrum and CCF available were measured in the case with a different magnetic field (2.1 T instead of 1.7 T), which might be part of the reason for the inconsistency between the modelling results and measurements. Another reason might be the fact that in the full-wave modelling the probing a receiving antenna was assumed to have a Gaussian pattern, which is not true for the interferometer antennae used in O-mode experiments. To achieve the full understanding, however, further study of this regime is necessary.

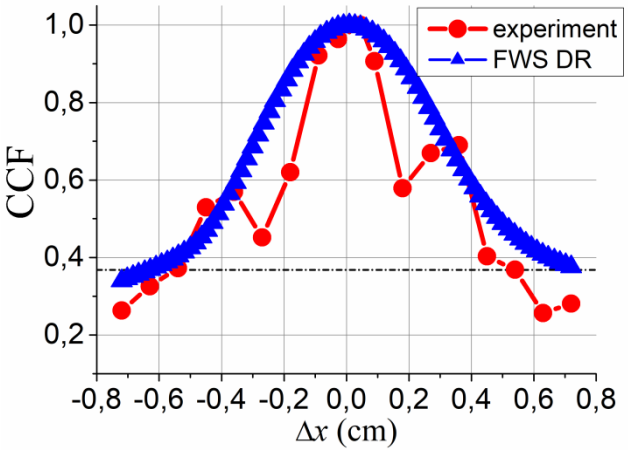

Figure 9.18: RCDR CCF determined experimentally and calculated with a synthetic diagnostic for -2.3 cm antenna.

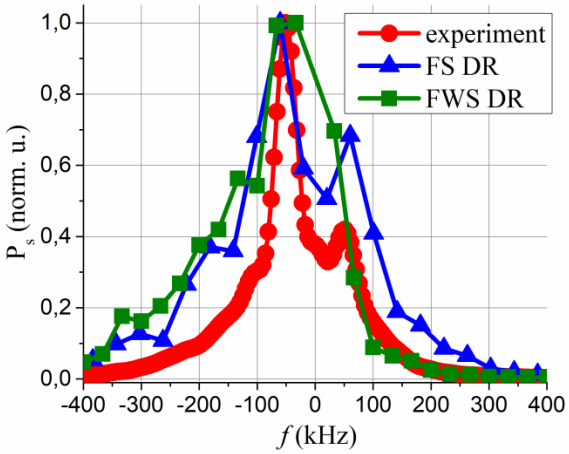

Figure 9.19: DR frequency spectrum determined experimentally and calculated with synthetic diagnostics.

As for nonlinear effects, figure 9.20 illustrates the nonlinear narrowing of the RCDR CCF with the turbulence amplitude growth [63], suggesting that the transition from the linear to the nonlinear regime is happening only for the strongly amplified turbulence. This in turn means that for the original ELMFIRE data the RCDR operates in linear regime. This conclusion is further confirmed by the scattering signal power dependence on the turbulence amplitude shown in the figure 9.21.

As for the DR frequency spectrum, in the case of O-mode, it still demonstrates the aforementioned shift to the higher frequencies in the nonlinear regime, but not a significant one, as can be seen at figure 9.22. This is appropriate for “experimental” ELMFIRE case, where the turbulence dispersion is closer to linear law.

Nonlinear effects for O-mode start to play a role at much higher amplitudes compared to X-mode.

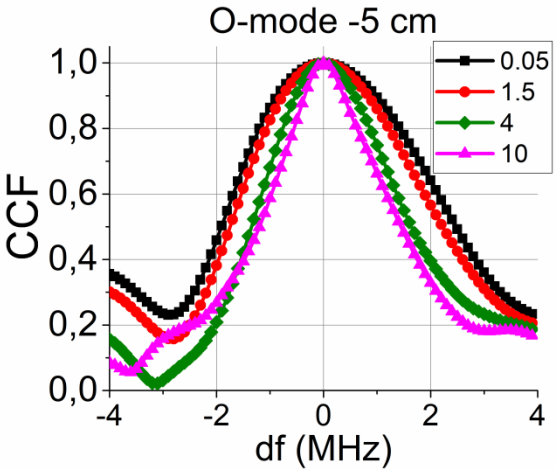

Figure 9.20: CCF for -5 cm antenna shift. Different lines correspond to different amplitudes of the turbulence.

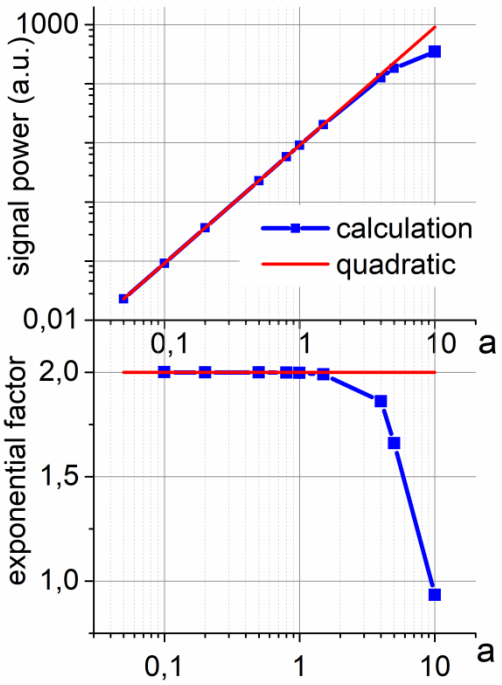

Figure 9.21: DR signal power dependence on the turbulence amplitude.

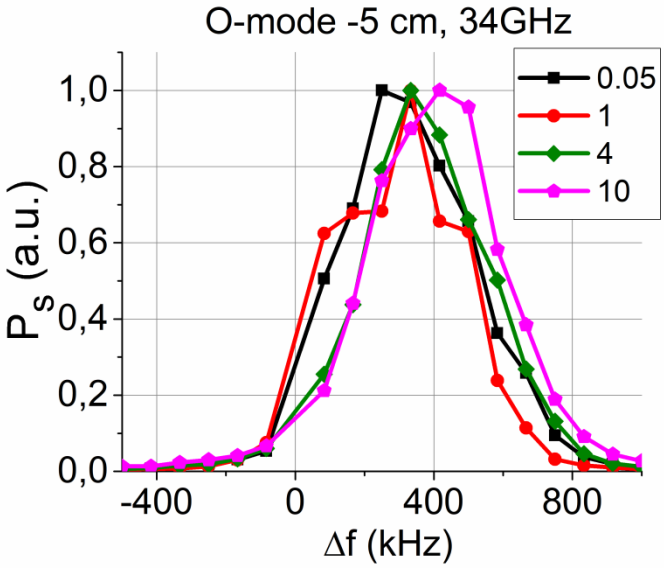

Figure 9.22: DR signal power spectra for probing at 34 GHz and different amplitudes of the turbulence.

Overall, it seems that in the case of O-mode, for the experimental situation, both DR and RCDR operate within the linear regime, which makes the linear numerical modelling relevant and means that O-mode measurements are more suitable for a direct interpretation.

9.5. Discussion

In the performed simulations, DR diagnostic was shown to operate in the linear regime for both O-mode and X-mode probing, with the parameters of synthetic signal generally in agreement with experimental measurements, with the exceptions being the O-mode frequency spectrum and the X-mode poloidal wavenumber spectrum. To explain the discrepancy between synthetic and experimental frequency spectra in case of O-mode, further studies are required, while in the case of X-mode the likely explanation is the insufficiently fine ELMFIRE grid. The synthetic RCDR diagnostic also showed good agreement with experiment, demonstrating that it is operating in linear regime for O-mode and in nonlinear one for X-mode.

Nonlinear effects, such as the narrowing of the RCDR CCF and the flattening of DR poloidal wavenumber measurements were observed. A novel nonlinear effect of “linearization” connected to the interplay of multiple scattering and drift-wave dispersion law was discovered for the DR frequency spectra. It was also shown that X-mode gets affected by nonlinear effects at lower amplitudes of the turbulence compared to O-mode, while RCDR is more affected than DR.

While the simulations for both modes were performed separately, they correspond to the same input plasma parameters and it seems worthwhile to compare the results obtained with both diagnostics. The X-mode probing corresponds to sector 4 on the figure 5.1, while O-mode corresponds to sector 3. Direct calculation of the CCF from ELMFIRE data yields radial correlation length of around 0.2-0.3 cm for both of these regions. The X-mode measurements and the model give the value of radial correlation length of around 0.4 cm (as shown at figure 9.7), while O-mode (figure 9.18) produces the value > 0.5 cm. While not too drastic, this

difference is in agreement with our interpretation of the diagnostics' regime being nonlenar and linear for X-mode and O-mode respectively.

Finally, while the results obtained have demonstrated a qualitative agreement with the analytical predictions, the subject of the future work would be to perform quantitative analysis on the nonlinear scattering regime offset. Analytical criteria provided by chapter 8 and [19][20] would need to be adapted for the situation of FT-2 experiments, possibly including modifications due to the cylindrical geometry effects and compared against the modelling results, as well as other nonlinearity interpretations, such as those presented in [45] and [46].

10. Conclusions

The understanding of turbulent processes governing tokamak plasma is of one the major tasks of the Magnetic Confinement Fusion research. As such the techniques that provide information about the characteristics of the plasma turbulence are of a great importance to the fusion research, since detailed experimental studies are necessary to validate the results of theoretical analysis and numerical modelling. The DR and RCDR techniques are commonly used for this task; however, there are still a lot of open questions about the correct way to interpret experimental measurements provided by them.

Within this thesis, the DR and RCDR techniques were studied both analytically and numerically to broaden the current knowledge of them and to help with the interpretation of experimental data. The goal of the study was to both obtain some general conclusions, and to interpret the specific FT-2 tokamak experiment.

Analytical study covered a number of issues regarding the Doppler reflectometry measurements: First of all, a novel technique for estimating the tilt angle of the turbulent structures was analyzed. Within the linear approximation and slab geometry, solving the Helmholtz equation an expression for the RCDR CCF was obtained and the technique was shown to indeed provide information on the turbulence tilt angle, but with a number of limitations, including the one imposed by poorly-localized small-angle scattering. This limitation, while expected, was not previously analytically described and is a principally new result of this thesis. Another principal conclusion was the fact that tilt angle measurement depended on cut-off separation rather than on turning point separation, as it was suggested before. Aside from that, an alternative technique was suggested to obtain the same results with RCDR. Analytical results were also confirmed with numerical modelling, for which a numerical implementation of Born approximation was developed.

To expand beyond the limitation of the slab geometry model, geometrical effects were studied and analytical expressions demonstrating the difference between slab and cylindrical geometry were obtained. The main and probably the most important difference discovered is the fact that when plasma curvature is strong the decay of the CCF is no longer defined by the cut-off separation of the probing beams, but by a more complicated expression. Results of this analysis were applied to the FT-2 experiment to conclude that in this case the effect of plasma curvature contributes was not principal in that case.

Finally, to better understand the limitations of the linear model, as well as the mechanism behind the onset of nonlinearity, an analysis of the Helmholtz equation with perturbation theory was performed. This analysis provided results describing the onset of the nonlinear regime. While such onset was already described, it was done within a physical optics model. The rigorous analysis has revealed a number of new results, such as alternative turbulence amplitude threshold values for different parameter ranges. These results were then validated with full-wave modelling and were shown to provide significant difference with the previously available formula for relevant plasma parameters found in tokamaks.

On the numerical side of research, to interpret experimental measurements at the FT-2 tokamak, a synthetic DR and RCDR diagnostics were developed. To do that, the results of GK modelling with ELMFIRE code were used as an input data of the full-wave IPF-FD3D code. As a result, synthetic DR and RCDR signals were obtained and benchmarked against experimental

measurements. A reasonable agreement was obtained validating both ELMFIRE modelling and the interpretation of experimental results. In addition, extensive computations were performed to artificially scan the turbulence amplitude to determine the nonlinearity degree of experiment and the way nonlinear effects impact the measurements. An effect of “linearization” of the DR frequency shift depending on the wavenumber of the probing wave was discovered. Also, an earlier onset of nonlinearity was demonstrated for RCDR compared to DR and for X-mode polarization compared to O-mode one.

Overall, within this thesis a number of new results were obtained that can be applied to RCDR experiments on any device. The results of the thesis furthered the understanding on the RCDR and DR diagnostics and the approaches used have shown their effectiveness for the experimental data analysis.

11. Outlook

There are a number of directions in which the work performed in this thesis could be further expanded. From the analytical standpoint, the nonlinearity threshold analysis could be further expanded to encompass also the RCDR diagnostic. The results of such analysis would be interesting in connection with the fact that nonlinearity onset was shown to happen earlier for RCDR than for DR. Similarly, while the results were obtained for the tilt angle measurement technique, it could be worthwhile to study the possibility of the CCF reconstruction in this case in the same way, it is performed for correlation length measurements. Finally, a more detailed application of analytical results of chapter 8 to experimental data would be an interesting topic of further research.

From numerical modelling point of view, the linear model developed within the thesis could be applied to the alternative tilt-angle measurement technique to see which one of these approaches is more feasible. Some efforts were already taken to model the reconstruction procedure for this case and finalizing them could in principle increase applicability of the studied technique. Next, it would be interesting to numerically validate the curvature effects described analytically in chapter 6. Moreover, as mentioned previously, both chapter 7 and chapter 8 could benefit from additional modelling to study the effects of non-Gaussian turbulence spectrum.

Chapter 8 would also benefit from additional numerical and possibly analytical study to address the observed discrepancies between analytical and modelling results. Further confirmation of the proposed explanation could be done the possibility of eliminating those discrepancies could be explored.

In regards to synthetic diagnostic, additional study could be performed to explore if non-Gaussian beam in experiment is the reason for O-mode frequency spectrum inconsistency. A bit more challenging but an interesting task could be inclusion of the metallic wall enabling the multiple passes of the probing beam through plasma in the computation. This multiple pass effect could be responsible for the broadening of the measured poloidal spectrum in X-mode (by causing equatorial probing case to go into nonlinear regime faster) in experiment and accounting for it could resolve the final discrepancy between modelling and experimental results.

Finally, further benchmarking of ELMFIRE turbulence modelling against FT-2 experimental measurements is possible, as the measurements of the enhanced microwave UHR scattering diagnostics are available. In a similar design, synthetic diagnostics can be developed, although the numerical computations in the presence of a UHR could be challenging.

Acknowledgements

As I am starting to write this final chapter of my thesis, I am still undecided on whether I should use the formal style or be a little more personal. For that reason I'd like to do both.

This thesis, which is a culmination of four-year-long efforts, would not be possible without the assistance of a great number of people as well as cooperation of multiple institutions. I would like to first of all thank Ioffe Institute, University of Lorraine and Intsitut Jean Lamour for giving me the opportunity to participate in a joint Ph.D. program. On that note, I would like to thank French Embassy in Moscow for awarding me with Vernadsky scholarship which was the main source of funding behind my project. In particular, I would like to thank Anna Pankova, who guided me through the numerous unexpected complications of being the recipient of the government scholarship. In a similar vein, I would like to thank the Russian Foundation for Basic Research for selecting me for the grant 18-33-0003, which allowed to both significantly advance my project and to present my results at international conferences.

As far as people go, I would like to start by thanking professors Evgeniy Gusakov and Stephane Heuraux whose supervision gave me the much needed guidance to finish this thesis as I am endlessly grateful to them for making this thesis possible. Prof. Gusakov, who has been my mentor since the start of my scientific career, was an invaluable source of theoretical knowledge and his constant interest my project and readiness to spend time answering multitudes of my questions (or, sometimes, answering the same question multiple times) were the source of endless motivation for me. Professor Heuraux, who had the patience to explain to me during hours of discussions all the intricacies of numerical modelling as well as the intricacies of living in France (both of which were an uncharted territory for me) had made this joint Ph.D. enjoyable instead of jarring.

I would also like to thank FT-2 experimental team, in particular Alexey Altukhov and Alexey Gurchenko for providing me with experimental data and guiding me in its interpretation. This project would not be possible without Carsten Lechte graciously providing his code for me to use and Georgiy Zadvistky teaching me how to, for which I am grateful. I'd also like to thank Michail Irzak, whose advice was the main inspiration behind approach to the creation of the synthetic diagnostic and my colleagues from Aalto University for providing me with ELMFIRE data. Finally, I'd like to thank Alexey Popov for always being there for me to address any questions about both physics and institutional regulations. He, along with Natalia Teplova, made our lab room the most welcoming place.

Moving on to the more informal part, I am grateful to my friends from Saint-Petersburg and, in particular, Lisa, who gave me the much needed initial push four years ago to pursue this project and Alex, who was my lifeline to Russia and had saved me multiple times when problems arose. I would also like to thank the people I met during this journey: Mark, Fabian, Erik, Amitoj, Marie, Elias, Alessandro and Remco. Spending time in the International Tea Party was best part of my day during the hardest times.

Last, but definitely not least, I am endlessly grateful to the people who were always there for – my family and my girlfriend Lucy, who at times believed in me and my career choice more than I did.

Bibliography

[1] "BP Statistical Review of World Energy", Review paper, 68th edition, BP Statistical Review of World Energy, London, England, 2019 https://www.bp.com/content/dam/bp/business-sites/en/global/corporate/pdfs/energy-economics/statistical-review/bp-stats-review-2019-full-report.pdf

[2] M. Kikuchi, K. Lackner and M. Q. Tran, "Fusion Physics", International Atomic Energy Agency, 2012

[3] J. Wesson, D. J. Campbell, "Tokamaks, 3rd edition", Clarendon Press, Oxford, England, 2004

[4] E. Gerstner, "Nuclear energy: The hybrid returns", *Nature*. **460**, 25–28, 2009

[5] J. D. Lawson, "Some Criteria for a Power Producing Thermonuclear Reactor", *Proceedings of the Physical Society. Section B*, **70**, 1, 1957.

[6] L. Spitzer, Jr., "A Proposed Stellarator", PM-S-l, internal report or Int Conf USAEC NYO- 993, 1951

[7] I. E. Tamm, "Theory of the magnetic thermonuclear reactor, part 1", *Plasma Physics and the Problem of Controlled Thermonuclear Reactions* (transl.), Pergamon, New York, 1959

[8] Eurofusion website, https://www.euro-fusion.org/news/detail/detail/News/tokamak-principle/

[9] A. J. Wootton, B. A. Carreras, H. Matsumoto et al., "Fluctuations and anomalous transport in tokamaks", *Physics of Fluids B: Plasma Physics*, **2**, 2879, 1990.

[10] B. B. Kadomtsev. "Plasma turbulence", Academic Press, London, New-York, 1965.

[11] W. Horton, "Turbulent transport in magnetized plasmas", World Scientific Publishing Company, 2012

[12] P.H. Diamond et al., "Zonal flows in plasma—a review", *Plasma Phys. Control. Fusion* **47**, R35, 2005.

[13] W. Horton, "Drift waves and transport", *Rev. Mod. Phys.* **71,** 735, 1999

[14] N. Bretz, "Diagnostic instrumentation for microturbulence in tokamaks", *Rev. Sci. Instrum.* **68,** 2927, 1997

[15] G. D. Conway, "Turbulence measurements in fusion plasmas", *Plasma Phys. Control. Fusion* **50,** 124026, 2008

[16] G.D. Conway, B. Scott, J. Schirmer et al., "Direct measurement of zonal flows and geodesicacoustic mode oscillations in ASDEX Upgradeusing Doppler reflectometry", *Plasma Phys. Control. Fusion* **47,** 1165, 2005

[17] P. Hennequin, R. Sabot, C. Honore et al., "Scaling laws of density fluctuations at high-k on Tore Supra", *Plasma Phys.Control. Fusion* **46** B121, 2004.

[18] J. Schirmer et al., "Radial correlation length measurements on ASDEX Upgrade using correlation Doppler reflectometry", *Plasma Phys. Control. Fusion* **49,** 1019, 2007

[19] E. Z. Gusakov, A. Yu. Popov, "Non-linear theory of fluctuation reflectometry", *Plasma Phys. Control. Fusion*, **44,** 2327, 2002

[20] E. Z. Gusakov, A. Yu. Popov, "Two-dimensional non-linear theory of radial correlation reflectometry", *Plasma Phys. Control. Fusion*, **46** 1393, 2004

[21] E. Z. Gusakov, A. Yu. Popov, "Theory of radial correlation Doppler reflectometry", *38th EPS Conference on Plasma Physics* P4.056, 2011

[22] E. Z. Gusakov, M. A. Irzak and A. Yu. Popov, "Radial correlation reflectometry at oblique probing wave incidence (linear scattering theory predictions)", *Plasma Phys. Control. Fusion*, **56,** 025009, 2014

[23] FT-2 tokamak experiment website, http://www.ioffe.ru/HTPPL/ft-2.html

[24] T. P. Kiviniemi et al., "Full f gyrokinetic simulation of FT-2 tokamak plasma", *Plasma Phys. Control. Fusion* **48,** A327, 2006

[25] C. Lechte et al., "X mode Doppler reflectometry k-spectral measurements in ASDEX Upgrade: experiments and simulations", *Plasma Phys. Control. Fusion* **59,** 075006, 2017

[26] A. N. Kolmogorov, "The local structure of turbulence in incompressible viscous fluid for very large Reynolds numbers", *Proceedings of the Royal Society of London A*, **434**, 1890, 1991

[27] R. H. Kraichnan, "Inertial Ranges in Two-Dimensional Turbulence", *The Physics of Fluids*, **10**, 1417, 1967

[28] Website of the University of Stuttgard, https://www.igvp.uni-stuttgart.de/en/research/plasma-dynamics-and-diagnostics/projects/cascade/
[29] H. Biglari, P. H. Diamond and P. W. Terry, "Influence of sheared poloidal rotation on edge turbulence", *Physics of Fluids B: Plasma Physics*, **2**, 1, 1990.
[30] T. Happel, T. Gorler, P. Hennequin et al., "Comparison of detailed experimental wavenumber spectra with gyrokinetic simulation aided by two-dimensional fullwave simulations", *Plasma Phys. Control. Fusion*, **59,** 054009, 2017
[31] L. Vermare et al., "Impact of collisionality on fluctuation characteristics of micro-turbulence", *Physics of Plasmas*, **18**, 012306, 2011
[32] B. B. Kadomtsev and O. P. Pogutse, "Plasma instability due to particle trapping in a toroidal geometry", *Soviet Physics JETP*, **24**, 1734, 1967
[33] P. N. Guzdar, L. Chen, W. M. Tang et al., "Ion-temperature-gradient instability in toroidal plasmas", *The Physics of Fluids*, **26**, 673, 1983.
[34] J. F. Drake, P. N. Guzdar and A. B. Hassam, "Streamer Formation in Plasma with a Temperature Gradient", *Phys. Rev. Lett*., **61**, 2205, 1988
[35] N. T. Gladd, D. W. Ross, "Trapped ion instability in plasmas with magnetic shear", *The Physics of fluids* **16**, 1706, 1973
[36] P. Niskala et al., "Gyrokinetic characterization of the isotope effect in turbulent transport at the FT-2 tokamak", *Plasma Phys. Control. Fusion* **59,** 044010, 2017
[37] G. Zadvitskiy, "Experimental and numerical study of turbulence infusion plasmas using reflectometry synthetic diagnostics", Ph.D. thesis, Université de Lorraine; Universität Stuttgart, tel-01868530v2, 2018
[38] E. Mazzucato, "Small-scale density fluctuations in the adiabatic Toroidal Compressor", Phys. Rev. Lett. **36**, 792, 1976
[39] C. M. Surko, R. E. Slusher, "Study of plasma density fluctuations by the correlation of crossed CO2 laser beams", *The Physics of fluids* **23**, 2425, 1980
[40] A.V. Melnikov et al., "Heavy ion beam probing – diagnostics to study potential and turbulence in toroidal plasmas", *Nucl. Fusion* **57,** 072004, 2017
[41] A. J. Creely et al., "Correlation electron cyclotron emission diagnostics and improved calculation of turbulent temperature fluctuation levels on ASDEX Upgrade", *Rev. Sci. Instrum*. **89,** 053503, 2018
[42] G. R. McKee et al., "The beam emission spectroscopy diagnostic on the DIII-D tokamak", *Rev. Sci. Instrum*. **70**, 913, 1999
[43] G. Conway et al., "Plasma rotation profile measurements using Doppler reflectometry", *Plasma Phys. Control. Fusion* **46**, 951, 2004
[44] F. Fernandez-Marina, T. Estrada and E. Blanco, "Turbulence radial correlation length measurements using Doppler reflectometry in TJ-II", *Nucl. Fusion*, **54**, 072001, 2014
[45] A. B. Altukhov et al., "Fast synthetic X-mode Doppler reflectometry diagnostics for the full-f global gyrokinetic modeling of the FT-2 tokamak", *Physics of Plasmas* **25**, 082305, 2018
[46] A. B. Altukhov et al., "Influence of the probing wave phase modulation on the X-mode radial correlation Doppler reflectometry performance in the FT-2 tokamak", *Physics of Plasmas* **25**, 112503, 2018
[47] A. B. Altukhov et al., "Poloidal inhomogeneity of turbulence in the FT-2 tokamak by radial correlation Doppler reflectometry and gyrokinetic modelling", *Plasma Phys. Control. Fusion* **58,** 105004, 2016
[48] D. Prisiazhniuk et al., "Density fluctuation correlation measurements in ASDEX Upgrade using poloidal and radial correlation reflectometry", *Plasma Phys. Control. Fusion* **60,** 075003, 2018
[49] J. R. Pinzón et al., "Experimental investigation of the tilt angle of turbulent structures in the core of fusion plasmas", *Nucl. Fusion*, **59**, 074002, 2019
[50] J. R. Pinzón et al., "Measurement of the tilt angle of turbulent structures in magnetically confined plasmas using Doppler reflectometry", *Plasma Phys. Control. Fusion*, **61,** 105009, 2019
[51] V. L. Ginzburg, "The propagation of electromagnetic waves in plasmas", Oxford, Pergamon, 1964
[52] E. M. Lifshitz, L. P. Pitaevskii, "Course of theoretical physics: physical kinetics", Butterworth-Heinemann, 1981
[53] T. H. Stix, "Waves in Plasmas", American Institute of Physics, 1992
[54] D. G. Swanson, "Plasma Waves, 2nd Edition", Institute of Physics Publishing, London, 2003

[55] A. D. Piliya, A. Yu. Popov, "On application of the reciprocity theorem to calculation of a microwave radiation signal in inhomogeneous hot magnetized plasmas", *Plasma Phys. Control. Fusion* **44**, 467, 2002
[56] E. Z. Gusakov. M. A. Tyntarev, "The two-dimensional theory of reflectometry diagnostics of plasma fluctuations", *Fusion Eng. Des*. **34–35,** 501, 1997
[57] E. Blanco, T. Estrada, "Two-dimensional full-wave simulations of radial correlation Doppler reflectometry in linear and non-linear regimes", *Plasma Phys. Control. Fusion* **55**, 125006, 2013
[58] E. Z. Gusakov, N. V. Kosolapova, "Fluctuation reflectometry theory and the possibility of turbulence wave number spectrum reconstruction using the radial correlation reflectometry data", *Plasma Phys. Control. Fusion* **53,** 045012, 2011
[59] N. V. Kosolapova et al, "Numerical modelling of tokamak plasma micro turbulence wave number spectrum reconstruction using radial correlation reflectometry data", *J. Phys.: Conf. Ser*. **416** 012020, 2013
[60] E. Z. Gusakov, M. A. Irzak, A. Yu. Popov et al., "Reconstruction of turbulence radial wave number spectra based on the multi-frequency microwave Doppler backscattering data", *Physics of Plasmas* **24**, 022119, 2017
[61] E. Z. Gusakov, A. V. Surkov and A. Yu. Popov, "Multiple scattering effect in Doppler reflectometry", *Plasma Phys. Control. Fusion* **47,** 959, 2005
[62] S. Heuraux et al., "Reflectometry simulation as a tool to explore new schemes of characterizing the fusion plasma turbulence", *J. Phys.: Conf. Ser*. **416,** 012019, 2013
[63] E. Blanco, T. Estrada., "Study of Doppler reflectometry capability to determine the perpendicular velocity and the k-spectrum of the density fluctuations using a 2D full-wave code", *Plasma Phys. Control. Fusion* **50**, 095011, 2008
[64] J. R. Pinzon et al., "Enhanced Doppler reflectometry power response: physical optics and 2D full wave modelling", *Plasma Phys. Control. Fusion* **59,** 035005, 2017
[65] G. D. Conway., "Scattering of reflectometer signals from rippled surfaces", Rev. Sci. Instrum. **64**, 2782, 1993
[66] A. Hasegawa., "Plasma Instabilities and Nonlinear Effects", Springer-Verlag Berlin, Heidelberg, 1975
[67] F. Da Silva, M. C. Pinto, B. Despres, S. Heuraux, "Stable coupling of the Yee scheme with a linear current model", *Journal of Computational Physics* **295**, 24-45, 2015
[68] A. Taflove, S. C. Hagness, "Computational Electrodynamics: The Finite-Difference Time-Domain Method, Third Edition", Artech House, USA, 2005
[69] G. V. Pereverzev, P. N. Yushmanov, "ASTRA Automated System for Transport Analysis in a Tokamak", IPP Report 5/98, Max-Planck-Institut fur Plasmaphysik, Garching, 2002
[70] V. Rozhansky et al., "New B2SOLPS5.2 transport code for H-mode regimes in tokamaks", *Nucl. Fusion* **49** 025007, 2009
[71] F. Merz., "Gyrokinetic Simulation of Multimode Plasma Turbulence", Ph.D thesis, Universität Münster, 2009 (http://genecode.org/PAPERS_1/merz.pdf)
[72] S. Leerink et al., "Multiscale Investigations of Drift-Wave Turbulence and Plasma Flows: Measurements and Total-Distribution-Function Gyrokinetic Simulations", *Phys. Rev. Lett.*, **109** 165001, 2012
[73] E. Z. Gusakov, A. V. Surkov, "Spatial and wavenumber resolution of Doppler reflectometry", *Plasma Phys. Control. Fusion* **46,** 1143, 2004
[74] M. V. Fedoryuk., "Saddle point method", Moscow, 1977 (In Russian)
[75] J. Murray., "Asymptotic Analysis", Springer Verlag, New York, 1984
[76] E. Z. Gusakov, B. O. Yakovlev, "Two-dimensional linear theory of radial correlation reflectometry diagnostics" *Plasma Phys. Control. Fusion*, **44,** 2525, 2002
[77] P. Beckmann, A. Spizzichina, "The Scattering of Electromagnetic Waves from Rough Surfaces", Oxford Pergamon, 1963
[78] G. D. Conway et al., "Recent progress in modelling the resolution and localization of Doppler reflectometry measurements", *14th International Reflectometry Workshop for Fusion Plasma Diagnostics* (*IRW14*) O.213, 2019

Appendix 1. General formula for RCDR CCF with turbulence tilt

If the formula (7.10) was to be considered for arbitrary relation between $l_{\min}$, $l_{\max}$ and ρ, one could still obtain the expression for t_{max} by finding real part of the exponent argument. The key point is to keep in mind imaginary parts of both ρ^* and $\tilde{l}_{cx}$.

To make the formulae more comprehensive we will introduce a number of new designations and rewrite parts of expression (7.10) using them:

$$A_1 = \left|\rho^{*2}\right| = \left(\rho^2 + \frac{{l_{\min}}^2 \sin^2\gamma}{4} + \frac{{l_{\max}}^2 \cos^2\gamma}{4}\right)^2 + \left(\frac{\Delta xc \cos 2\vartheta}{4\omega\cos\vartheta}\right)^2;$$

$$R_1 = \mathrm{Re}\left(\frac{\rho^2}{\rho^{*2}}\right) = \frac{\rho^2 + \frac{{l_{\min}}^2 \sin^2\gamma}{4} + \frac{{l_{\max}}^2 \cos^2\gamma}{4}}{A_1}\rho^2; I_1 = \mathrm{Im}\left(\frac{\rho^2}{\rho^{*2}}\right) = \frac{\left(\frac{\Delta xc\cos 2\vartheta}{2\omega\cos\vartheta}\right)}{A_1}\rho^2;$$

$$A_2 = \left|\tilde{l}_{cx}{}^2\right| = \left({l_{cx}}^2 + \frac{\left(l_{\max}^2 - l_{\min}^2\right)^2 \sin^2 2\gamma}{2\rho^2}R_1\right)^2 + \left(\frac{\left(l_{\max}^2 - l_{\min}^2\right)^2 \sin^2 2\gamma}{2\rho^2}I_1\right)^2;$$

$$R_2 = \mathrm{Re}\left(\frac{{l_{cx}}^2}{\tilde{l}_{cx}{}^2}\right) = \frac{{l_{cx}}^2 + \frac{\left(l_{\max}^2 - l_{\min}^2\right)^2 \sin^2 2\gamma}{2\rho^2}R_1}{A_2}{l_{cx}}^2; I_2 = \mathrm{Im}\left(\frac{{l_{cx}}^2}{\tilde{l}_{cx}{}^2}\right) = \frac{-\frac{\left(l_{\max}^2 - l_{\min}^2\right)^2 \sin^2 2\gamma}{2\rho^2}I_1}{A_2}{l_{cx}}^2;$$

$$\upsilon_{pol}\tilde{t} = \upsilon_{pol}t - 2\Delta x\frac{\sin^3\vartheta}{\cos\vartheta}; \Lambda = \left(l_{\max}^2 - l_{\min}^2\right)\sin 2\gamma/4; \qquad \text{(A1.1)}$$

$$\mathrm{Re}\left(\frac{1}{2\rho^{*2}}\left[-\left(2+\frac{\Delta\omega}{\omega}\right)K\rho^2 + i\upsilon_{pol}t - 2i\Delta x\frac{\sin^3\vartheta}{\cos\vartheta}\right]^2\right) = -\left(\upsilon_{pol}\tilde{t}\right)^2\frac{R_1}{2\rho^2} + 2K\upsilon_{pol}\tilde{t}I_1 + Const(t);$$

$$\mathrm{Re}\left(\frac{\left[i\Delta x + \left(i\upsilon_{pol}\tilde{t} - \left(2+\frac{\Delta\omega}{\omega}\right)K\rho^2\right)\left(l_{\max}^2 - l_{\min}^2\right)\sin 2\gamma/4\rho^{*2}\right]^2}{\tilde{l}_{cx}{}^2}\right) =$$

$$\left(-\frac{\left(\upsilon_{pol}\tilde{t}\right)^2}{{l_{cx}}^2}\left(\frac{\Lambda}{\rho^2}\right)^2\left(R_1^2 - I_1^2\right) + \frac{\upsilon_{pol}\tilde{t}}{{l_{cx}}^2}\frac{\Lambda^2}{\rho^2}8KR_1I_1 - \frac{2\upsilon_{pol}\tilde{t}}{{l_{cx}}^2}\frac{R_1}{\rho^2}\Lambda\Delta x\right)R_2 +$$

$$\left(-\frac{\left(\upsilon_{pol}\tilde{t}\right)^2}{{l_{cx}}^2}\left(\frac{\Lambda}{\rho^2}\right)^2 2R_1I_1 + \frac{\upsilon_{pol}\tilde{t}}{{l_{cx}}^2}4K\frac{\Lambda^2}{\rho^2}\left(R_1^2 - I_1^2\right) + \frac{2\upsilon_{pol}\tilde{t}}{{l_{cx}}^2}\Delta x\frac{\Lambda}{\rho^2}I_1\right)I_2 + Const(t).$$

And as a result:

$$J(t)^{saddle} \propto \exp\left(-\frac{\left(\upsilon_{pol}\tilde{t}\right)^2}{\rho^2}\left(\frac{R_1}{2}+\frac{\Lambda^2}{\rho^2 l_{cx}{}^2}\left(2R_1I_1I_2+\left(R_1{}^2-I_1^2\right)R_2\right)\right)\right)\times$$

$$\exp\left(2\upsilon_{pol}\tilde{t}\left(KI_1+\frac{2K\Lambda^2}{l_{cx}{}^2\rho^2}\left(\left(R_1{}^2-I_1^2\right)I_2+2R_1I_1R_2\right)+\frac{\Lambda\Delta x}{l_{cx}{}^2\rho^2}\left(R_1R_2-I_1I_2\right)\right)\right);$$

$$\upsilon_{pol}t_{\max}=2\Delta x\frac{\sin^3\vartheta}{\cos\vartheta}-\frac{KI_1\rho^2+\frac{2K\Lambda^2}{l_{cx}{}^2}\left(\left(R_1{}^2-I_1^2\right)I_2+2R_1I_1R_2\right)+\frac{\Lambda\Delta x}{l_{cx}{}^2}\left(R_1R_2-I_1I_2\right)}{\frac{R_1}{2}+\frac{\Lambda^2}{\rho^2 l_{cx}{}^2}\left(2R_1I_1I_2+\left(R_1{}^2-I_1^2\right)R_2\right)}; \qquad \text{(A1.2)}$$

$$\upsilon_{pol}\Delta_t=\sqrt{\frac{2\rho^2}{R_1+\frac{2\Lambda^2}{\rho^2 l_{cx}{}^2}\left(2R_1I_1I_2+\left(R_1{}^2-I_1^2\right)R_2\right)}}.$$

Now, to tie this in with the previous results one can note that in the case of $l_{\min}$, $l_{\max}$, $\Lambda^{0.5}<<\rho$; $\Delta x \sim l_{cx}$ and R_1, $R_2 \sim 1 >> I_1$, I_2 and formula (A1.2) coincides with (7.14). Another result that can be inferred from this formula is that, as expected for turbulence with $\Lambda=0$ it gives $\upsilon_{pol}t_{max}=\Delta x\tan\vartheta$.

Glossary

Character	Description	Units
n	Plasma number density	cm^{-3}
τ_E	Energy confinement time	s
T	Plasma temperature	keV
δn	Plasma electron density fluctuations' amplitude	cm^{-3}
r	Radial coordinate in toroidal/cylindrical geometry system	cm
φ	Poloidal coordinate in toroidal geometry system	rad
z	Torotidal coordinate in cylindrical geometry system	cm
k	Wavenumber in Fourier space	cm^{-1}
κ	Radial wavenumber wavenumber of the turbulence	cm^{-1}
q	Poloidal wavenumber of the turbulence	cm^{-1}
γ	Tilting angle of turbulence structure	rad
ρ_{ci}	Ion Larmor radius	cm
T_i	Plasma ion temperature	eV
m_i	Ion mass	g
e	Elementary charge	statC
$k_\perp$	Turbulence wavevector component perpendicular to magnetic field	cm^{-1}
ρ_{ce}	Electron Larmor radius	cm
$\hat{\varepsilon}$	Plasma dielectric tensor	-
m_e	Electron mass	g
ω_{pe}	Electron plasma frequency	Hz
ω_{ce}	Electron cyclotron frequency	Hz
ω_{pe}	Ion plasma frequency	Hz
ω_{ci}	Ion cyclotron frequency	Hz
ω	Angular frequency of the probing wave	Hz
n_c	O-mode critical density	cm^{-3}
E_z	Toroidal component of electric field	statV/cm
f_D	The first momentum of frequency spectrum	Hz
v_{ph}	Phase velocity of the probing wave	cm/s
v_{pol}	Poloidal rotation velocity of plasma	cm/s
Ω	Turbulence frequency	Hz
f	Central frequency on the probing wave	Hz
L	Cut-off radial position	cm
k_y	Poloidal wavenumber of the wave	cm^{-1}
$L(k_y)$	Turning point radial position	cm
α	Airy scale	cm
P	Probing beam power	erg/s
A_s	Scattered field amplitude	statV/cm
r_a	Tokamak minor radius	cm
ρ	Probing beam radius	cm
ϑ	Probing angle with respect to normal probing	rad
K	Central poloidal wavenumber of the probing wave	cm^{-1}
$\Delta\omega$	Frequency separation of probing waves	Hz
Δx	Cut-off separation of probing waves	cm
l_{cx}	Radial correlation length of the turbulence	cm
t_{max}	Time delay corresponding to maximum correlation of two signals	s
Δy	Poloidal separation of the maximum of correlation	cm
m	Poloidal wavenumber of the probing wave normalized by radius	-
$k_m(r)$	Probing wave radial wavenumber corresponding to specific m	cm^{-1}

Φ	Phase of the probing wave	-
α_c	Cylindrical symmetry analog of Airy scale	cm
l_{min}	Largest spatial scale of the turbulence	cm
l_{max}	Shortest spatial scale of the turbulence	cm
t_c	Turbulence decorrelation time	s
l_{cy}	Poloidal correlation length of the turbulence	cm
a	Turbulence amplitude anhancement factor	-
n_i	Exponential power scaling factor	-
Δf	The second momentum of frequency spectrum	Hz

Abstract

Plasma turbulence is nowadays believed to be responsible for the anomalous transport and consequently the degradation of discharge conditions in magnetic confined fusion devices, such as tokamaks. Since a good energy confinement time is crucial for achieving a positive energy yield, understanding and control of turbulent processes is currently one of the major goals of the Magnetic Confinement Fusion research. To study the plasma turbulence, experimental tools that are able to provide information about its characteristics are necessary. Such tools include microwave diagnostics and, in particular, Doppler reflectometry and radial correlation Doppler reflectometry. While these non-invasive diagnostics benefit from the simplicity of the setup, there are a number of unresolved issues when it comes to the interpretation of the experimental data. Issues such are small-angle scattering and plasma curvature effects limit the range of applicability of the simple interpretation of the measurements, while nonlinear scattering effects make it inapplicable altogether. These problems make it necessary to validate the interpretation of experimental data.

Thus, the primary goal of this thesis was to create a synthetic Doppler reflectometry and radial correlation Doppler reflectometry diagnostic for the interpretation of the FT-2 tokamak experimental results. This goal is achieved by applying full-wave IPF-FD3D code to the results of gyrokinetic plasma modelling with ELMFIRE code to obtain the synthetic signals, which are then benchmarked with experimental measurements. The synthetic diagnostic is also used for a more general study of the possibility of nonlinear effects influencing the experimental measurements. Finally, the secondary goal of this thesis was to perform an analytical research of plasma curvature effects, nonlinear scattering and a novel technique for turbulence structures' characterization. The first principles analytical study was performed by considering the Helmholtz equation and obtaining an analytical expression for the experimental signals. The results for the latter two topics were numerically validated with the partial use of specially developed linear numerical model and the full-wave IPF-FD3D code.

Keywords: simulations, diagnostic, reflectometry

Résumé

La turbulence du plasma est considérée aujourd'hui comme le mécanisme responsable du transport anormal induisant la dégradation du confinement de l'énergie des plasmas de fusion confinés magnétiquement, tels que les tokamaks. Le temps de confinement de l'énergie est un paramètre crucial pour atteindre un rendement énergétique positif. La maîtrise de ce paramètre passe la compréhension et le contrôle de la turbulence du plasma. Ces thèmes de recherche correspondent actuellement aux principaux objectifs de la recherche sur la fusion par confinement magnétique. Pour réaliser l'étude de la turbulence plasma, des outils expérimentaux capables de fournir ses caractéristiques sont nécessaires. Ces outils comprennent les diagnostics par micro-ondes et, en particulier, la réflectométrie Doppler et la réflectométrie de corrélation radiale Doppler. Bien que ces diagnostics non invasifs bénéficient d'une configuration simple, il existe un certain nombre de problèmes non résolus associés à l'interprétation des données expérimentales. Des problèmes tels que la diffusion aux petits angles et les effets de courbure du plasma limitent le champ d'application d'une interprétation simple des mesures. La prise en compte des effets de diffusion non linéaire rende l'interprétation standard inapplicable. Ces problèmes nécessitent de valider l'interprétation des données expérimentales.

Ainsi, l'objectif principal de cette thèse était de créer un diagnostic de réflectométrie Doppler synthétique et de réflectométrie de corrélation radiale Doppler pour l'interprétation des résultats expérimentaux du tokamak FT-2. Cet objectif fut atteint en appliquant le code full-wave IPF-FD3D aux résultats d'une modélisation gyrocinétique du plasma turbulent avec le code ELMFIRE pour obtenir les signaux synthétiques. Ces derniers sont ensuite comparés avec des mesures expérimentales. Le diagnostic synthétique est également utilisé pour une étude plus générale de la contribution des effets non linéaires lors des mesures expérimentales. Un objectif secondaire de cette thèse correspondait à une recherche analytique sur les effets de courbure du plasma et de la diffusion non linéaire puis sur une nouvelle technique pour la caractérisation des structures turbulentes. L'étude analytique basée sur les premiers principes a été réalisée en considérant l'équation de Helmholtz et en obtenant une expression analytique pour les signaux expérimentaux. Les résultats pour ces deux derniers sujets ont été validés numériquement avec l'utilisation partielle d'un modèle numérique linéaire spécialement développé pour ce type d'études et du code IPF-FD3D.

Mots clés: simulation, diagnostique, reflectometrie